

# SYNTHESIS, CHARACTERIZATION AND MACROSCOPIC MANIPULATION OF CARBON NANOTUBES

THÈSE N° 3364 (2005)

PRÉSENTÉE À LA FACULTÉ SCIENCES DE BASE

Institut de physique de la matière complexe

PROGRAMME DOCTORAL EN PHYSIQUE

ÉCOLE POLYTECHNIQUE FÉDÉRALE DE LAUSANNE

POUR L'OBTENTION DU GRADE DE DOCTEUR ÈS SCIENCES

PAR

Csilla MIKÓ

M.Sc. Certified Teacher of Physics, Eötvös Loránd University, Hongrie  
et de nationalité hongroise

acceptée sur proposition du jury:

Prof. L. Forró, directeur de thèse  
Prof. J.-Ph. Ansermet, rapporteur  
Dr K. Hernádi, rapporteur  
Prof. J. Nagy, rapporteur

Lausanne, EPFL  
2005



SYNTHESIS, CHARACTERIZATION AND  
MACROSCOPIC MANIPULATION OF  
CARBON NANOTUBES

LAUSANNE, EPFL

2005



---

## Version abrégée

Ce manuscrit de thèse rapporte la synthèse, la caractérisation et la manipulation de nanotubes de carbone. Deux aspects y sont abordés : (i) la synthèse des nanotubes de carbone par décomposition catalytique d'hydrocarbure, (ii) la fabrication et le renforcement des fibres macroscopiques de nanotubes de carbone.

Dans une première partie, une étude de certains paramètres liés à la croissance des nanotubes a été menée de manière systématique. L'effet de la composition du catalyseur supporté (stœchiométrie de l'alliage métallique, nature du support), l'effet de la température du réacteur et l'effet du temps de séjour du catalyseur dans le réacteur ont été étudiés. Il semble que  $\text{Fe}_2\text{Co}$  présente la meilleure activité catalytique parmi les alliages de composition  $\text{Fe}_{1-\xi}\text{Co}_\xi$ . Un écart par rapport à cette stœchiométrie optimale ( $\text{Fe}/\text{Co}=2$ ) accroît l'empoisonnement du catalyseur. D'autre part,  $\text{CaCO}_3$ , utilisé comme support, semble être une source supplémentaire de carbone. En effet, le  $\text{CO}_2$ , produit lors de la décomposition du support, réagit avec l'acétylène et participe au mécanisme de croissance des nanotubes. Les supports de type carbonates d'alcalino-terreux limitent l'agglomération des particules métalliques, et sont donc une source de réactifs.

Dans la deuxième partie, des fibres ont été fabriquées à partir de nanotubes de carbone afin d'exploiter leurs excellentes propriétés mécaniques à l'échelle macroscopique. Les propriétés électriques ont aussi été mesurées. Les fibres présentent une conductivité par saut, bien qu'elles soient fabriquées à partir de nanotubes métalliques et semi-conducteurs. Les tests mécaniques des fibres non renforcées montrent que les propriétés de nanotubes individuels ne sont pas conservées à l'échelle macroscopique. Ceci peut être expliqué par la faiblesse des interactions de type van der Waals entre les nanotubes. Le renforcement de ces fibres a été réalisé après irradiation par électrons et rayons UV à faible dose. Des liaisons C-C ont été produites entre les nanotubes. Cette réticulation explique l'augmentation du module de cisaillement des fibres et a été confirmée par des mesures électriques. Contrairement à l'exposition aux photons UV, l'irradiation par électrons à dose forte provoque un désordre dans la structure graphitique des nanotubes. Ceci est à l'origine d'une diminution du module de Young. Par conséquent, l'irradiation UV, qui ne provoque pas de redistribution des atomes de carbone, semble plus adaptée au renforcement des fibres de nanotubes.

## Abstract

This thesis describes the synthesis, characterisation and macroscopic manipulation of carbon nanotubes. Two interconnected aspects were investigated: (i) growth of carbon nanotubes by catalytic chemical vapour deposition of acetylene and (ii) assembly and reinforcement of macroscopic carbon nanotube fibres.

The first part describes a systematic study of the growth of carbon nanotubes by chemical vapour deposition. In particular, the effect of the growth parameters, such as catalyst composition, catalyst carrier, temperature, and retention time, on the yield and quality of CNTs was investigated. It was found that  $\text{Fe}_2\text{Co}$  is the most active catalyst in the bimetallic family of  $\text{Fe}_{1-\xi}\text{Co}_\xi$ , whereas deviation from this ideal compound was identified as poisoning the catalytic reaction. Furthermore, the  $\text{CaCO}_3$  support was found to be an additional source of carbon. This chemical reaction was explained by the decomposition of  $\text{CaCO}_3$ , which produces  $\text{CO}_2$  groups that react with acetylene to result in carbon for the growth of CNTs. Hence, it was discovered that carbonate supports are not only acting as an inert support to avoid the coarsening of catalyst particles but as an additional source of reactant during the growth.

In the second part, macroscopic, oriented fibres were assembled from CNTs in order to exploit their excellent mechanical properties. Electrical as well as mechanical properties were measured. Although both semiconducting and metallic CNTs are present in the starting material, electrical measurements on the macroscopic ropes of CNTs revealed a hopping-like conductance of the fibres. Measurements of mechanical properties have pointed out that these fibres lack the strength of an individual nanotube. The main problem is the weak van der Waals interaction between the tubes which lead the tubes to slide easily along their axes. This problem was addressed by irradiation experiments: Pure covalent carbon-carbon bonds were established in CNT fibres by a low dose of electron and ultraviolet irradiation resulting in an enhancement of the shear modulus between the tubes. Moreover, electrical measurements have demonstrated that a low dose of electron irradiation can significantly increase the shear modulus via cross-linking of CNTs in the fibre, but a high electron dose disorders the graphitic structure and results in a loss of the intrinsically high Young's modulus of the individual tubes. In contrast to electrons, the ultraviolet photons do not displace carbon atoms in the nanotube, therefore the reinforcement can be achieved by keeping the graphitic structure of the tubes intact.

## Kivonat

Ez a dolgozat szén nanocsövek növesztésével, karakterizálásával és makroszkópikus manipulálásával foglalkozik. Két egymással összefüggő részre tagolódik: a szén nanocsövek katalitikus növekedésének vizsgálatára valamint a nanocsövek szállá történő összeszerelésére és megerősítésére.

Az első rész a nanocsövek növekedésének szisztematikus vizsgálatát írja le az acetilén katalitikus kémiai gőzfázisú rétegleváltszása (CCVD) során. Részletesen tanulmányoztuk a katalizátor összetételének, a hordozófelület típusának, a nanocsövek növesztési hőmérsékletének és időtartamának hatását a nanocsövek mennyiségére és minőségére. Katalizátorok közül a  $\text{Fe}_{1-\xi}\text{Co}_\xi$  bimetál család tagjait vizsgálva azt tapasztaltuk, hogy a legaktívabb katalizátor a  $\text{Fe}_2\text{Co}$  ötvözet. Eltérések ettől az ideális százalékos összetételtől csökkentették a katalizátor aktivitását. Az alkáli-földfém karbonát hordozófelületek hatásainak vizsgálakor kiderült, hogy az általunk használt  $\text{CaCO}_3$  egy másodlagos szénforrás szerepét is betölti a szokásos katalizátor elválasztó funkciója mellett. A szénproduktív kémiai reakciólánc első lépésében  $\text{CO}_2$  keletkezik a mézskő bomlása révén, majd a  $\text{CO}_2$  acetilénnel történő reakciója során szén keletkezik, melyből a katalizátoron keresztül nanocső szintetizálódik.

A második részben rendezett makroszkópikus szálakat állítottunk elő nanocsövekből. Elektromos vezetőképesség mérések rámutattak arra hogy, míg az egyedi nanocsövek fémesek illetve félvezetőek, addig a belőlük készített makroszkópikus szálaknak a granulált anyagokra jellemző ún. "hopping" jellegű az elektromos vezetőképessége. A mechanikai tulajdonságok vizsgálatai rávilágítottak a szálak alacsony Young-modulusára, holott az egyes nanocsövek rendkívül nagy szilárdságúak. Ennek oka az, hogy egyes csövek között fellépő gyenge van der Waals kölcsönhatás, ami a csövek egymáshoz viszonyított könnyed, hosszirányú elcsúszását lehetővé teszi. E probléma orvoslására elektron és ultraibolya besugárzást használtunk, amelyek erős szén-szén kovalens kötések hoztak létre az egyes csövek között. A besugárzás során végzett elektromos mérések megmutatták, hogy alacsony dózisi elektron besugárzással kereszt-kötések alakulnak ki az egyes csövek között, jelentős mértékben növelve ezáltal a csövek közötti nyíró modulust. A túlzott elektron dózis viszont teljesen rendezetlenné teszi a szálakat: a kezdetben nagy Young modulussal rendelkező nanocsövek elvesztik kedvező rugalmassági tulajdonságaikat, amorf szerkezetűvé válnak. Az elektron besugárzással ellentétben az ultraibolya fotonok nem ütö ki a szén atomokat a helyükről, megmarad tehát a nanocsövek szerkezete, hanem a jelenlevő DMF és a nanocsövek felületén található szabad gyökök közötti kötések összefogják a szálakat.









## Acknowledgements

There are many people to thank for their support and encouragement, without whom this thesis would not have been possible.

Firstly, I thank my thesis advisor, Professor László Forró for directing and supporting this research and for giving me the possibility to work in his research group under excellent working conditions and for opening many other sources of opportunities not just for studying, but cultural ones as well. This thesis is built on his creative ideas and constructive propositions which helped me to find my way.

This thesis was partially funded by the following research projects: European Commission (RTN Program, NANOCOMP network, RTN1-1999-00013) and the Swiss National Science Foundation (grant number 61534) Their financial support is gratefully acknowledged. The Swiss National Center of Competence in Research Nanoscale Science (NCCR Nanoscience) has been a helpful network.

Dr. Richárd Gaál helped me by sharing a part of his great expertise in all subjects related to carbon nanotubes and physical measurement in the laboratory from my arrival. I owe him much for his patience and helpfulness not only in the lab, but also in private.

Many thanks to Dr. Jin Won (Maria) Seo, who was my supporting advisor, for her endless patience and for numerous discussions. In addition, she gave me plenty of useful advice in different areas, such as microscopy and paper writing.

Next to her, Dr. Arnaud Magrez supported me with his advice and with his good sense of humour. He proved to me that chemistry is not cuisine but the inverse. (also many thanks for the help with French!)

I thank Prof. Jean-Philippe Ansermet and Prof. János B. Nagy, together with Dr. Klára Hernádi for accepting to participate on the jury of this thesis.

I would like to thank the present and the former members of the NN group, with whom I have passed many pleasurable moments not only in the institute, but also in the outside world: Ana Akrap, Christel Dieker, Sylvia Jeney, Yanki Keles, Gerit and Andrzej Kulik, Thomas Geiges, Camilo Guzman, Kyumin Lee, Branimir Lukić, Bálint Náfrádi, Balázs Sipos, Bertrand Vileno, Neven Barišić, Slaven Garaj, Titusz Fehér, András Kis, Pierre Marcoux, Polona Umek and Tim Skirrow. Great thanks also to my officemates: Mirko Milas, Raph ael Foschia and Stefan Hengsberger. I am also thankful to Dr. Edina Couteau, who introduced me to the world of chemistry via synthesis and purification of nanotubes in the first months. Many thanks to the members of IPMC for their friendship during the past several years. Thanks also to “Richi”, Maria and “Arno” for critical reading of the manuscript.

I am indebted to Bernard Guisolan and the technicians of the IPMC mechanical

workshop for the machined pieces used in this thesis as well as to Gerald Beney for his technical support around the CCVD furnaces. I also thank Brian Senior, Silviya Gradečak and Guido Milanesi for help and troubleshooting of the electron microscopes and the CIME for access to the electron microscopes.

Many thanks to Monique Bettinger, who helped me a lot as our institute secretary, by her efficiency and smiles.

Finally I would like to thank members of my family and the Mikó family for their support of so many years, especially my husband and my daughter, who were with me for better, for worse and shared all the pleasures and troubles of these years.

# Contents

|          |   |           |
|----------|---|-----------|
| <b>1</b> | <b>Introduction</b>   | <b>1</b>  |
| <b>2</b> | <b>Physical Properties of Carbon Nanotubes</b>                            | <b>5</b>  |
| 2.1      | Allotropes of carbon . . . . .  | 5         |
| 2.2      | Basic structures of nanotubes . . . . .                                   | 7         |
| 2.3      | Electronic properties of CNTs . . . . .                                   | 10        |
| 2.4      | Chemical reactivity of CNTs . . . . .                                     | 11        |
| 2.5      | Mechanical properties . . . . .   | 12        |
| 2.5.1    | Defects and deformations in carbon nanotubes . . . . .                    | 13        |
| 2.5.2    | Potential applications . . . . .  | 17        |
| <b>3</b> | <b>Synthesis of Carbon Nanotubes</b>                                      | <b>19</b> |
| 3.1      | Synthesis methods . . . . .   | 19        |
| 3.1.1    | Arc-discharge . . . . .   | 19        |
| 3.1.2    | Laser ablation . . . . .  | 21        |
| 3.1.3    | Catalytic chemical vapour deposition . . . . .                            | 22        |
| 3.1.4    | Other synthesis methods . . . . .   | 24        |
| 3.2      | Theory of catalytic growth of CNTs . . . . .                              | 25        |
| <b>4</b> | <b>Characterisation Techniques</b>  | <b>29</b> |
| 4.1      | Electron microscopy . . . . .   | 29        |
| 4.1.1    | Scanning electron microscopy . . . . .                                    | 29        |
| 4.1.2    | Transmission electron microscopy . . . . .                                | 32        |
| 4.2      | XRPD . . . . .  | 37        |
| 4.3      | TGA . . . . .   | 37        |
| <b>5</b> | <b>CCVD Growth of Carbon Nanotubes by Using Alkaline Earth Carbonates</b> | <b>39</b> |
| 5.1      | Furnace . . . . .   | 40        |
| 5.1.1    | Fixed-bed furnace . . . . .   | 40        |

|          |  |           |
|----------|--|-----------|
| 5.1.2    | Rotary tube furnace . . . . .  | 40        |
| 5.2      | Catalyst . . . . .   | 41        |
| 5.2.1    | Catalyst preparation . . . . .   | 41        |
| 5.2.2    | Catalyst composition . . . . .   | 42        |
| 5.3      | Catalyst support . . . . .   | 48        |
| 5.4      | Retention time . . . . .   | 52        |
| 5.5      | Mass production . . . . .  | 53        |
| 5.6      | Growth mechanism . . . . .   | 54        |
| 5.7      | Conclusion . . . . .   | 55        |
| <b>6</b> | <b>Assembly, Mechanical Characterisation and Reinforcement of Macroscopic Carbon Nanotube Fibres</b> | <b>57</b> |
| 6.1      | Overview of measurement techniques . . . . .   | 58        |
| 6.1.1    | Mechanical measurements . . . . .  | 58        |
| 6.1.2    | Strength of single carbon nanotubes . . . . .  | 58        |
| 6.1.3    | Electrical resistivity measurements . . . . .  | 62        |
| 6.1.4    | Four-probe resistivity measurements . . . . .  | 63        |
| 6.2      | Assembly of nanotubes to macroscopic fibers . . . . .  | 63        |
| 6.2.1    | Methods of alignment of CNTs . . . . .   | 64        |
| 6.2.2    | Conclusion . . . . .   | 72        |
| 6.3      | Irradiation and reinforcement of ropes of CNTs . . . . .   | 72        |
| 6.3.1    | Irradiation effects on carbon nanostructures . . . . .   | 72        |
| 6.3.2    | Irradiation effects on graphite . . . . .  | 73        |
| 6.3.3    | Irradiation effects on carbon nanotubes . . . . .  | 74        |
| 6.4      | Sample preparation . . . . .   | 78        |
| 6.4.1    | Electrophoresis . . . . .  | 78        |
| 6.4.2    | Extrusion . . . . .  | 80        |
| 6.5      | Experimental results on as-prepared samples . . . . .  | 80        |
| 6.5.1    | Mechanical measurements . . . . .  | 80        |
| 6.5.2    | Four-probe measurements on the ropes of SWNTs . . . . .  | 83        |
| 6.6      | Cross-linking CNT fibres by e-beam: a resistivity study . . . . .                                    | 84        |
| 6.7      | Enhancement of the macroscopic fibre by ultraviolet light . . . . .                                  | 88        |
| 6.7.1    | Interlinking SWNTs by UV light . . . . .   | 88        |
| 6.7.2    | In-situ resistivity measurements on the SWNT fibres . . . . .  | 88        |
| 6.7.3    | Young's modulus measurements . . . . .   | 89        |
| 6.8      | Conclusion . . . . .   | 92        |
| <b>7</b> | <b>General Conclusions</b>   | <b>95</b> |

---

|  |            |
|--|------------|
| <b>A Purification of Nanotubes</b>                                 | <b>97</b>  |
| A.1 Overview of purification methods on CNTs . . . . .             | 97         |
| A.1.1 Chemical purification . . . . .                              | 98         |
| A.1.2 Mechanical purification . . . . .                            | 99         |
| A.1.3 Purification with surfactant by ultrasonication . . . . .    | 101        |
| A.2 Results on the purification of CNTs . . . . .                  | 102        |
| A.2.1 Purification of multiwall nanotubes grown by CCVD . . . . .  | 102        |
| A.2.2 Purification of multiwall nanotubes grown by AD . . . . .    | 104        |
| <b>B Data Acquisition from the HP3562A Digital Signal Analyzer</b> | <b>107</b> |
| B.1 The program in Labview . . . . .                               | 108        |
| <b>Curriculum Vitae</b>  | <b>127</b> |
| <b>Publications</b>  | <b>129</b> |





# List of Figures

|      |   |    |
|------|---|----|
| 2.1  | Allotropes of carbon: Structural model of (a) black carbon soot, (b) transparent diamond, and (c) graphite. (d) shows a fullerene ( $C_{60}$ ) and an end of a carbon nanotube. . . . .   | 6  |
| 2.2  | The first TEM micrograph of branching nanotubes by Endo [16]. . .   | 7  |
| 2.3  | (a) The hexagonal graphene sheet with the base vectors $\vec{a}_1$ and $\vec{a}_2$ , translational vector $\vec{T}$ , chiral vector $\vec{C}_h$ and chiral angle $\vartheta$ . The chiral vector is defined on the honeycomb lattice of carbon atoms by unit vectors and the chiral angle with respect to the zigzag axis. Along the zigzag axis $\vartheta=0^\circ$ . (b) A SWNT is formed when the ends of the chiral vector $\vec{C}_h$ are put together. The circumference of the tube is given by the vector $\vec{C}_h$ . . . . . | 8  |
| 2.4  | Zigzag (a), chiral (b) and armchair (c) nanotubes. . . . .  | 8  |
| 2.5  | The “discovery” of CNTs. Bright field TEM images of multi-walled CNTs from Iijima’s seminar paper [18]. . . . .   | 9  |
| 2.6  | Exotic CNT structures . . . . .   | 10 |
| 2.7  | The chemical reactivity of CNTs is described by the $\pi$ -orbital mismatch. Diagrams of (a) $\pi$ -orbitals of a graphene sheet, (b) pyramidalization angle ( $\theta_P$ ), and (c) the $\pi$ -orbital misalignment angles ( $\phi$ ) along the $C_1 - C_4$ in the (5,5) SWNT and its capping fullerene, $C_{60}$ from reference [47]. . . . .   | 12 |
| 2.8  | TEM micrographs of different MWNT caps the paper of Iijima [62].  | 14 |
| 2.9  | Pentagon and heptagon deformations in the hexagonal lattice indicated by letters P and H [62]. . . . .  | 14 |
| 2.10 | (a) The strain-energy curve for the bending of a (13,0) nanotube switches from harmonic to linear at a buckling point at the buckling angle of approximately $57^\circ$ . The force (broken line) drops and remains almost constant. (b) MD simulation of a buckled nanotube [53]. (c) TEM micrograph of a buckled nanotube [65]. . . . .   | 15 |

---

|      |   |    |
|------|---|----|
| 2.11 | Evolution of a particular (5-7-7-5) defect from a classical simulation for a (10,10) armchair nanotube at 2000 K under 10% uniaxial strain. (a) The hexagonal lattice with two heptagons and pentagons coupled in pairs. (b)The defect splits and starts diffusing. (c) Another bond rotation has led to the formation of a (5-7-5-8-5) defect [67]. . . . .    | 16 |
| 3.1  | Schematic drawing of the arc-discharge method. In order to keep constant current between the cathode and the evaporating anode, the cathode is moved downwards during the reaction. . . . .   | 20 |
| 3.2  | (a) the arc-discharge product (b) hard shell (c) soft core. . . . .   | 20 |
| 3.3  | The arc-discharge apparatus in our laboratory. Graphite electrodes are in the middle opposing to each other. The water cooled soot collector is on the left hand side. . . . .  | 21 |
| 3.4  | Synthesis of carbon nanotube ropes by laser ablation of a graphitic target. SWNT bundles are collected on the cooled collector [58]. . .  | 22 |
| 3.5  | CCVD furnace. The catalyst particles are introduced in a quartz boat into the hot (700°C) furnace. Nanotubes grow over the catalyst via decomposition of acetylene. . . . .   | 23 |
| 3.6  | Schematic of the applied flame synthesis method in the experiment of Height et al. [90]. The premixed catalyst and the carbon source are burnt in a closed chamber under moderate vacuum. Vertical translation of the burner stage allows sampling at a series of heights above the burner. The product is collected in the upper part of the chamber . . . . . | 24 |
| 3.7  | CCVD growth model of the nanotubes. (a) the tip and (b) the bottom growth of CNTs. Depending on the adhesion force between the particle and the substrate, the catalyst can be pushed up by the growing nanotube (a) (tip growth) or the carbon diffusion continues from the bottom (b) (bottom growth). . . . .  | 26 |
| 3.8  | An encapsulated catalyst particle, SWNTs and soot structures obtained between 530°C and 1130°C. Iron atoms are represented as balls and carbon atoms as a stick-like structure [93]. . . . .  | 27 |
| 3.9  | The size effect of the catalyst particle. Simulation of growth of SWNTs from cluster of 10 to 100 Fe atoms [93]. . . . .  | 27 |
| 4.1  | Interactions between the specimen and the electrons as well as penetration depths of different generated electrons in a bulk sample inside a SEM. . . . .   | 30 |

---

|     |  |    |
|-----|--|----|
| 4.2 | A schematic drawing of a SEM microscope including the interactions between a bulk specimen and the incident e-beam. . . . .  | 31 |
| 4.3 | A schematic drawing of the interactions between an electron transparent specimen and the incident e-beam in a TEM. . . . .   | 32 |
| 4.4 | a) A simplified schematic drawing of the main components of a transmission electron microscope. . . . .  | 34 |
| 4.5 | EELS spectrum of graphite, fullerene and diamond. . . . .  | 35 |
| 4.6 | Electron diffraction pattern of a multi-walled carbon nanotube. The pattern is the superposition of the diffraction patterns produced by several isochiral clusters of tubes with different chiral angles. The direction of the beam incidence is approximately normal to the tube axis and the pattern exhibits 2mm planar symmetry [22]. . . . . | 36 |
| 4.7 | (a) A prepared TEM grid. Suspension of CNTs were dropped to the holey carbon-coated surface. (b) A magnified part of the grid shows nodes of CNTs. . . . .   | 36 |
| 5.1 | Rotary tube furnace. . . . .   | 40 |
| 5.2 | The as-prepared catalyst, supported catalyst and the MWNT powder. 10 minutes heat treatment under nitrogen atmosphere results in the supported catalyst. MWNTs grew over the supported catalyst after 30 minutes of acetylene exposure. . . . .  | 42 |
| 5.3 | Evolution of the purified product mass versus the supported Co( $\xi$ )-Fe content of the catalyst in the alloy of Fe <sub>1-<math>\xi</math></sub> Co $\xi$ /CaCO <sub>3</sub> . Curves correspond to 30 minutes growth at 700°C, 720°C and 740°C, respectively . . . . .   | 42 |
| 5.4 | X-ray Powder Diffraction patterns. For each composition, two diagrams of the products are presented: ① annealed for 10 min under N <sub>2</sub> and ② 10 min N <sub>2</sub> exposure was followed by 10 min N <sub>2</sub> /C <sub>2</sub> H <sub>2</sub> . . . . .  | 44 |
| 5.5 | The flowchart of the heat treatment of the as-prepared catalyst in the case of 33 mol% of cobalt content. . . . .  | 45 |
| 5.6 | The flowchart of the heat treatment of the as-prepared $\xi < 33$ mol% catalyst. . . . .   | 45 |
| 5.7 | The flowchart of the heat treatment of the as-prepared $\xi > 33$ mol% catalyst. . . . .   | 46 |
| 5.8 | SEM micrograph of CCVD nanotubes grown at 33 mol% 660°C for 30 minutes. . . . .  | 46 |

---

|      |  |    |
|------|--|----|
| 5.9  | TEM micrograph of purified CCVD nanotubes grown at different cobalt contents of catalyst: (a) 0 mol%, (b) 25 mol%, (c) 33 mol%, (d) 50 mol%, (e) 75 mol%, (f) 100 mol%. . . . .  | 47 |
| 5.10 | TEM micrograph and EELS spectrum of an encapsulated particle. MWNT was grown on $\text{Fe}_{0.75}\text{Co}_{0.25}$ catalyst. . . . .   | 48 |
| 5.11 | The obtained nanotubes on earth carbonates as a function of their decomposition temperature in the case of 100 mg $\xi = 33$ mol% as-prepared catalyst, at $700^\circ\text{C}$ for 30 minutes. . . . .   | 49 |
| 5.12 | SEM micrographs of the CNTs obtained on $\xi = 33$ mol% catalyst supported by earth alkaline supports (a) $\text{MgCO}_3$ , (b) $\text{CaCO}_3$ , (c) $\text{BaCO}_3$ and (d) $\text{SrCO}_3$ . . . . .  | 50 |
| 5.13 | $\text{CO}_2$ content of $\text{CaCO}_3$ versus temperature from TGA analysis. . . . .   | 51 |
| 5.14 | Carbon yield in function of growth temperature. . . . .  | 51 |
| 5.15 | High temperature growth of “nanotubes”. At $1000^\circ\text{C}$ the acetylene decomposes spontaneously forming thick fibers. . . . .   | 52 |
| 5.16 | The amount of the nanotubes produced as a function of time at three different temperatures. CNTs were grown over 50 mg of $\text{Fe}_2\text{Co}/\text{CaCO}_3$ catalyst. . . . .   | 53 |
| 5.17 | The calculated Gibbs energies for all the reaction equations listed above. . . . .   | 55 |
| 6.1  | Nanotube response to resonant alternating applied potentials. (a) In the absence of a potential, (b) at the fundamental mode of vibration and (c) the second harmonic. . . . .   | 59 |
| 6.2  | Mechanical resonance of a nanotube in an applied electric field [56].  | 59 |
| 6.3  | (a) High-resolution TEM image of a thick, bent nanotube showing a characteristic wave-like distortion – rippling. (b) and (c) are magnified views of a portion of (a) [56]. . . . .  | 60 |
| 6.4  | (a) AFM image of a SWNT rope adhering to the polished alumina ultrafiltration membrane, with a portion bridging a pore of the membrane. (b) Schematic of the measurement: the AFM is used to apply a load to the nanobeam and to determine directly the resulting deflection [12]. . . . . | 61 |
| 6.5  | Schematics of the four-contacts measurement. The resistance ( $R_B$ ) measured between the two middle contacts and the calculation of the resistivity ( $\rho$ ) is based on equation (6.5). . . . .   | 62 |

|      |  |    |
|------|--|----|
| 6.6  | A scanning electron microscope image of a multiwall nanotube lying across four gold electrodes. Contacts were fabricated by electron-beam lithography prior to the deposition of the nanotube [116]. . . .   | 63 |
| 6.7  | (a) SEM image of the obtained SWNT forest. (b) Magnified image of the SWNT forest edge [99]. . . . .   | 64 |
| 6.8  | SEM micrograph of the SWNT strand from the article of Zhu [117].   | 65 |
| 6.9  | Schematic drawings about the three main type spinning process. . .   | 66 |
| 6.10 | Schematic of the setup for producing carbon nanotube fibres by solution spinning. Suspension of purified nanotubes in SDS solution is introduced into a spinning beaker containing PVA. The nanotube suspension is destabilised by PVA and the nanotubes coagulate into fibres aligned with the flow direction. (b) A scanning electron micrograph showing a portion of the nanotube fibre [108]. . . . .  | 68 |
| 6.11 | Electrophoretic SWNT fibre production setup. A potential of 1-2 V is applied between the commercial carbon fibre and the platinum counter-electrode for 10-30 min, leading to the formation of an ordered SWNT cloud. When the carbon fibre is slowly withdrawn from the solution it “draws” the aligned SWNT fibre [118]. . . . .   | 70 |
| 6.12 | SEM image of a CNT yarn in the process of being simultaneously drawn and twisted during spinning from a nanotube forest outside the SEM. . . . .   | 71 |
| 6.13 | A scanning electron micrograph showing a portion of the nanotube fibre, single and four plied [110]. The single yarn was $3.2 \mu\text{m}$ . . . .   | 71 |
| 6.14 | Two possible types of cross-link (a) and (b) promoting divacancies in graphite, from the paper of Telling et al. $V_2^1(\beta\beta)$ and $V_2^2(\beta\beta)$ the first and the second nearest interplane-neighbour divacancy configurations allow bonding between the twofold coordinated carbon atoms. Corresponding bond lengths are $1.43\text{\AA}$ and $1.38\text{\AA}$ . The fourfold coordinated interstitial (c) (bond lengths are $1.49\text{\AA}$ each), that can occur when the basal planes are shifted by half a bond length ( $0.71\text{\AA}$ ) from their equilibrium configuration [133]. . . . . | 74 |
| 6.15 | An isolated SWNT exposed to a low-intensity $1 \left(\frac{\text{\AA}}{\text{cm}^2}\right)$ 200 keV electron beam. Atom extraction from the surface leads to a series of surface reconstructions in which the nanotube diameter decreases from the original value of 1.4 nm (a) to 0.4 nm (f) before eventually breaking [138] after half an hour of irradiation. . . . .  | 75 |

|      |  |    |
|------|--|----|
| 6.16 | (a) HRTEM image of a nanotube bundle before and (b) after a couple of seconds under a high-intensity 1.25 MeV electron beam [140]. . . . .   | 76 |
| 6.17 | Evolution of the morphology of a carbon nanotube rope under intense electron beam irradiation. The acceleration voltage was 80 kV and the current density $0.4 \frac{\text{A}}{\text{cm}^2}$ . Corresponding doses are: $3.4 \times 10^{20}$ , $17 \times 10^{20}$ and $67 \times 10^{20} \frac{\text{electron}}{\text{cm}^2}$ [13]. . . . . | 77 |
| 6.18 | (a) The motor driven translational stage with the negative electrode around the 1 wt% of SWNT/DMF suspension and four positively charged graphite electrodes immersed into the suspension. (b) After six hours of pulling, long fibres appear on the electrodes. . . . .   | 78 |
| 6.19 | SWNT rope, (a) small magnification and (b) high resolution scanning electron micrograph. . . . .   | 79 |
| 6.20 | Scanning electron micrograph of SWNT (a) and MWNT (b) rope using PmPV/toluene solution. . . . .  | 79 |
| 6.21 | Scanning electron micrograph of MWNT/polypropylene fibre smaller (a) and higher (b) magnification. . . . .   | 80 |
| 6.22 | Schematic drawing of the non-destructive elastic modulus measurement. The fiber is shaken by an amplified random noise signal. The digital signal analyser compares the signal from the amplifier and the response of the fiber. . . . .   | 81 |
| 6.23 | Frequency response curve of a carbon nanotube rope. The peak at 50 Hz is line pick-up. The peak at 487.5 Hz corresponding to the resonant frequency of the fibre, which accords with the value 5.3 GPa based on equation (6.6). . . . .  | 82 |
| 6.24 | Temperature dependence of the electrical resistivity of the SWNT fibre. The resistivity of SWNT fibre as a function of temperature indicating hopping-like conduction [146]. . . . .   | 83 |
| 6.25 | (a) TEM specimen holder with electrical contacts. (b) A SWNT fiber is mounted on a TEM ring (in the middle) which is placed and contacted to the specimen holder. . . . .  | 84 |
| 6.26 | The resistivity of a SWNT fiber as a function of electron irradiation time. After 35 minutes of electron irradiation, the fibre reached the minimum of resistivity. The step-like variation towards the end of the irradiation is the result of the stepwise moving of the irradiated zone along the sample. . . . .                         | 85 |

---

|      |  |     |
|------|--|-----|
| 6.27 | The resistivity of pristine and irradiated nanotubes as a function of temperature. The temperature dependence indicates hopping-like conduction. . . . .   | 86  |
| 6.28 | TEM images of the rope before (a) and after (b) the irradiation experiment. Before irradiation, the CNT wall structure of parallel layers of graphene sheets is clearly visible. After irradiation the wall structure is fully destroyed. . . . .  | 87  |
| 6.29 | Four-probe electric measurement as a function of irradiation time. . . . .   | 89  |
| 6.30 | <i>In situ</i> Young's modulus measurement during UV illumination of the SWNT fibre. The UV lamp is on the left hand side, the SWNT fibre is attached to a loudspeaker and hanging on over a transducer. The frequency response is evaluated by a digital analyser (on the right hand side). . . . . | 90  |
| 6.31 | Frequency response curves of a carbon nanotube rope at different irradiation times. Note the shift of the resonance from 450 Hz to 950 Hz upon 60 seconds of ultraviolet irradiation. The peak at 50 Hz is line pick-up. . . . .   | 90  |
| 6.32 | TEM image of a SWNT fiber before (a) and after UV irradiation (b). Note that there is no sign of amorphisation of the nanotubes. . . . .   | 91  |
| A.1  | TEM micrograph of nanotubes produced by CVD. (a) represents a good purification process while (b) shows the nanotube walls damaged by purification. . . . .  | 98  |
| A.2  | Schematic drawing about the reflux purification of CNTs . . . . .  | 99  |
| A.3  | Schematic drawing of the mechanical purification scheme [157]. . . . .   | 100 |
| A.4  | (a) magnetic particles enclosed in graphitic shells. (b) after 24 hours of sonication in the presence of ZrO <sub>2</sub> [157]. . . . .   | 100 |
| A.5  | Results of surfactant purification in the method of Bonard et al. [158]. Raw nanotubes (a) were dispersed in the aqueous suspension of an anionic surfactant followed by filtration resulting in separation of nanotubes from impurities (b). . . . .  | 101 |
| A.6  | TEM images of the supramolecular organisation of the SDS molecules on CNTs. . . . .  | 102 |
| A.7  | SEM micrograph of raw CCVD nanotubes at (a) 4000 and (b) 8000 magnification. The large and small white spots are most probable the calcium carbonate and catalyst particles, respectively. . . . .   | 103 |
| A.8  | SEM micrograph of purified samples from the CCVD furnace with a dense mat of CNTs. a) 5000 and (b) 20000 magnification. . . . .  | 103 |

|      |  |     |
|------|--|-----|
| A.9  | High resolution TEM picture of (a) raw and (b) purified CCVD nanotubes. . . . .                              | 104 |
| A.10 | SEM and TEM micrographs of raw AD nanotubes. . . . .   | 105 |
| A.11 | (a) SEM and (b) TEM micrographs of the purified AD nanotubes. . . . .  | 106 |
| B.1  | The graphical user interface (GUI). . . . .  | 109 |
| B.2  | DDAS takes over control from the analyser and interrogates it for dumping data in ASCII format. . . . .      | 109 |
| B.3  | Separating the header from the measured data, from which the phase and the magnitude are calculated. . . . . | 110 |
| B.4  | Automated archiving in ASCII format. . . . .   | 111 |
| B.5  | LCL gives back control to the analyser. . . . .  | 112 |



# Chapter 1

## Introduction

“At any rate, it seems that the laws of physics present no barrier to reducing the size of computers until bits are the size of atoms, and quantum behavior holds dominant sway.”

(R. Feynman)

As we can read in the Feynman’s statement [1], the interest to miniaturise and speed up devices that we use in our everyday life began many years ago and attracted many researchers to work on this effort. In particular, the discovery of carbon nanotubes (CNTs) and other nanometre-scale structures has been one of the driving forces for nanotechnology and has opened new fields in physics, chemistry, biology, and materials science. Currently, they represent one of the most rapidly expanding, challenging areas of research that crosses many borders between areas of natural sciences.

Nanometre-scale structures are usually defined as systems in which at least one dimension is below 100 nm. 1D representatives such as nanowires or nanotubes have nanometre-scale diameter but may have a micron range dimension [2]. In the last decades the interest in CNTs has grown exponentially, because they have been recognised as an excellent material for nanotechnological applications due to their extraordinary physical properties. For instance, CNTs have been proposed as new materials for organic field emission devices, organic field effect transistors, electron emitters in flat displays by Samsung, simple molecular transistors, Scanning Probe Microscopy (SPM) tips [3], or gas and electrochemical energy storage devices, high frequency capacitors, quantum resistors, nano-tweezers, artificial muscles, molecular electronic devices, nanomotors, nanorotators etc.. In addition, CNTs have proven to be excellent candidates for field emission gun tips in electron microscopes [4],

and can also be employed as a conductive transparent layer [5] for optoelectronic applications, for example in the next generation of flexible displays [6]. Currently, significant efforts are made in order to transfer their unique properties from the laboratory into industrial applications. However, for most of the applications it is essential to have pure, well-graphitised<sup>1</sup> and in some cases aligned or patterned CNTs. In spite of tremendous progress, nanotube growth is not yet fully understood and consequently full control of the synthesis remains inaccessible.

This PhD work aims at the understanding of the growth mechanism of CNTs and their application in macroscopically assembled fibers. Macroscopic fibers currently represent one of the most promising applications of CNTs because the assembly is relatively simple. Moreover, in fiber form CNTs can be a starting point for construction of novel, macroscopic structures which largely exhibit the excellent axial properties of individual tubes. An important precondition of this application is obviously the synthesis of CNTs with high quality and high yield at low cost. Therefore the first task was to investigate CNT growth by using the catalytic chemical vapour deposition technique and to find out the parameters which play an important role for CNT characteristics and yield.

The second task corresponded to the assembly of CNTs into macroscopic fibers in order to exploit the extraordinary mechanical property of CNTs. In general, macroscopically aligned arrays of CNTs show a significant enhancement of the mechanical, electrical and thermal properties compared with the random tangles of bundled tubes typically found in as-grown bulk samples [7, 8, 9, 10, 11]. Therefore one of the challenges is to improve the degree of CNT alignment [10]. Orientation of nanotubes embedded into a polymer matrix can be solved starting from an isotropic soot by way of alignment in a macroscopic fiber. In the context of this work, macroscopic fibers consisting of aligned SWNTs and MWNTs in a polymer matrix were achieved. In addition, SWNTs were also assembled into fibres by using a polar solvent.

From the mechanical point of view, ropes of SWNTs are weakly coupled to each other by van der Waals interaction [12]. Consequently, the mechanical strength of a macroscopic nanotube fiber is limited by the small intertube shear modulus: The fiber would be torn apart before the individual nanotubes would break. Therefore the Young's modulus of the fiber is not as high as expected from the Young's modulus of individual SWNTs. In this work, the effect of electron and ultraviolet radiation on Young's modulus and electrical conductivity was studied *in situ*. In particular, the reinforcement achieved is compared with the reinforcement measured

---

<sup>1</sup>Possess perfect hexagonal lattice in the sidewall as present in graphite.

by A. Kis in individual CNTs after electron irradiation [13].

This thesis is organized as follows: This short introduction is followed by a short overview of the physical properties of carbon nanotubes. An overview including the principles of different growth methods of carbon nanotubes is given in Chapter 3 followed by a short Chapter 4 describing the basic principles of the main characterization techniques (SEM, TEM, XRPD and TGA) applied. The next two chapters (Chapter 5 and 6) present the main experimental results obtained within this thesis: Chapter 5 contains the main experimental results on the CNT growth studies. Chapter 6 involves the assembly of CNTs into macroscopic fibres as well as the electron and ultraviolet light irradiation experiments. The former part contains a detailed overview of alignment techniques reported as well as a description of the technique applied in this thesis. The results of the measurements of the electronic and the mechanical properties are presented together with the previously published work on the measurement of the mechanical and the electronic properties of individual nanotubes or their bundles. The latter part illustrates the irradiation effects on CNT fibres. In a short section, the irradiation effects on carbon nanostructures and graphite, which provide a theoretical basis for the mechanism of reinforcement of the CNT fibers under electron and ultraviolet irradiation are reviewed. *In situ* mechanical and electric conductivity measurements proved to cross-link CNTs and/or their bundles. A detailed description of the non-destructive Young's modulus measurement is given in Appendix B. An enhancement of the mechanical and electrical properties via irradiation is an important first step in their future applications.



## Chapter 2

# Physical Properties of Carbon Nanotubes

### 2.1 Allotropes of carbon

Carbon is one of the most important elements in nature. It can combine with itself and other elements in three types of hybridisations. This gives a rich diversity of structural forms with variable and unique physical properties and is the basis of organic chemistry and life. Up to now, one non-crystalline and four crystalline groups of the allotrope modification of carbon have been discovered <sup>1</sup>. The non-crystalline phase represents the amorphous carbon, which has – as all glassy materials – some short range ordering but no long-range ordering of the structure (Figure 2.1a).

Carbon has the electronic ground state configuration  $1s^2 2s^2 2p^2$  and can form  $sp^3$ ,  $sp^2$  and  $sp^1$  hybrid bonds. In the  $sp^3$  hybridisation four equivalent  $2sp^3$  hybrid orbitals are tetrahedrally oriented around the atom and can form four equivalent  $\sigma$  bonds by an overlap with orbitals of other atoms. The transparent cubic diamond configures in this tetrahedral array of  $sp^3$   $\sigma$  bonds with a C-C bond length of 1.544 Å (Figure 2.1b).

In the  $sp^2$  hybridisation three equivalent  $sp^2$  orbitals are formed and one unhybridised  $2p$  orbital is left. Graphite – also known as plumbago or black lead – hybridises into  $sp^2$  configuration. The  $sp^2$  orbitals are coplanar and oriented at  $120^\circ$  to each other and form very strong  $\sigma$  bonds by overlapping with orbitals of neighbouring atoms whereas the remaining unhybridised  $\pi$  orbital forms a  $\pi$  bond by the overlap with the  $2p$  orbital from the neighbouring C atom. The weak interlayer bonding of graphite originates from the small overlap of these  $\pi$  orbitals and causes

---

<sup>1</sup>Wikipedia<http://www.answers.com/library/Wikipedia-cid-367390454>

easy sliding of the layers relative to each other.

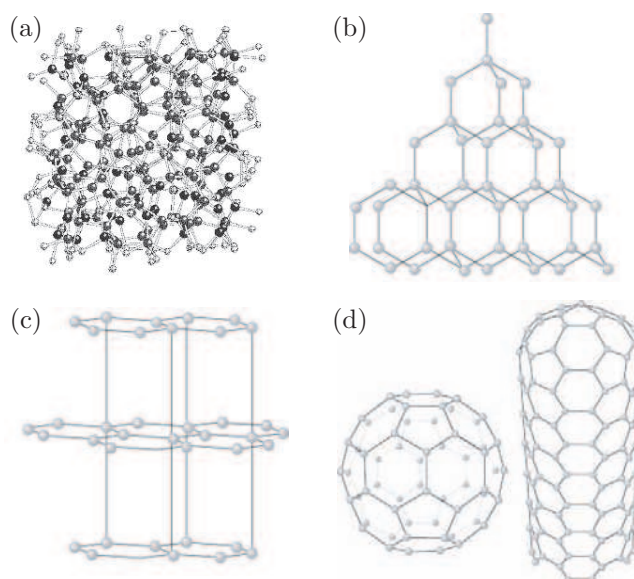


Figure 2.1: Allotropes of carbon: Structural model of (a) black carbon soot, (b) transparent diamond, and (c) graphite. (d) shows a fullerene (C<sub>60</sub>) and an end of a carbon nanotube.

From the physical point of view, the cubic diamond with  $sp^3$  configuration is a wide-gap semiconductor (5.47 eV) and the hardest material in nature, whereas graphite with  $sp^2$  hybridisation is conducting parallel to the  $\sigma$  bond planes. On the other hand, ceraphite<sup>2</sup> – also known as white carbon – is one of the softest substances known to mankind and has more than one index of refraction. The lowest gravimetric density ( $\sim 2$  mg/cm<sup>3</sup>) ever reported for a solid has been measured in carbon nanofoam, which has a fractal-like structure consisting of carbon clusters randomly interconnected into a web-like foam [14].

In 1985, with the discovery of C<sub>60</sub> by Kroto, Curl and Smalley [15], a novel group has been added to the class of carbon materials (Figure 2.1), which contains fullerenes<sup>3</sup> and CNTs. Fullerenes are cage-like, hollow molecules that are composed of hexagonal and pentagonal groups of carbon atoms. The smallest possible fullerene molecule may have 32 carbon, although fullerene-like molecules (lacking a hexagonal face) with about 20 carbon atoms have also been observed. Much larger fullerenes also exist containing 180, 190, 240, and 540 carbon atoms. Meanwhile fullerenes with 60, 70, 76, 84, 90, and 96 carbon atoms can nowadays be produced

<sup>2</sup><http://www.radiochemistry.org/periodictable/elements/6.html>

<sup>3</sup>After Richard Buckminster Fuller (from the resemblance of the configurations of the carbon atoms to his geodesic domes) + “ene” (an unsaturated organic compound, especially one containing a double bond between carbon atoms, like in *acetylene*).

in macroscopic amounts.

CNTs are cylindrical carbon molecules with a diameter around 1 nm and a length of up to microns. The first observation was made in a transmission electron microscope (TEM) by Endo [16] already in 1976 (Figure 2.2), followed by Iijima in 1980 [17]. However, their structure and significance for nanotechnology were discussed for the first time in 1991 by Iijima [18].

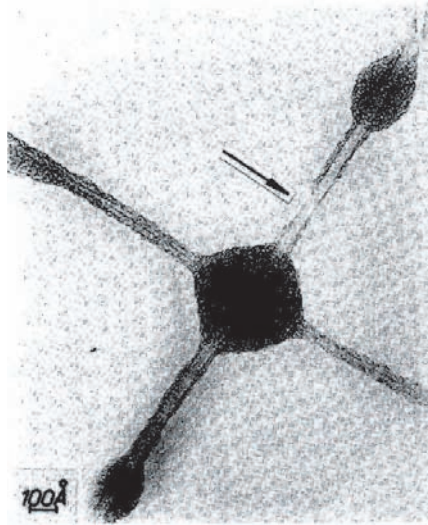


Figure 2.2: The first TEM micrograph of branching nanotubes by Endo [16].

Nanotubes possess a unique combination of small size, low density, high strength and a broad range of electronic properties from metallic to semiconducting.

## 2.2 Basic structures of nanotubes

From a structural point of view CNTs can be described by rolling up the graphene – a single layer of graphite – into a cylinder (Figure 2.3).

The “rolling-up” is described by a chiral vector  $\vec{C}_h$ , whose length corresponds to the tube’s circumference, as shown in Figure 2.3. The chiral vector is expressed as:

$$\vec{C}_h = n \vec{a}_1 + m \vec{a}_2 \equiv (n, m), \quad (2.1)$$

where the integers  $n$  and  $m$  represent the chiral indices, while  $\vec{a}_1$  and  $\vec{a}_2$  are those unit vectors which span the unit cell of the hexagonal lattice.

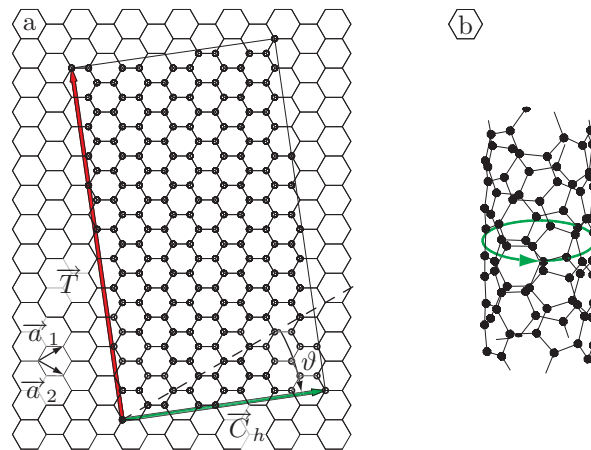


Figure 2.3: (a) The hexagonal graphene sheet with the base vectors  $\vec{a}_1$  and  $\vec{a}_2$ , translational vector  $\vec{T}$ , chiral vector  $\vec{C}_h$  and chiral angle  $\vartheta$ . The chiral vector is defined on the honeycomb lattice of carbon atoms by unit vectors and the chiral angle with respect to the zigzag axis. Along the zigzag axis  $\vartheta=0^\circ$ . (b) A SWNT is formed when the ends of the chiral vector  $\vec{C}_h$  are put together. The circumference of the tube is given by the vector  $\vec{C}_h$ .

The atomic structure of the nanotubes can be classified according to the  $\vec{C}_h$  chiral vector or the  $\vartheta$  chiral angle, since both of them describe the “twist” of the nanotube lattice. The chiral angles are in the  $0$  to  $30^\circ$  interval, where the limits are referred to “zigzag”  $(n, 0)$  and to “armchair”  $(n, n)$  nanotubes, respectively, see Figure 2.4a-c.

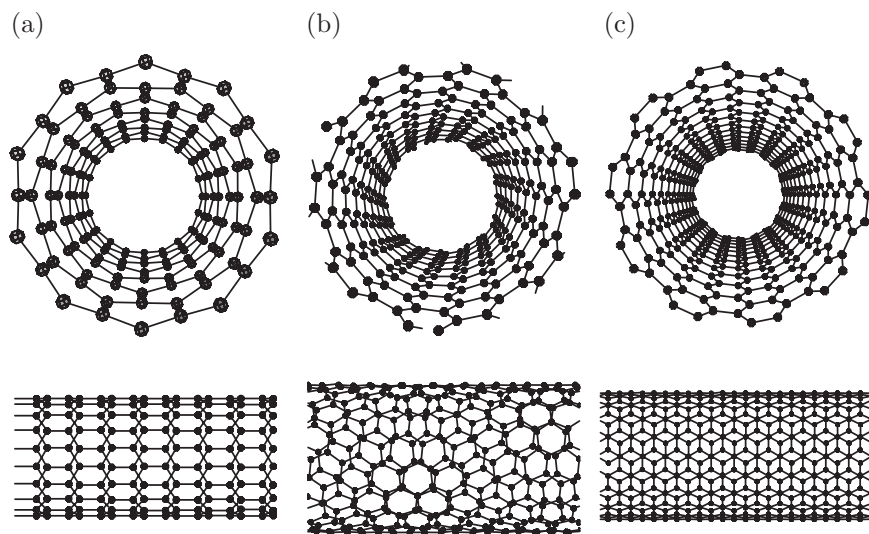


Figure 2.4: Zigzag (a), chiral (b) and armchair (c) nanotubes.



The diameter  $d$  of the nanotube is given by  $d = \frac{L}{\pi}$  equation, where  $L$  is the length of the chiral vector or the circumferential of the nanotube and

$$L = \left| \vec{C}_h \right| = a \sqrt{n^2 + m^2 + nm} \quad (2.2)$$

where  $a = 2.49\text{\AA}$  is the lattice constant of graphite. (The nearest neighbour distance between carbon atoms in graphite is  $1.42\text{\AA}$ .)

Experimentally the nanotube chirality has been determined either directly from atomically resolved scanning tunnelling microscopy (STM) [19], transmission electron microscopy (TEM) [20] or from raman spectroscopy [21] images or from electron diffracted patterns [22, 23]. Because of inhomogeneities in production, CNTs always have a diameter distribution involving chiralities.

Multiwall carbon nanotubes (MWNTs), see Figure 2.5a-c, contain several coaxial cylinders, each cylinder being a single-wall carbon nanotube.

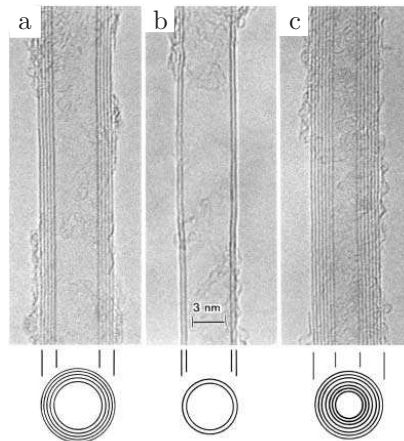


Figure 2.5: The “discovery” of CNTs. Bright field TEM images of multi-walled CNTs from Iijima’s seminar paper [18].

The interlayer spacing can range from  $0.342\text{ nm}$  to  $0.375\text{ nm}$ , depending on the diameter and number of shells comprising the tube [24]. For comparison, the interlayer of graphite is  $0.335\text{ nm}$ . This suggests a relatively weak interaction between individual shells, also confirmed by studies of mechanical and electronic properties of CNTs [25].

### Exotic CNT-type structures

The discovery of CNTs in 1991 stimulated scientists’ fantasy as well and countless new carbon structures turned up. Some instances for the extraneous carbon forms (see also Figure 2.6) are:

Nanotubes of helical shape have regular pitch and helix which looks like a nano-telephone cord (Figure 2.6f). They been produced using a particular catalyst preparation over silica supported Co catalyst [26]. According to the results obtained over catalysts prepared by impregnation, quality of the coils strongly depends on the pH of the initial solution and on the pretreatment during catalyst preparation. Graphite micro-matches (Figure 2.6a) were grown on a high temperature superconductor<sup>4</sup> as a substrate [27]. Graphite cones (Figure 2.6c) were achieved with very sharp tips by Microwave Plasma Enhanced Chemical Vapour Deposition [28]. By adding other elements to the carbon nanotubes such as boron or nitrogen, bamboo structure nanotubes are formed [29, 30] instead of straight ones.

The CNTs can be opened by heat treatment and filled with different elements such as metals [31], salts or fullerenes [32] (Figure 2.6d and g). Using CNTs as a template, low-dimensional inorganic nanocrystals have been grown [33].

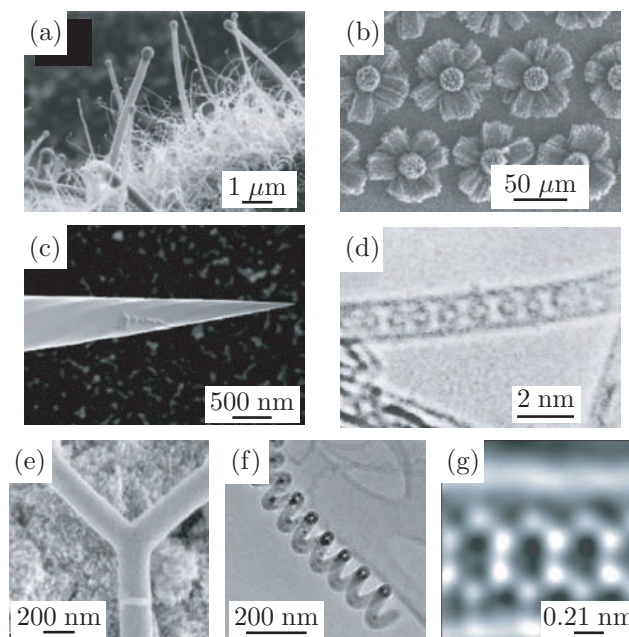


Figure 2.6: Exotic CNT structures

## 2.3 Electronic properties of CNTs

The chirality of CNTs has a significant influence on their properties. Even a small change of diameter can drastically alter their conductivity from metallic to semi-conducting [34]. This interesting electrical property of CNTs is due to the peculiar electronic structure of the graphene and it can be deduced by taking into account

<sup>4</sup> $\text{Bi}_2\text{Sr}_2\text{CaCu}_2\text{O}_8$  and  $\text{Bi}_2\text{Sr}_2\text{YCu}_2\text{O}_8$

the confinement of the electrons around the circumference of the CNT. It was shown that an  $(n,m)$  nanotube is metallic as accounts that:  $2n + m = 3i$ , where  $i$  is an integer and  $n$  and  $m$  define the nanotube [35, 36, 37, 38]. All the rest of the tubes will be either large or small-gap semiconductors. The energy gaps of semiconducting tubes depend inversely on diameter as  $1/d$ . Due to the  $\sigma - \pi$  band mixing, a small gap will open in the case when  $i$  is nonzero, with a  $1/d^2$  dependence [39, 40, 41]. The resistance to conduction is determined by quantum mechanical aspects and was proved to be independent of the nanotube length [42].

Because of the insufficiency in the SWNT production, the as-product SWNTs are always a mixture of semiconducting and metallic tubes. Separation of nanotubes is a serious obstacle for application in electronic devices and is still not in daily practice. In principal, there would be two possible solutions:

1. size selective growth, which means to gain complete control over the diameter distribution during production by using catalytic particles of a well-determined size,
2. post-selection, which separates different tubes after production [43, 44].

MWNTs are more complex objects than the SWNTs in that each one of their carbon shells can have different electronic character and chirality. However, in studies of MWNTs with a metallic outer shell that are side-bonded to metal electrodes, it was concluded that electrical transport at low energies is dominated by outer-shell conduction [45]. These systems show 1D or 2D characteristics, depending on their diameter and the nature of the property examined.

## 2.4 Chemical reactivity of CNTs

The chemical reactivity of a CNT is, compared with a graphene sheet, enhanced as a direct result of the curvature of the CNT surface (Figure 2.7) [46, 47].

A SWNT consists of two separate regions with different physical and chemical properties.

- The chemically more reactive zone is the end cap, which contains C-atoms placed in hexagons and pentagons to obtain a closed cage structure [48, 49]. According to the isolated pentagons rule, the distance between pentagons on the fullerene shell is maximised in order to obtain a minimal local curvature and surface stress.
- The less reactive region is the hexagonal sidewall, which is generated by wrapping the graphene sheet in a certain direction [50].

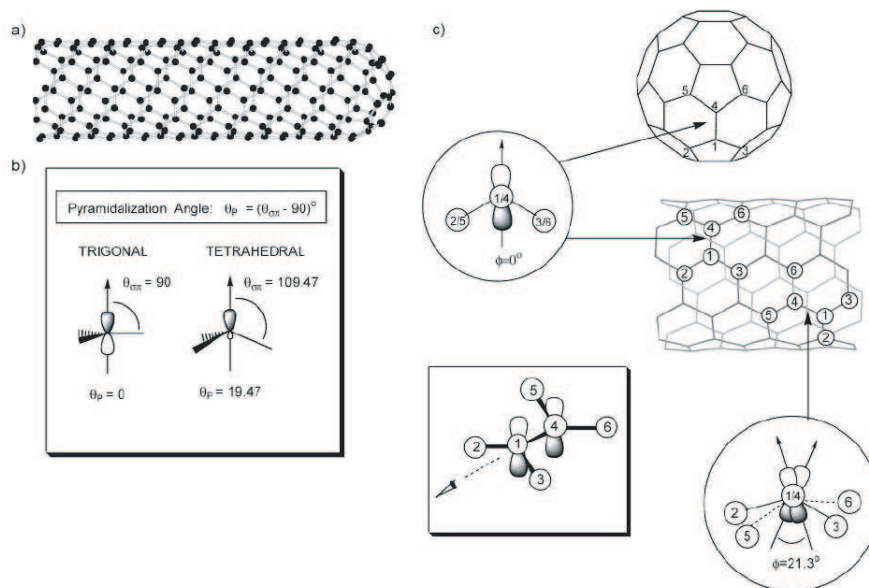


Figure 2.7: The chemical reactivity of CNTs is described by the  $\pi$ -orbital mismatch. Diagrams of (a)  $\pi$ -orbitals of a graphene sheet, (b) pyramidalization angle ( $\theta_P$ ), and (c) the  $\pi$ -orbital misalignment angles ( $\phi$ ) along the  $C_1 - C_4$  in the (5,5) SWNT and its capping fullerene,  $C_{60}$  from reference [47].

Normally, the chemical reactivity is mainly determined by the sidewall reactivity because the sidewalls are long compared to the small end caps. Hence, CNT reactivity is directly related to the  $\pi$ -orbital mismatch caused by an increased curvature. For the same reason, a smaller nanotube diameter results in increased reactivity. Covalent chemical modification of either sidewalls or end caps has been possible. By functionalisation [51] or polymer wrapping [52], for instance, the solubility of CNTs in different solvents can be controlled.

## 2.5 Mechanical properties

Since their discovery, CNTs have attracted the attention of many scientists and engineers worldwide, particularly because of their high stability, strength and stiffness, combined with low density and elastic deformability. Theoretical [53] and experimental [54, 12] studies have shown that individual CNT can undergo enormous bending deformation and recover elastically [55, 54, 56]. The initial measurements of the Young's modulus of CNTs have confirmed the theoretical expectation close to 1 TPa, similar to the in-plane modulus of graphite [12, 57]. These measurements have pointed out that special care is needed to produce CNTs with highly ordered structure, because structural defects may considerably reduce their me-

chanical properties [57].

Another drawback is that SWNTs often bundle up in the exterior of crystalline ropes during the production [58], and the single tubes are held together by weak van der Waals interaction.

The mechanical properties of ropes of CNTs are comparable with that of graphite. Strong  $sp^2$ -hybridised  $\sigma$ -bonds with a length of  $1.42\text{\AA}$  give an exceptionally high Young's modulus in-plane, but out of the plane  $\pi$ -bonds are responsible for the weak, van der Waals interlayer binding.

Lu et al. [59] have reported theoretical studies of the elastic properties of CNTs by using an empirical pair potential. In this model, the atomic interactions near the equilibrium structure are approximated by the sum of pairwise harmonic interatomic potentials. The interwall interaction ( $U(r)$ ) in MWNTs and SWNT ropes was modelled by summing pairwise van der Waals interaction:

$$U(r) = 4\varepsilon \left[ \left( \frac{\sigma}{r} \right)^6 - \left( \frac{\sigma}{r} \right)^{12} \right] \quad (2.3)$$

with the parameters  $\sigma = 0.34$  nm and  $\varepsilon = 12$  meV. The applied parameters were developed for intraplane interactions in graphite, and therefore do not take into account changes in bond rehybridisation due to changes in diameter. The Young's modulus was calculated from the second derivative of the strain energy density with respect to strains. The nanotube's wall thickness was chosen to be equal to the interwall distance in MWNT ( $t = 0.34$  nm), close to the interlayer distance in graphite ( $t = 0.335$  nm). The Young's modulus was found to be  $0.97$  TPa, and practically independent of the tube's diameter and chirality (in the range of  $0.68$ - $27$  nm).

Theoretical studies have revealed that the optical activity of chiral nanotubes disappears if the nanotubes become larger [60]. Therefore, it is expected that other physical properties are influenced by these parameters too. Use of the optical activity might result in optical devices in which CNTs play an important role.

### 2.5.1 Defects and deformations in carbon nanotubes

Typically, CNTs deviate from the ideal structure and contain defects. The most frequently observed are point- or planar defects, whose density strongly depends on the growth condition. By replacing hexagons with pentagons or heptagons, a defective structure can easily be created. A pentagon introduces a positive  $60^\circ$  of disclination whereas a heptagon results in negative inclination.

Pentagon-heptagon defects (Stone-Wales transformations [61]) appear in the

sidewall of the nanotube as point-defects without any inclination in the wall structure but induce local distortions away from a cylindrical towards more polygonal formations (see Figure 2.11). It is also known that high density of pentagon and heptagon defects can close the CNT. According to Euler's rule, 6 pentagons are necessary to generate the tip closure in the hexagonal network of a nanotube.

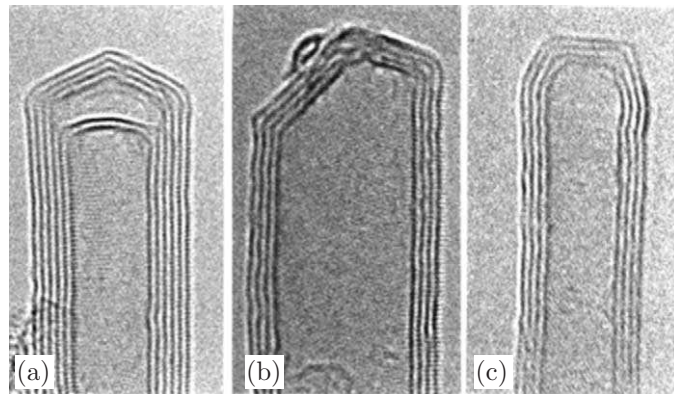


Figure 2.8: TEM micrographs of different MWNT caps the paper of Iijima [62].

The positions of the pentagons at the tips vary from one tube to another (Figure 2.8), moreover, wedged in heptagons cause a negative inclination resulting in a saddle-like structure in the tube (Figure 2.9) [48].

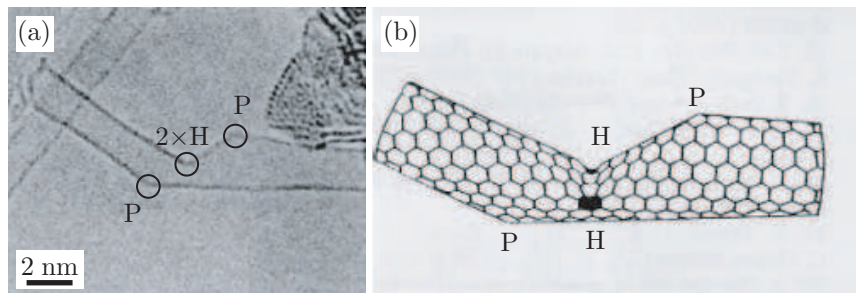


Figure 2.9: Pentagon and heptagon deformations in the hexagonal lattice indicated by letters P and H [62].

Additional structural properties of CNTs were investigated by Yakobson et al. [53]. molecular dynamics (MD) simulations were used in order to study the mechanical response of CNTs to large deformations and calculate the associated morphological changes. With properly chosen parameters, this analytical tool can predict nanotube behaviour not only at small deformations but also beyond the linear response. In the bending simulations, nanotubes have been found to be susceptible to buckling above a  $K_c$  critical curvature determined by the  $d$  tube diameter as

follows:  $K_c = \frac{0.155 \text{ nm}}{d^2}$  (Figure 2.10).

An important aspect of the MD simulations was the singular behaviour of the total energy of nanotubes as a function of strain [63]. At a small strain the energy grows as a square of the strain, in accordance with Hooke's law. However, at a certain high level of strain, the energy dropped dramatically and the qualitative behaviour changed: it varied irregularly and grew very slowly. Within the Hookean range of strain, and even at larger strains where the stress-strain relation deviates from linear, no bond breaking was observed. At a certain critical level, one of the C-C bonds broke up, leading to the formation of distinct atom chains, spanning two tube fragments, with only one chain surviving at higher strains [64].

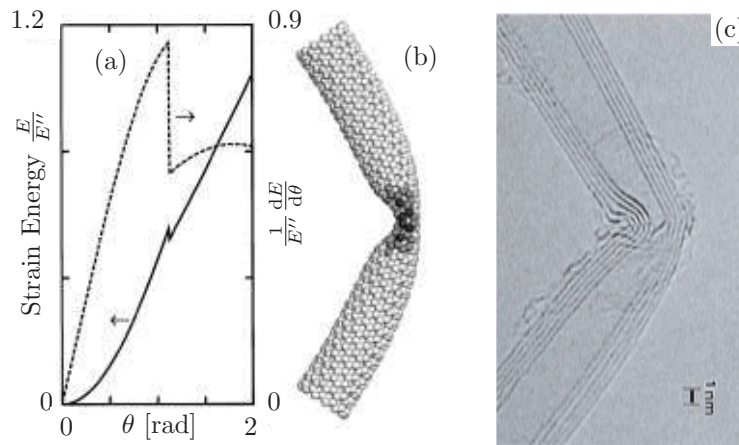


Figure 2.10: (a) The strain-energy curve for the bending of a (13,0) nanotube switches from harmonic to linear at a buckling point at the buckling angle of approximately  $57^\circ$ . The force (broken line) drops and remains almost constant. (b) MD simulation of a buckled nanotube [53]. (c) TEM micrograph of a buckled nanotube [65].

Experimental and theoretical studies by Iijima et al. [65] show that nanotube bending can be completely reversible up to angles in excess of  $110^\circ$  despite the formation of complex kink shapes. Wong et al. [66] have also observed buckling in lateral deformation of MWNTs by AFM.

The examinations of the response of CNTs to large axial strains showed that beyond a critical value of 5% axial tension the nanotube relaxes its excess strain via the Stone-Wales transformation [61]. Figure 2.11 shows the evolution of the (5-7-7-5) defect pairs. (a) represents a  $90^\circ$  rotation of the C-C bond around its center which produces two pentagons and two heptagons coupled in pairs (5-7-7-5). Increasing the strain, the defects propagate and/or more lattice imperfections are

introduced (Figure 2.11(b) and (c)).

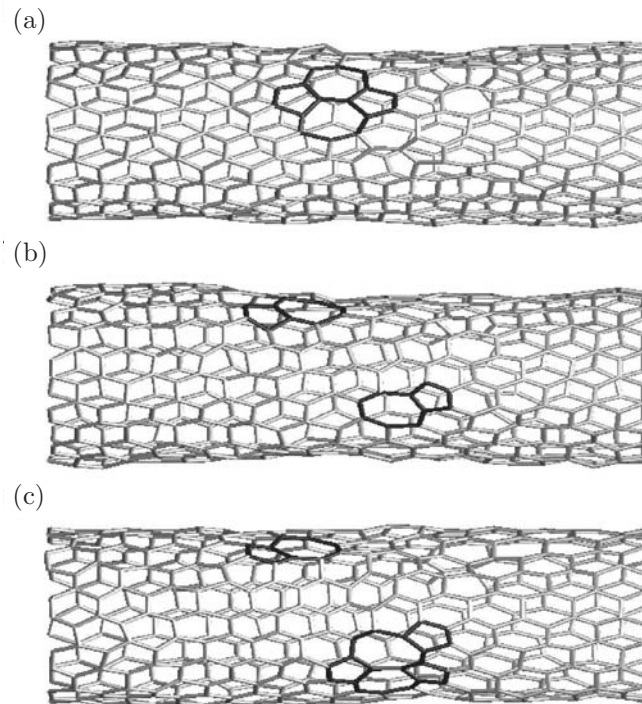


Figure 2.11: Evolution of a particular (5-7-7-5) defect from a classical simulation for a (10,10) armchair nanotube at 2000 K under 10% uniaxial strain. (a) The hexagonal lattice with two heptagons and pentagons coupled in pairs. (b) The defect splits and starts diffusing. (c) Another bond rotation has led to the formation of a (5-7-5-8-5) defect [67].

Nardelli et al. [67] pointed out the importance and the efficiency of the Stone-Wales defects under uniaxial strain via classical and quantum molecular dynamic simulations.

At zero strain, the energy is 2.34 eV *higher* in an armchair nanotube containing a Stone-Wales defect than in the ideal one. However, at 10% strain, the energy of a defective structure is 1.77 eV *lower* than in the ideal case. This demonstrates that the Stone-Wales defect is very powerful in reducing the tensile strain, since two heptagons can be stretched more than the hexagons, while keeping the C-C bond length almost constant. Moreover, the formation of a Stone-Wales defect is a reversible process [68].

As a consequence, electrical and mechanical properties of CNTs heavily depend on defects and deformations caused by impurities (mainly catalyst particles) or inhomogeneities that are generated during or after the growth process.



### 2.5.2 Potential applications

Due to their extraordinary mechanical properties, CNTs offer the potential to be employed in many different fields of applications where high strength, low weight, high elasticity and high durability are required. For instance, CNTs have been applied as tips in scanning probe microscopes in order to exploit their sharp geometry, intrinsic electrical conductivity and mechanical resilience. In comparison with commercially available silicon or gold tips, the CNT tips exhibit advanced imaging capabilities [69]. Moreover, the CNT tips are resistant to damage from tip crashes because of their flexibility. The slenderness of CNTs permits imaging high aspect ratio surface features. The nanotube tips present a solution to the common tip-wear problem and have been successfully demonstrated in lithographic oxidation of hydrogen-passivated silicon surfaces. However, attaching CNTs to the end of the tip remains a difficult task and a routine high yield production of good quality SPM tips from CNTs has not yet been achieved. Nowadays nanotube SPM tips are commercially available but expensive; therefore many researchers make an effort to automate the attaching process. Typically nanotube attachment requires a transmission or scanning electron microscope with a manipulator which enables accurate movements in nanometre scale. An alternative to the manually attached probes is to grow CNTs aligned on the cantilever by using CCVD methods. Although the *in situ* deposition of CCVD-grown tubes on SPM probes seems to be technologically easier, up to now the quality of these CNT tips have been insufficient. The mounting of arc-discharge tips one-by-one using a manipulator is time consuming but gives customer-specified, well-defined SPM probes made out of CNTs.

CNTs represent highly promising candidates for reinforcement in composite materials, where high strength and low weight are required. With a Young's modulus in the order of 1 TPa [12], nanotubes are able to sustain large strains in tension without showing signs of fracture and remain flexible perpendicular to their axes. Hence, nanotube-based composites have the potential to revolutionise structural materials for aerospace, electrical and thermal conductors for energy applications, nano-biotechnology, and other disciplines. In spite of the great efforts in exploiting the CNTs excellent mechanical properties, only few experiments showed their improved applicability compared to the traditionally used carbon fibers. Manipulation and processing of CNTs have been limited by their insolubility in most common solvents—although some dissolution has been obtained [70]—, and by the difficulty of dispersing the CNTs homogeneously throughout the matrix and achieving good interfacial bonding for load transfer across the CNT-matrix interface. When CNTs aggregate, their behaviour is different to that of an individual nanotube. To solve

this problem, the aggregates need to be broken up and dispersed or cross-linked to prevent slippage. Wrapping with polymers has also provided a supramolecular approach to solubilisation of CNTs [71]. Considerable effort has therefore been devoted to the chemical modification of CNTs [72, 51], which might pave the way to many useful applications, in particular for composite preparations.

A wide range of polymer matrices have been employed, and there is growing interest in nanotube/ceramic and nanotube/metal composites. The advantage of CNTs in polymer-CNT composites is their low density and their electronic properties, which makes them ideal candidates for conductive or semiconducting polymer composites. In addition they represent a very popular system for studying fundamental physical phenomena on the mesoscopic scale. Following advances in manufacturing and processing it is likely that they will be integrated in many devices in our everyday life.

## Chapter 3

# Synthesis of Carbon Nanotubes

The discovery of multiwall carbon nanotubes in 1991 [18] has directed the attention to the synthesis of CNTs. Here we will review five different methods, from which three forms the mainstream of the CNT production. In the second part of this chapter we will discuss the current understanding of the growth mechanism of CNTs.

### 3.1 Synthesis methods

There are several distinct classes of production methods, but in the literature three main techniques exist. The arc-discharge [73] and laser ablation [58] methods are based on the cooling of carbon plasma generated by the evaporation of solid carbon sources. The third widely used technique is CCVD [74], where the vapour-phase carbon source is decomposed chemically. Flame synthesis [75] and the solar energy route [76] are also alternatives for CNT production, however, scale-up and low-cost difficulties have pushed them into the background.

#### 3.1.1 Arc-discharge

Initially the arc-discharge (AD) method was used for producing fullerenes [77] and it was the first technique to manufacture CNTs. It is based on the cooling of carbon plasma evolved by an electric arc between two graphite rods. These graphite rods are placed in an inert atmosphere such as helium, argon, or in hydrogen, air or liquid nitrogen at a typical pressure from 50 to 900 mbar. CNTs are grown through use of an electric arc by applying a DC current density of  $\sim 150 \text{ A/cm}^2$  with a voltage set to  $\sim 20 \text{ V}$ . Initially the two rods are just touched in order to initiate the arc. Once

the arc is established, the rods are kept at about a millimetre apart. Because of this high current density, the temperature in the arc can reach  $3000^{\circ}\text{C}$ . As the positive electrode vaporises, its length decreases but the distance between the anode and the cathode is kept constant [48, 73]. Figure 3.1 shows a schematic view of an arc apparatus.

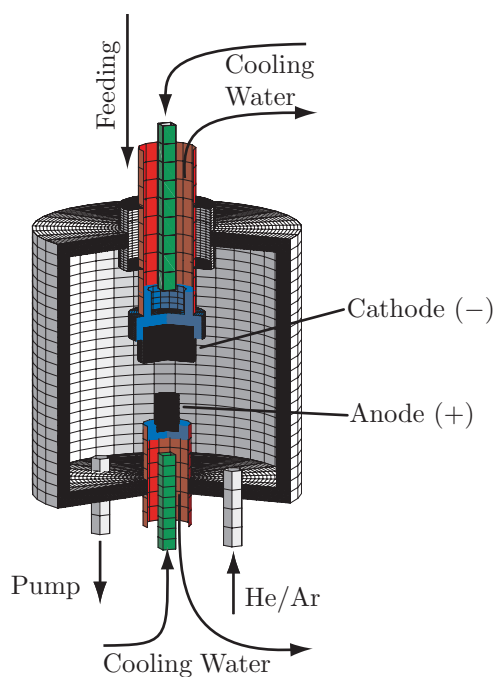


Figure 3.1: Schematic drawing of the arc-discharge method. In order to keep constant current between the cathode and the evaporating anode, the cathode is moved downwards during the reaction.

Approximately half of the evaporated carbon condenses on the frontal face of the cathode, forming a slag-like hard deposit. The remaining vapour condenses in a gas phase, forming soot, which finally piles up on the inner walls of the reaction chamber and around the root of the deposit.



Figure 3.2: (a) the arc-discharge product (b) hard shell (c) soft core.

The deposit consists of two regions: an inner fibrous black core and an outer gray, hard shell, see Figure 3.2. The inner core has a columnar structure that is made up of bundles of nanotubes and flocks of polyhedral carbon particles. Approximately 30% of the inner core consists of CNTs whereas, the hard shell is made up of polycrystalline graphite.

High quality MWNTs (Figure 3.3) can be grown using pure graphitic electrodes, while SWNT ropes can be produced when the consuming anode contains a small amount of transition metal catalyst particles such as cobalt, nickel or iron [78].

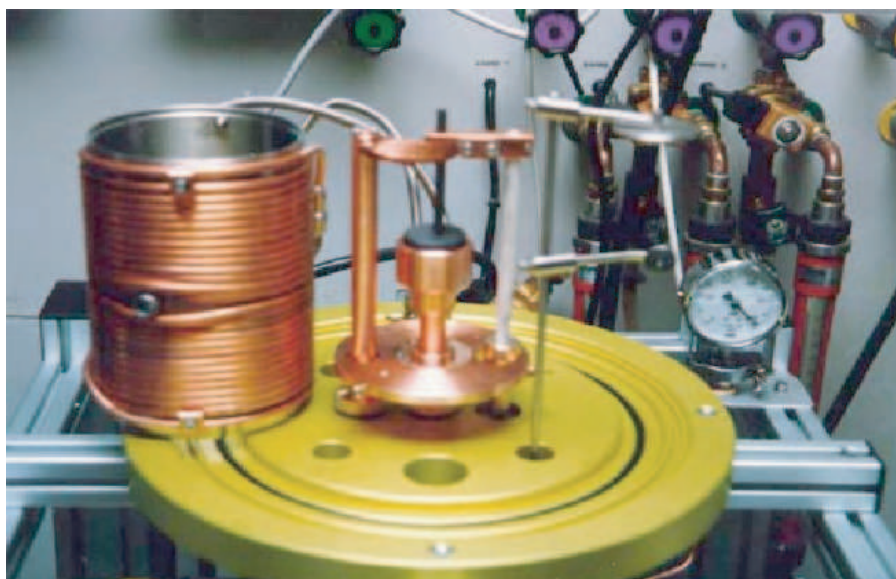


Figure 3.3: The arc-discharge apparatus in our laboratory. Graphite electrodes are in the middle opposing to each other. The water cooled soot collector is on the left hand side.

However this technique results in a mixture of components such as CNTs, multi-layered graphitic particles, fullerenes, carbon soot and in some cases catalyst particles. Because of the high percentage of impurities in the crude product, this method always requires purification of the nanotubes. The separation of CNTs from the contaminations can be a very long and difficult procedure depending on the desired purity and on the applied treatment.

### 3.1.2 Laser ablation

Another way of producing high quality CNTs is laser ablation [58]. In this method, intense laser pulses are used to ablate a carbon target. For SWNT growth the graphite containing 0.5% of nickel and cobalt. The target is placed in a furnace

heated to 1200°C. During laser ablation, an inert gas (He or Ar) is passed through the chamber, carrying the nanotubes to be collected on a cold collector (Figure 3.4).

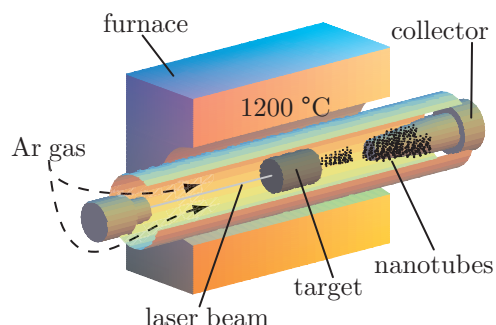


Figure 3.4: Synthesis of carbon nanotube ropes by laser ablation of a graphitic target. SWNT bundles are collected on the cooled collector [58].

In general, the laser is used to vaporise the graphite target in the oven. As the vaporised spoils cool, the carbon atoms quickly condense into large clusters. The inert gas drives the nanotubes to a cooled collector. The growing procedure of one nanotube continues until the catalyst particles become too large<sup>1</sup> or surrounding conditions have cooled so that carbon can no longer diffuse through the surface of the catalyst particles [79]. Another possible reason for the interruption of the reaction is when the catalyst particles become coated with a thick layer of carbon, so they cannot adsorb more.

Laser Ablation is similar to AD in regard to the applied high temperature in order to bring the solid carbon source to a vapour phase. It is generally considered that these methods produce CNTs of high quality, albeit in very small quantities. SWNTs formed in this case are bundled together by van der Waals forces [80].

### 3.1.3 Catalytic chemical vapour deposition

For the past 25 years, in chemistry, the Catalytic Chemical Vapour Deposition (CCVD) synthesis has been a well-known technique for synthesising carbon fibers. For CNT growth, it involves flowing a hydrocarbon gas through a tube over a catalyst material in a resistivity heated furnace, see Figure 3.5 [74, 81]. The key parameters controlling growth are: the carbon source, gas flow rate and ratio, catalyst, support and growth temperature [82, 83, 84]. A commonly used gaseous carbon source is a type of hydrocarbon, ( $C_nH_m$ ), such as acetylene ( $C_2H_2$ ) or methane ( $CH_4$ ) [85]. For catalyst, typically, Fe, Co, Ni or their alloys are dispersed on a

<sup>1</sup>During CNT growth, large clusters of catalyst particles can form due to the evaporation of the graphite target.

support material e.g. silicon, alumina or zeolite. Typical reaction temperatures are between 600°C and 1200°C.

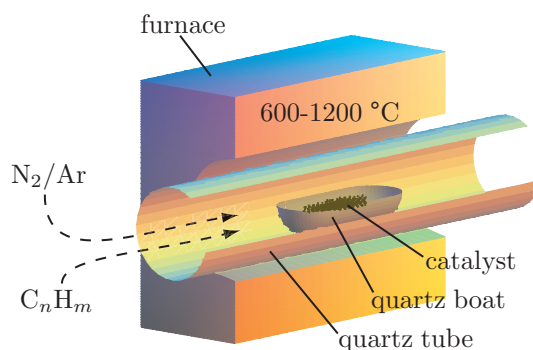


Figure 3.5: CCVD furnace. The catalyst particles are introduced in a quartz boat into the hot (700°C) furnace. Nanotubes grow over the catalyst via decomposition of acetylene.

This method is essentially a two-step process consisting of:

1. a catalyst preparation step and
2. the carbon-catalyst reaction i.e. the real synthesis of CNTs.

During the chemical reaction, the chemical bonds in the carbon source are cracked catalytically by high temperature and activated by catalyst resulting reactive carbon atoms in the atmosphere. The carbon then diffuses into the catalyst, where it will aggregate and carbon layers will be precipitated. Maintaining the proper conditions of the furnace (temperature, gas flow) CNTs will be grown over the catalyst particles.

It has many advantages including low temperature production, controllable growth and the “easy way” to scale up to industrial production. Precise setting of the catalyst preparation and the growth conditions, control over the diameter both on either single- and multiwall CNTs can be achieved. Furthermore, CNT alignment on a patterned surface [86], spiral [26] or Y-junctioned [87] nanotubes can also be produced by CCVD (see Figure 2.6). The only disadvantage is the weaker mechanical properties compare with the nanotubes made by AD or laser ablation.

Nevertheless, CCVD is more flexible than the other techniques and it has many variations such as Plasma-Enhanced Chemical Vapour Deposition (PECVD), which, typically, is coupled with a plasma generator at the reaction zone. Due to the electric field, it is possible to grow vertically aligned CNTs on different metal underlayers [88]. Moreover, much lower growth temperatures can be achieved than in the

“conventional” CCVD furnace, to such an extent that CNTs were grown on plastic surfaces [89].

Moreover, the CCVD technique is used for the growth study performed in this work and will be discussed in detail in Chapter 5 together with other experimental results.

### 3.1.4 Other synthesis methods

#### Flame synthesis

Among the variety of techniques which have been developed for nanotube synthesis, flame synthesis [75] is a continuous-flow scalable method with potential for considerably low cost CNT production. The procedure is based on burning a premixed carbon containing fuel, a rare gas and a source of metallic catalyst in a moderate vacuum, see Figure 3.6.

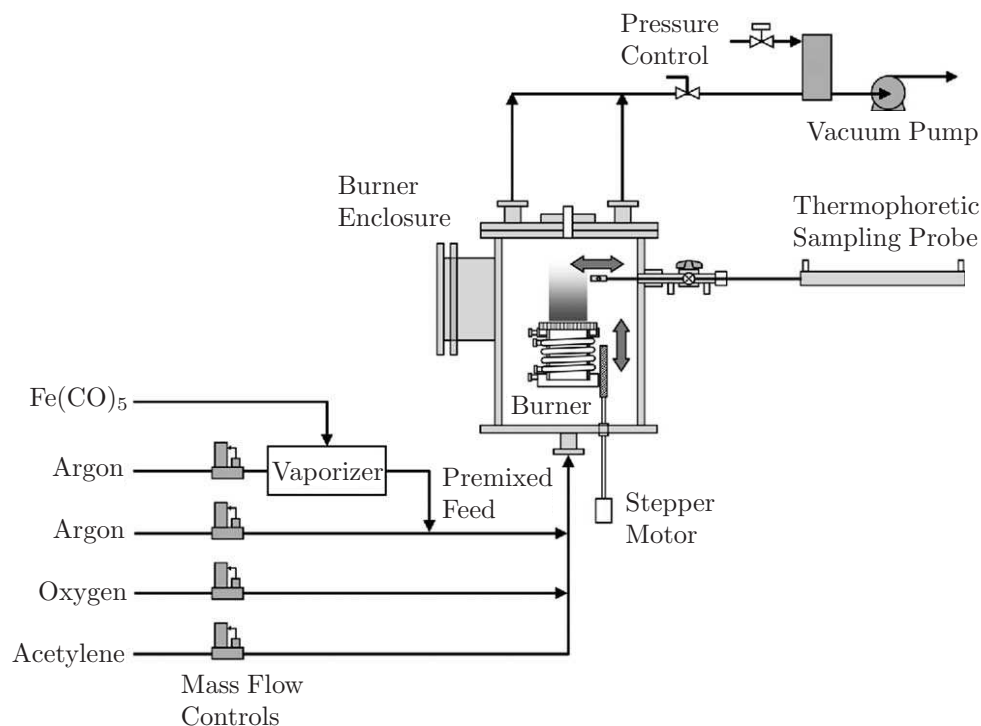


Figure 3.6: Schematic of the applied flame synthesis method in the experiment of Height et al. [90]. The premixed catalyst and the carbon source are burnt in a closed chamber under moderate vacuum. Vertical translation of the burner stage allows sampling at a series of heights above the burner. The product is collected in the upper part of the chamber

Typically, acetylene or methane is mixed with oxygen as fuel and is diluted with



argon gas. Iron-nitrate, ferrocene, nickelocene and iron-pentacarbonyl is commonly used for catalyst precursor. During the synthesis the fuel and the catalyst gases are burnt in the chamber at burner pressure of 6.7 kPa. The inception of nanotube growth appears to occur early in the post-flame region. However, once initiated, nanotube growth occurs rapidly. The product is collected from the upper flange of the burner chamber.

Generally, the yield per mass of carbon fed and presented metal particles is low. Height and coworkers [90] made a detailed study of the conditions for nanotube formation in a premixed flame (Figure 3.6). The interpretation of CNT formation identifies the role of iron oxide particles and suggests ways for improving the yield of nanotubes from the flame.

### The solar energy route

In order to evaporate a graphite target in an inert atmosphere, a high temperature can be obtained also by solar radiation [76]. In the experiment of Laplaze and coworkers, a 2 kW vertical solar furnace was employed. The setup consists of a stand part rounded by a Pyrex balloon flask, a graphite pipe, a target and a cellulose filter. The stand is a water-cooled brass cylinder which supports the cellulose filter to collect the soot. The target is a mixture of powdered graphite and cobalt-nickel catalyst and is placed into the focal point of the chamber by the graphite pipe. The pipe is heated at its top by sunlight and has triple functions: (i) channels the carbon soot, (ii) works as a thermal screen (iii) forms an annealing zone. The major difficulty in the solar furnace is to achieve a temperature high enough for the target to be vaporised. With clear-sky conditions, the estimated temperature of the crucible usually reached 2680°C.

## 3.2 Theory of catalytic growth of CNTs

In this section a general growth mechanism of CNTs is explained which can be employed for all catalytic processes without taking into account the applied method. In the CCVD processes catalysts are always required, but in the case of AD and laser ablation, only for SWNT production. MWNTs can be grown without catalyst from two pure graphite electrodes or graphite targets.

The catalyst metals (Fe, Co, Ni) are prepared either on a graphite target (AD, laser ablation) or another support such as silicon, alumina or zeolite (CCVD). From the carbon adsorbing-emitting point of view, the catalyst particles are not symmetric. One part of the catalyst can adsorb carbon atoms faster than the other. When

a catalyst is placed into a vapour-phase carbon enriched, high temperature environment<sup>2</sup>, the carbon starts to diffuse into the metal and is dissolved in its surface. For an unsaturated catalyst particle the absorption is highly exothermic. When the particle is saturated with carbon, another, endothermic process becomes beneficial and the carbon atoms will be segregated. In order to form an energetically favourable atomic configuration (i.e. avoid dangling bonds on the surface of the carbon), the carbon atoms assemble in an  $sp^2$  structure at a less reactive facet of the particle. The size of catalyst particles is a crucial parameter since it determines the CNT diameter. Below 100 nm of catalyst in diameter, it leads to tubular formation of carbon.

A simple model, presented in Figure 3.7 describes the growth with a particle at the top or bottom of the nanotube. In principle, both cases are the same, but in the case of bottom growth (Figure 3.7.b), the particle sticks more to the substrate surface than in the top growth case. If the adhesion force is not high enough to stick the nanotubes to the surface, the particles can be either lifted up or sucked into the tube, as is frequently found in TEM images of CCVD grown nanotubes [91].

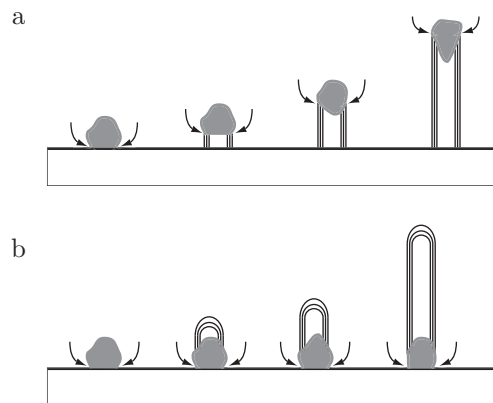


Figure 3.7: CCVD growth model of the nanotubes. (a) the tip and (b) the bottom growth of CNTs. Depending on the adhesion force between the particle and the substrate, the catalyst can be pushed up by the growing nanotube (a) (tip growth) or the carbon diffusion continues from the bottom (b) (bottom growth).

According to the model given by Kanzov et al. [92], the range of catalyst particle diameters is restricted to where effective growth is possible. For large particles the reaction is too slow due to the long diffusion lengths, i. e. the smaller the particles are, the faster the growth rate should be. However, very small metal particles are

<sup>2</sup>High temperature means above the activation threshold temperature.

also not useful, because very small diameters are energetically unfavourable due to the high curvature. This implies that there is a range of particle diameters for the formation of nanotubes.

Recent molecular dynamic simulations showed that defective SWNTs were able to be grown from iron-carbide particles at temperatures between  $530^{\circ}\text{C}$  and  $1130^{\circ}\text{C}$  [93]. As can be seen in Figure 3.8 which shows iron-carbide particles as a function of temperature, below  $330^{\circ}\text{C}$  and above  $1330^{\circ}\text{C}$  graphene sheets encapsulate the particle or form a three-dimensional soot-like structure and affects the growth.

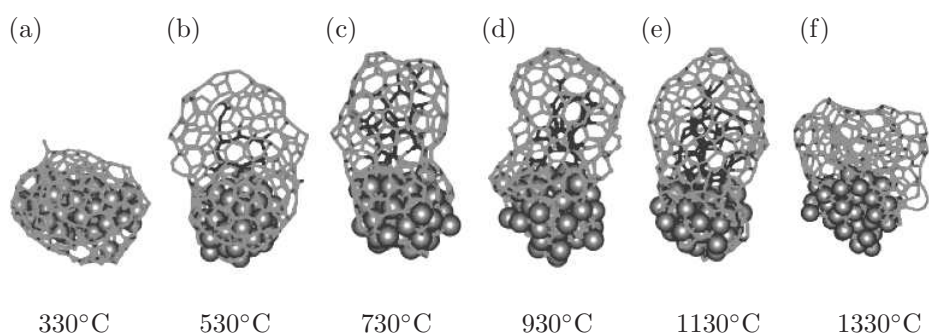


Figure 3.8: An encapsulated catalyst particle, SWNTs and soot structures obtained between  $530^{\circ}\text{C}$  and  $1130^{\circ}\text{C}$ . Iron atoms are represented as balls and carbon atoms as a stick-like structure [93].

The effect of catalyst particle size on the growth mechanism and structure of SWNTs has also been studied by Ding et al. [94].

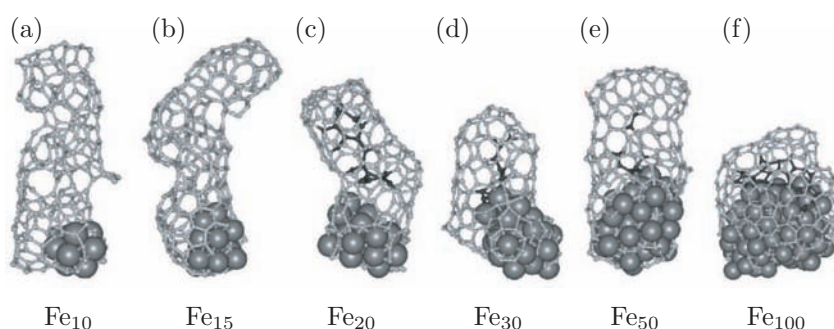


Figure 3.9: The size effect of the catalyst particle. Simulation of growth of SWNTs from cluster of 10 to 100 Fe atoms [93].

The simulated temperature range for nanotube nucleation was similar to that used in CCVD experiments. Their results show that nucleation begins when carbon atoms precipitate to the surface of a highly supersaturated iron-carbide particle, Figure 3.9. These atoms nucleate carbon strings and polygons that grow into larger

graphitic islands, which lift off the surface to form graphitic caps. For large particles, containing at least 20 Fe atoms (0.6 nm), the caps grow in diameter until they have the same diameter as the cluster. In this way well-structured SWNTs that have diameters similar to the metal cluster diameters are grown. Additionally, SWNTs grown from smaller Fe clusters containing 10-15 atoms, have larger diameter than the cluster diameter and their walls have very poor graphitisation that contain many defects and bond-unsaturated carbon atoms.

In agreement with this result, experimental results show that SWNTs with 0.6-0.7 nm can grow from Co clusters containing as low as 20-30 atoms [95].

## Chapter 4

# Characterisation Techniques

In order to get topographical, chemical and in some case crystallographical information about the samples, three main characterisation techniques have been applied in the thesis: Transmission and Scanning Electron Microscopy (TEM, SEM), X-Ray Powder Diffraction (XRPD) and Thermogravimetry Analysis (TGA).

### 4.1 Electron microscopy

Electron Microscopes (EMs) function exactly as their optical counterparts except that they use a beam of electrons instead of light to “image” the specimen and gain information as to its structure and composition <sup>1</sup>. Thanks to the dual wave-charged particle nature of electrons, EMs not only provide images but can also yield a wealth of secondary signals like X-rays, Auger electrons and light [96]. This examination can provide topography, morphology, chemical composition and crystallographic information.

In this work, TEM and SEM, in particular, were used to differentiate resulting materials characteristics, such as average diameter, level of purity, wall structure, composition of nanotubes and catalyst particles.

#### 4.1.1 Scanning electron microscopy

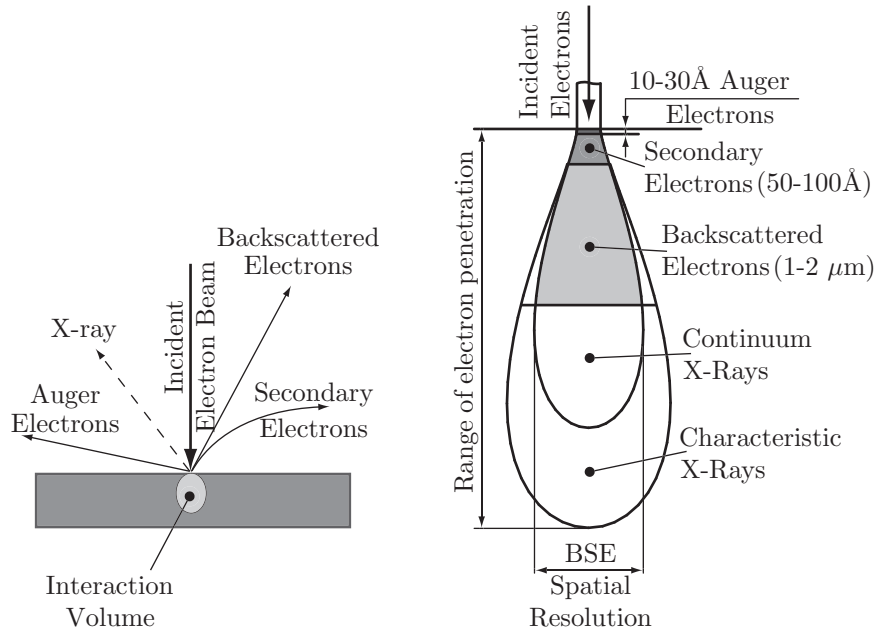
##### **Bulk specimen interactions**

The energetic electrons in the microscope strike the sample and various reactions can occur as shown in Figure 4.1a. The interactions sketched in the schematic drawing are utilised when examining thick or bulk specimens(SEM). A drawing

---

<sup>1</sup><http://cimewww.epfl.ch>

showing the generation depths of the interactions is also presented in Figure 4.1b. In the SEM the following electrons are used for sample characterisation:



(a) The types of the interactions between a bulk specimen and the incident e-beam in a SEM.

(b) The interaction volume of the different electrons.

Figure 4.1: Interactions between the specimen and the electrons as well as penetration depths of different generated electrons in a bulk sample inside a SEM.

**Secondary Electrons** Caused by an incident electron passing “near” an atom in the specimen, near enough to impart some of its energy to a lower energy electron. This causes a slight energy loss and path change in the incident electron and the ionisation of the electron in the specimen atom. This ionised electron, a so called “secondary electron”, then leaves the atom with a very small kinetic energy.

Production of secondary electrons is very topography related. Due to their low energy, 5eV, only secondaries that are very near the surface (<10nm, see 4.1) can exit the sample and be examined. Collection of these electrons is aided by using a “collector” in conjunction with the secondary electron detector.

**Backscattered Electrons** Caused by an incident electron colliding with an atom in the specimen which is nearly normal to the incident’s path. The incident electron is then scattered “backward” ( $180^\circ$ ).

The production of backscattered electrons varies directly with the specimen’s

atomic number. This differing generation rate causes higher atomic number elements to appear brighter than lower atomic number elements. This interaction is utilised to differentiate parts of the specimen that have different average atomic number.

Auger electrons and X-rays were not or rarely used in the characterisation of CNTs.

### Image formation inside a SEM

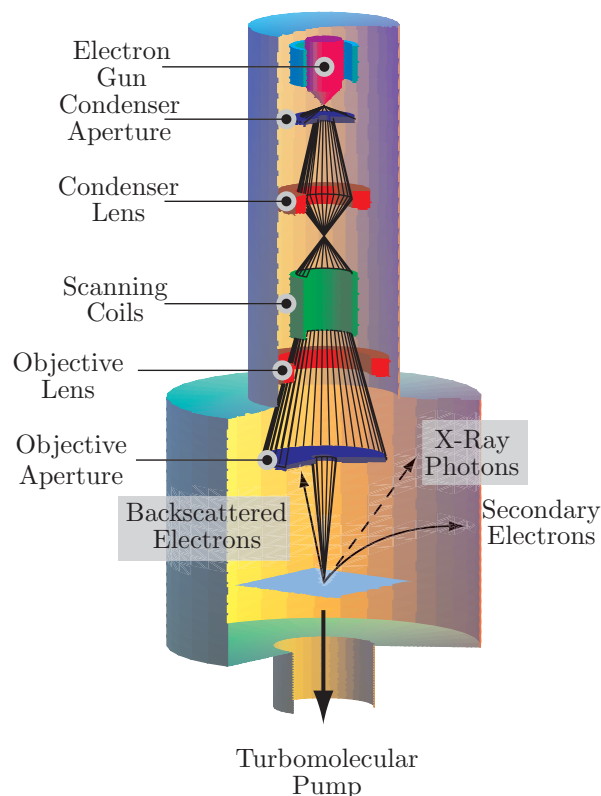


Figure 4.2: A schematic drawing of a SEM microscope including the interactions between a bulk specimen and the incident e-beam.

- At the top of the picture is an electron gun, producing a stream of monochromatic electrons.
- The electron beam is condensed by the first condenser lens, which is used to form the beam. Together with the condenser aperture it eliminates the high-angle electrons from the beam.
- The second condenser lens forms the electrons into a thin, tight, coherent beam and is usually controlled by the “fine probe current”.

- A user selectable objective aperture further eliminates high-angle electrons from the beam.
- A set of coils then “scan” or “sweep” the beam in a grid fashion like a television, dwelling on points for a period of time (usually in the microsecond range) determined by the scan speed.
- The final lens, the objective lens, focuses the scanning beam onto the desired part of the specimen.
- When the beam strikes the sample interactions occur inside the sample and are detected with various instruments.
- Before the beam moves to its next dwell point these detectors count the number of interactions and display a pixel on a screen whose intensity is determined by this number. Generally, the more reactions the brighter the pixel.
- This process is repeated until the grid scan is finished and then repeated.

### 4.1.2 Transmission electron microscopy

#### Thin specimen interactions

In a TEM, only thin specimens can be observed because electrons have a very short mean free path and can only be transmitted in a very thin sample. Thus, interactions between the specimen and the beam are different to those in a SEM. The interactions schematised in Figure 4.3 are those which take place in a TEM.

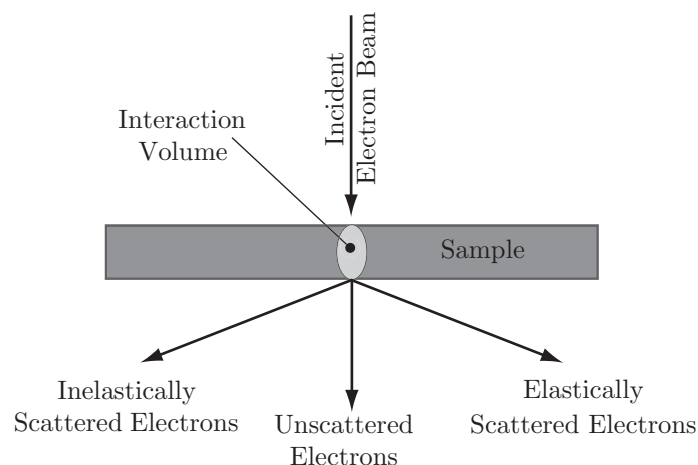


Figure 4.3: A schematic drawing of the interactions between an electron transparent specimen and the incident e-beam in a TEM.



**Unscattered Electrons** Incident electrons are transmitted through the thin specimen without any interaction occurring inside the specimen.

The transmission of unscattered electrons is inversely proportional to the specimen thickness. Areas of the specimen that are thicker will have less transmitted unscattered electrons and so will appear darker, conversely the thinner areas will have more transmitted and thus will appear brighter. The, so-called “bright-field” TEM images are composed of direct, unscattered electrons.

**Inelastically Scattered Electrons** Incident electrons that interact with specimen atoms in an inelastic fashion, losing energy during the interaction.

One use of the inelastically scattered electrons is for Electron Energy Loss Spectroscopy (EELS): The inelastic loss of energy by the incident electrons is characteristic of the elements that were interacted with. These energies are unique to each bonding state of each element and thus can be used to extract both compositional and bonding (i.e. oxidation state) information on the specimen region being examined.

**X-rays** Caused by the de-energization of the specimen atom after a secondary electron is produced. Since a lower (usually K-shell) electron was emitted from the atom during the secondary electron process an inner (lower energy) shell now has a vacancy. A higher energy electron can “fall” into the lower energy shell, filling the vacancy. As the electron “falls” it emits energy, usually X-rays, to balance the total energy of the atom.

X-rays emitted from the atom will have a characteristic energy which is unique to the element from which it originated. These signals are collected and sorted according to energy.

### **Image formation inside a TEM**

The first TEM was developed by Max Knoll and Ernst Ruska in Germany in 1931. A TEM works much like a slide projector, which shines a beam of light through the slide. As the light passes through it is affected by the structures and objects on the slide. These effects result in only certain parts of the light beam being transmitted through certain parts of the slide. This transmitted beam is then projected onto the viewing screen, forming an enlarged image of the slide.

In the TEM, the sample is illuminated with an electron beam using condenser lenses. The resulting image, representing a 2D projection of the sample, is magnified by the projector lens before being collected on a fluorescent screen, photographic paper or a CCD camera. The main limiting factor in TEM resolution is not the

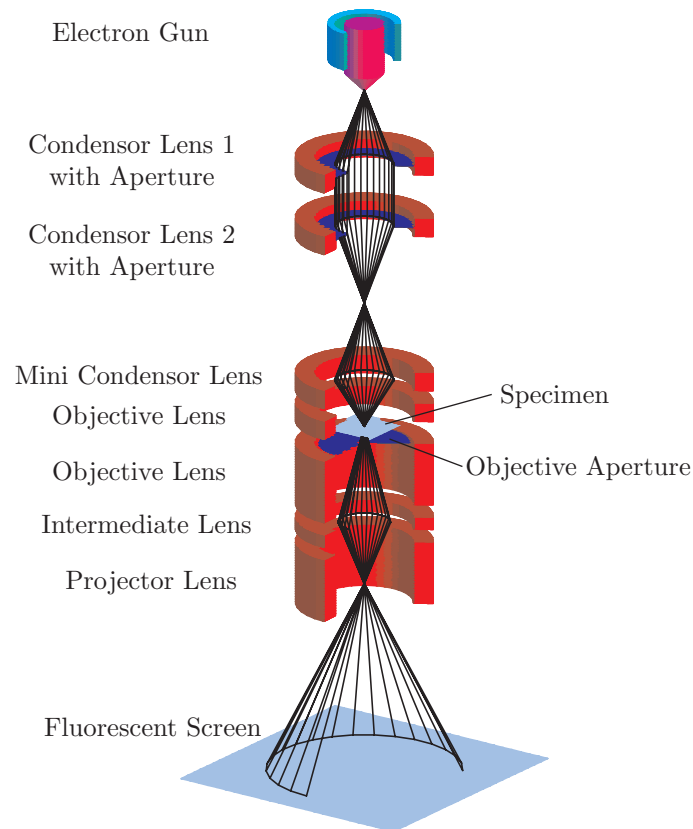


Figure 4.4: a) A simplified schematic drawing of the main components of a transmission electron microscope.

electron wavelength but the aberrations due to electromagnetic lenses that result in a  $1\text{\AA}$  resolution for state-of-the-art microscopes.

- The electron gun, produces a coherent monochromatic electron beam, as in the case of SEM.
- This beam is focused by the use of condenser lenses 1 and 2. The first lens largely determines the “spot size”; the general size range of the final spot that strikes the sample. The second lens changes the size of the spot on the sample; changing it from a wide dispersed spot to a pinpoint beam.
- The beam is restricted by the condenser aperture, to filter high angle electrons.
- The beam strikes the specimen and parts of it are transmitted.
- The objective lens is the most critical lens since it determines the resolving power of the instrument and performs the first stage of imaging. The objective aperture is positioned in the back focal plane of the objective lens, where electron diffraction patterns are formed, and limits the electron beams con-

tributing to the final image. The selected area electron diffraction aperture can select the area of interest in order to obtain the diffraction pattern of that region.

- The image is passed down the column through the intermediate and projector lenses, being enlarged all the way.
- The image strikes the phosphor image screen and light is generated, allowing the user to see the image. The darker areas of the image represent those areas of the sample through which fewer electrons were transmitted (thicker or denser part of the sample).

Today, TEMs constitute a very efficient tool for material characterisation by numerous methods like direct observation, energy dispersive X-ray spectroscopy (EDX), electron energy loss spectroscopy (EELS).

Diamond, graphite and fullerene consist only of carbon so that all of these specimens have absorption edges around 284 eV in EELS corresponding to the existence of carbon atoms, see Figure 4.5. From the fine structure of the absorption edge, the difference in bonding state can be detected. The sharp peak at the absorption edge corresponds to the excitation of carbon K-shell electrons (1s electron) to empty anti-bonding  $\pi$ -orbital. It is not observed for diamond, because of the lack of  $\pi$ -electrons<sup>2</sup>.

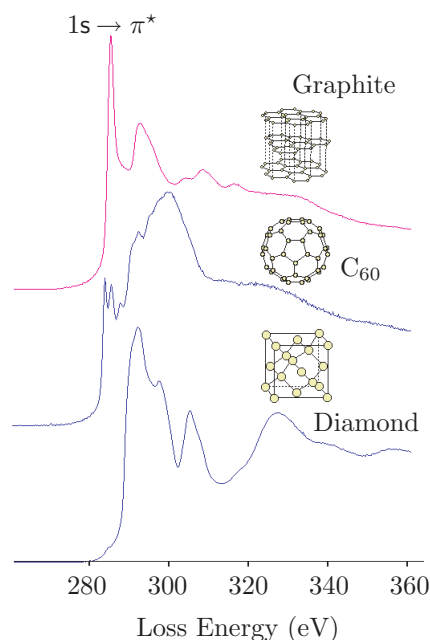


Figure 4.5: EELS spectrum of graphite, fullerene and diamond.

<sup>2</sup><http://cimewww.epfl.ch>

TEM was the technique used to discover CNTs in 1991 in the carbon soot produced during electric arc discharge between two electrodes [18] (Figure 2.5 on page 9). The detailed microstructure of CNTs has also been first studied by EM diffraction in 1999 [22], see Figure 4.6.

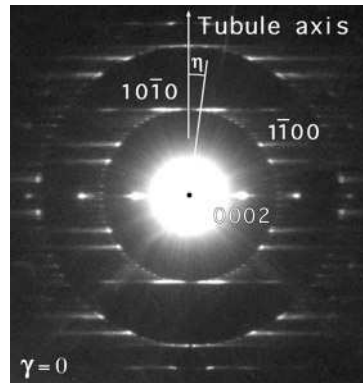


Figure 4.6: Electron diffraction pattern of a multi-walled carbon nanotube. The pattern is the superposition of the diffraction patterns produced by several isochiral clusters of tubes with different chiral angles. The direction of the beam incidence is approximately normal to the tube axis and the pattern exhibits 2mm planar symmetry [22].

#### CNT sample preparation for EM

In general sample preparation is a very demanding and time consuming task in electron microscopy. Fortunately, CNTs are in the form of powder so the sample preparation in most cases involves a careful clean work. Both the SEM and TEM preparations involve dispersing of the synthesised powder in pure isopropyl or ethyl alcohol by sonication.

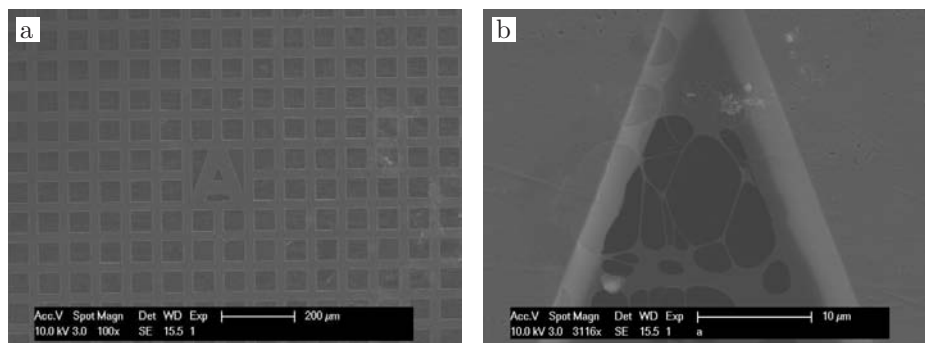


Figure 4.7: (a) A prepared TEM grid. Suspension of CNTs were dropped to the holey carbon-coated surface. (b) A magnified part of the grid shows nodes of CNTs.

In the case of SEM observations the suspension was dropped onto a well polished alumina specimen holder. For TEM, a drop of suspension was put on a copper grid covered with holey carbon film. Figure 4.7 shows a prepared TEM grid photographed by SEM.

At the EPFL, we have the opportunity of using different EMs. Both SEM and TEM studies were performed at the central facility and research center in electron microscopy (CIME) of EPFL. SEM micrographs were taken using a Philips XL30 FEG and XL30 SFEG microscopes in conventional and high resolution mode, respectively. For the TEM study the Philips CM20 microscope was mainly employed for conventional and high-resolution mode operating at 200 kV. EELS measurement was carried out using the Philips CM300 FEG microscope equipped with a Gatan Image Filter 2000 operating at 200 kV.

## 4.2 XRPD

X-ray Powder Diffraction is the most commonly used tool to determine the composition of powders. Each crystalline solid has its unique characteristic XRPD pattern which may be used as a “fingerprint” for its identification.

Phase identification is accomplished by comparing the data (peaks and relative intensities) from the specimen with peaks and relative intensities from a very large set of “standard” data provided by the International Center for Diffraction Data (ICDD). Interaction of X-rays with sample creates secondary diffracted beams of X-rays related to interplanar spacings in the crystalline powder according to the Bragg law:  $n\lambda = 2d \sin \vartheta$ , where the integer  $n$  is the order of the diffracted beam,  $\lambda$ ,  $\vartheta$  are the wavelength and the angle of the incident X-ray beam and  $d$  is the distance between adjacent planes of atoms (d-spacings).

For the measurements a Rigaku diffractometer was used in Bragg-Brentano geometry with monochromatic Cu-K $\alpha$  radiation. The data were collected in the  $\vartheta - 2\vartheta$  mode, i.e. X-ray tube is fixed, and the specimen moves at  $\frac{1}{2}$  the rate of the detector.

## 4.3 TGA

Thermogravimetry is a technique for the measurement of weight loss as a function of temperature. Within a short time and using small samples, information is obtained concerning the composition as well as its stability, oxidation behavior or the kinetics of a chemical reaction.



## Chapter 5

# CCVD Growth of Carbon Nanotubes by Using Alkaline Earth Carbonates

As presented in the Chapter 3, the Catalytic Chemical Vapour Deposition (CCVD) technique is the most common method for the synthesis of carbon nanotubes (CNTs) at large scale and low cost. Since this method consists of the decomposition of a hydrocarbon over a supported catalyst, many parameters have to be optimised (i.e. support, catalyst composition, growth temperature, retention time in the reaction chamber, etc.) in order to increase the production rate.

Previous experiments from our group [97] pointed out that the use of calcium carbonate as a support instead of  $\text{SiO}_2$  or zeolites facilitates the purification step, since  $\text{CaCO}_3$ , as well as other alkaline earth carbonates, is completely dissolved in diluted acid. Without optimising each growth parameter, the production rate reached 100 g/day of purified MWNTs using a rotary tube furnace.

Recently, influence of the support has been reported [98] but the role of the catalyst elements is not well understood yet. Furthermore, experiments on the growth of CNTs by adding  $\text{H}_2\text{O}$  [99] presented an enhancement on the conversion of the hydrocarbon into carbon nanotubes. Moreover, some carbon nanotubes have been produced from alcohol (R-OH) with a high conversion rate as well [100]. This could indicate that the addition of an oxygen containing species is helpful for the growth of carbon nanotubes. Nevertheless, the role of these oxygenated species has not been yet clearly identified.

Within this chapter, we present a systematic study for the optimisation of several

growth parameters (furnace temperature and retention time). We identify the effect of the metal composition in the catalyst as well as report the influence of the alkaline earth carbonate support on the product quantity and present a possible involvement mechanism of the carbonate in the growth process. Finally, this optimisation allows us to drastically increase the production rate up to about kg/day of purified CNTs using the rotary tube furnace technique.

## 5.1 Furnace

Two different furnaces were used for growing nanotubes by CCVD. For parametric study and qualitative experiments the so-called *fixed-bed* furnace was operated. For large-scale production and for fine tuning the *rotary tube* furnace was used.

### 5.1.1 Fixed-bed furnace

The pre-parametric studies were elaborated in a fixed-bed furnace. Figure 3.5 on page 23 shows a general schematic drawing of the CCVD furnace. This has the identical schema to our resistivity heated coil furnace. It contains a quartz tube, where a small quartz boat is introduced together with the catalyst. The gases traverse the tube and the off-gas mixture is fluxed below the furnace through oxytol in order to dissolve the residual organic materials. The reaction occurs in the hot part over the catalyst in the middle of the furnace.

### 5.1.2 Rotary tube furnace

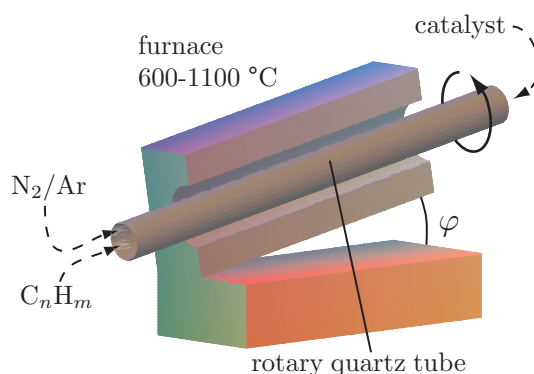


Figure 5.1: Rotary tube furnace.

For the final settings of large-scale production the rotary tube furnace was used. This CCVD furnace differs from the fixed-bed furnace only in a rotating quartz



tube and an automatic catalyst feeder, which enables us to scale up the production rate, see Figure 5.1. The oven works typically at temperatures between 600°C and 1100°C.

The acetylene and the carrier nitrogen gas was passed through the tube together with the powder. The reaction speed and time was set by the rotary speed and the angle. As the powder travelled through the hot part of the furnace nanotubes were grown. The product was collected at the lower end of the tube.

## 5.2 Catalyst

### 5.2.1 Catalyst preparation

MWNTs were synthesised by decomposition of acetylene over  $\text{Fe}_{1-\xi}\text{Co}_\xi$  ( $0 \leq \xi \leq 1$ ) catalysts supported by alkaline earth carbonates<sup>1</sup>. The total concentration of metal is about 5wt% relative to carbonate [69, 97]. A typical catalyst preparation:

- stoichiometric amount of metal salt – cobalt(II) and/or iron(III)<sup>2</sup> – is dissolved in distilled water and neutralised with ammonia (necessary to avoid the release of  $\text{CO}_2$  occurring when carbonates contact acids).
- $\text{MCO}_3$  is subsequently dispersed into the solution.
- The resulting mixture is dried on a hot plate under continuous stirring at 120°C.

This brownish powder is referred to “as-prepared catalyst” since it consists of a mixture of salts and carbonate, whereas “supported catalyst” is related to  $\text{Fe}_{1-\xi}\text{Co}_\xi/(\text{MCO}_3)$  obtained after heat treatment of the as-prepared catalyst in  $\text{N}_2$ , see in Figure 5.2.

Large batches of as-prepared catalyst were produced and kept in boxes in a ventilated cupboard without special care. For the production, the as-prepared catalyst is placed in an oven, flushed with nitrogen ( $\text{N}_2$ ), and finally exposed to a mixture of acetylene and nitrogen for 30 minutes, fluxed at 1 and 70 L/h, respectively.

---

<sup>1</sup>Alkaline earth carbonate:  $\text{MCO}_3$  where M= Mg, Ca, Sr or Ba

<sup>2</sup>cobalt(II): cobalt acetate tetrahydrate ( $\text{Co}(\text{CH}_3\text{COO})_2 \cdot 4\text{H}_2\text{O}$ ) and iron(III): iron nitrate nonahydrate ( $\text{Fe}(\text{NO}_3)_3 \cdot 9\text{H}_2\text{O}$ ) corresponding to  $\text{Fe}_{1-\xi}\text{Co}_\xi$  composition, where  $0 \leq \xi \leq 1$ .

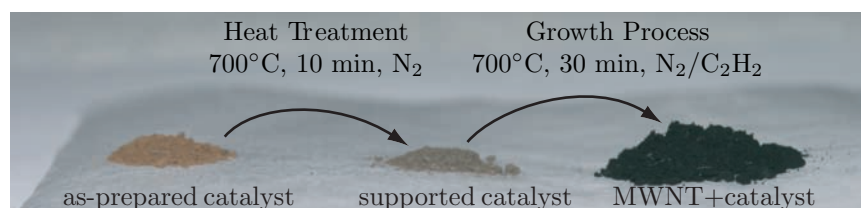


Figure 5.2: The as-prepared catalyst, supported catalyst and the MWNT powder. 10 minutes heat treatment under nitrogen atmosphere results in the supported catalyst. MWNTs grew over the supported catalyst after 30 minutes of acetylene exposure.

### 5.2.2 Catalyst composition

First we studied the influence of the catalyst composition  $\text{Fe}_{1-\xi}\text{Co}_\xi$  on the carbon yield. A series of reactions were taken with different catalyst composition for 30 min at  $700^\circ\text{C}$ ,  $720^\circ\text{C}$  and  $740^\circ\text{C}$  under  $\text{C}_2\text{H}_2/\text{N}_2$  gas flux. In Figure 5.3, the evolution of the purified product mass is plotted versus the  $\text{Co}(\xi)$  content in the  $\text{Fe}_{1-\xi}\text{Co}_\xi$  alloys.

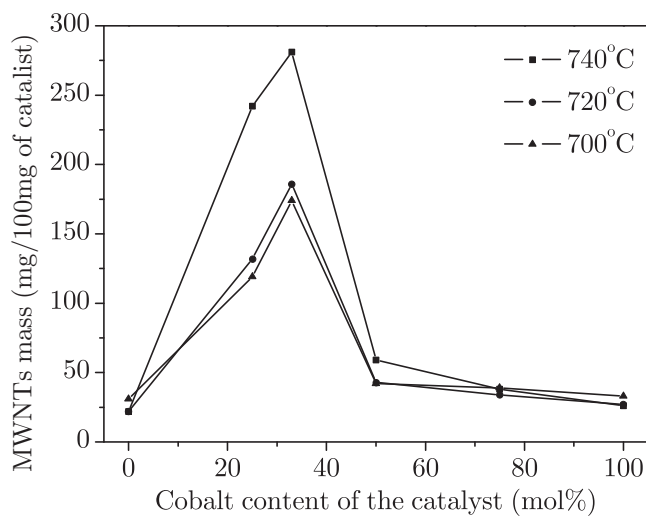


Figure 5.3: Evolution of the purified product mass versus the supported  $\text{Co}(\xi)$ -Fe content of the catalyst in the alloy of  $\text{Fe}_{1-\xi}\text{Co}_\xi/\text{CaCO}_3$ . Curves correspond to 30 minutes growth at  $700^\circ\text{C}$ ,  $720^\circ\text{C}$  and  $740^\circ\text{C}$ , respectively.

For all three temperatures a clear bell-shaped dependence of the resulting carbon yield is visible on the catalyst composition with the maximum at  $\xi = 33$  mol% of cobalt.

Our observation, that the resulting carbon content is higher for all binary alloys than for pure metals, is in agreement with the earlier observation that nanoparticles

of bimetallic alloys give higher yields of CNTs than monometallic catalysts [101, 102]. Preliminarily, the maximum yield of about 280 mg of purified MWNTs can be prepared from 100 mg of  $\xi = 33$  mol% as-prepared catalyst, at 700°C. E. Flahaut et al. [102] obtained comparable results for the yield of single walled CNT growth. Unfortunately, they conclude that the highest yield of carbon deposition is for  $\xi = 25$  mol% of Co without considering the case of  $\xi = 33$  mol%.

In order to understand why we have the highest CNT yield in the case of  $\text{Fe}_{0.66}\text{Co}_{0.33}$  catalyst, structures of the catalyst particles have been studied at different stages of nanotube growth, see Figure 5.4. To this end, we performed X-ray Powder Diffraction (XRPD) on the supported catalyst after annealing under ① pure  $\text{N}_2$  and ②  $\text{N}_2$  mixed with  $\text{C}_2\text{H}_2$ , to identify their crystalline structure and their composition.

The most predominant phases present correspond to  $\text{CaCO}_3$  and/or  $\text{CaO}$ ; the fraction of the latter depends on the annealing atmosphere. Additional peaks are attributed to the most intense reflections of  $\text{Fe}_2\text{CoO}_4$ ,  $\text{CoO}$  or  $\text{Fe}_2\text{Co}$  depending on the stoichiometry or on the annealing atmosphere. The presence of a mixed Ca-Fe-Co oxide phase could not be confirmed, which indicated the absence of the reaction between  $\text{CaCO}_3$  and Fe, Co precursor salts.

To clarify the composition of the second phase formed in the metallic system depending on the stoichiometry  $\text{Fe}_{1-\xi}\text{Co}_\xi$ , additional experiments have been performed with an unsupported catalyst. For the preparation of the unsupported catalyst, the metallic salt was mixed in distilled water, without carbonate, and the solution dried under continuous stirring to preserve the homogeneity of the solution in the resulting solid. A few milligrams of these mixtures were introduced into the fixed-bed furnace and annealed.

Figure 5.4 shows the corresponding XRPD patterns which are consistent with the XRPD patterns of the supported catalyst except that the intense  $\text{CaCO}_3$  and  $\text{CaO}$  peaks are missing and therefore easier to interpret.

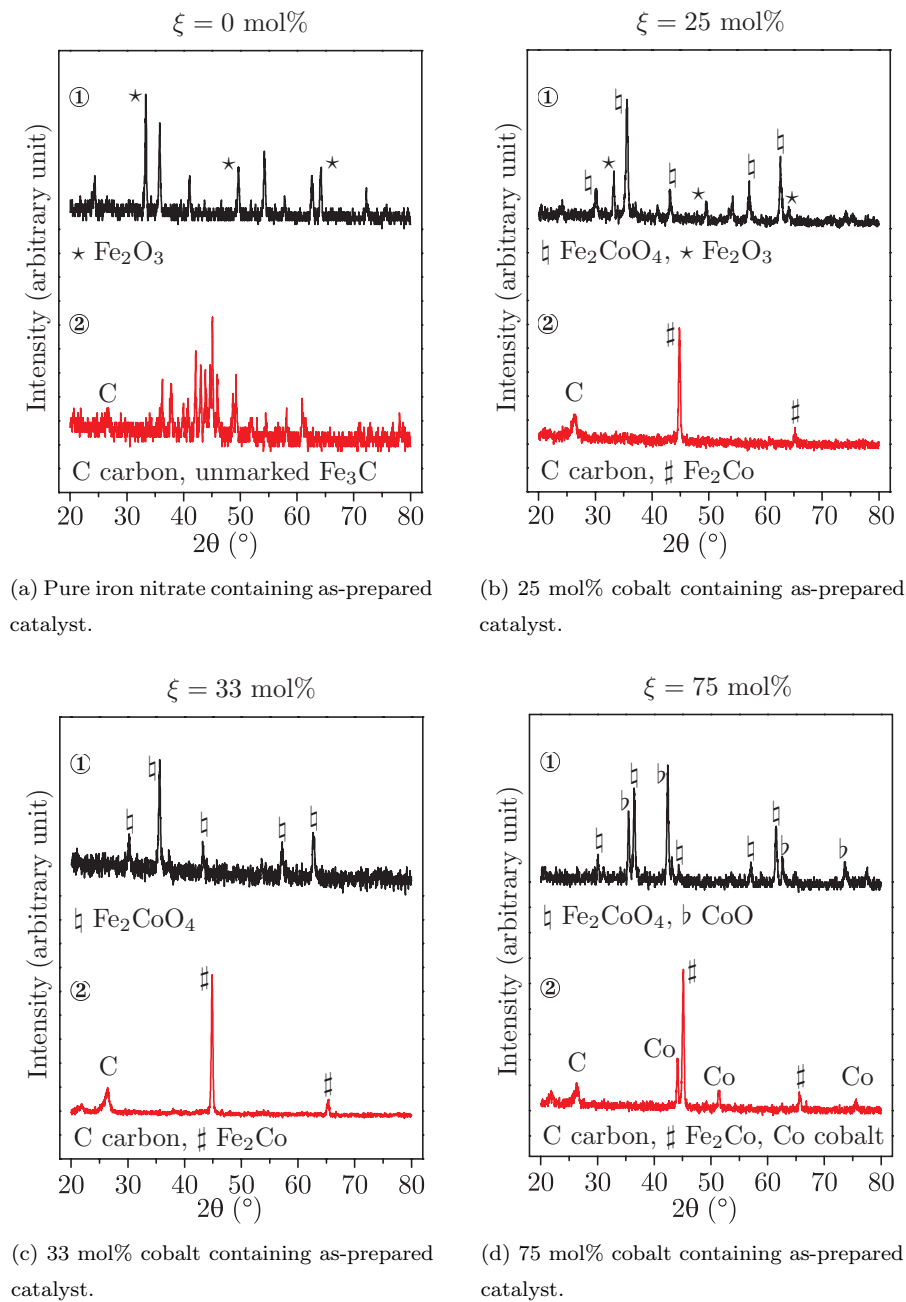


Figure 5.4: X-ray Powder Diffraction patterns. For each composition, two diagrams of the products are presented: ① annealed for 10 min under  $N_2$  and ② 10 min  $N_2$  exposure was followed by 10 min  $N_2/C_2H_2$ .

According to the XRPD results three composition ranges are distinguished.

### $\xi = 33 \text{ mol\% Co}$

After 10 min annealing under  $\text{N}_2$  atmosphere (①), a single phase catalyst is obtained during Co-Fe salt decomposition, which corresponds to the spinel<sup>3</sup> structure of  $\text{Fe}_2\text{CoO}_4$ . Additionally 10 min treatment under  $\text{C}_2\text{H}_2$  mixed with  $\text{N}_2$  (②), XRPD spectrum changes drastically (Figure 5.4 c), the oxide is reduced and we obtain pure  $\text{Fe}_2\text{Co}$  alloy as expected. If acetylene is further exposed to this reduced catalyst it will be decomposed into hydrogen and carbon, Figure 5.5.

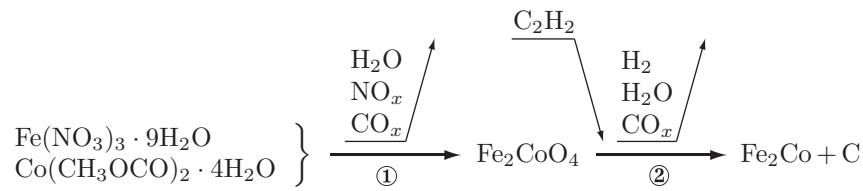


Figure 5.5: The flowchart of the heat treatment of the as-prepared catalyst in the case of 33 mol% of cobalt content.

### $\xi < 33 \text{ mol\% Co}$

Deviation from the previous composition leads to the presence of impurities. Salt decomposition under  $\text{N}_2$  (①) of the Fe enriched catalyst produces a  $\text{Fe}_2\text{CoO}_4$  and  $\text{Fe}_2\text{O}_3$  mixture. Reduction of the oxides by acetylene (②), produces  $\text{Fe}_2\text{Co}$  alloy and cementite ( $\text{Fe}_3\text{C}$ ) (Figure 5.6).

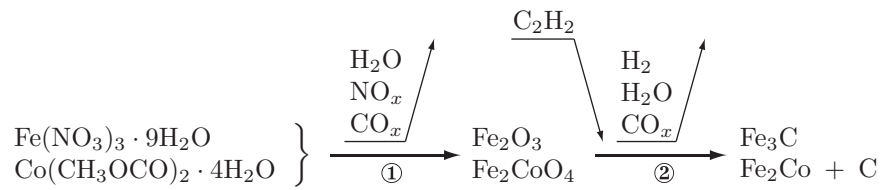


Figure 5.6: The flowchart of the heat treatment of the as-prepared  $\xi < 33 \text{ mol\%}$  catalyst.

### $\xi > 33 \text{ mol\% Co}$

For a Co rich compound CoO is predominantly formed mixed with  $\text{Fe}_2\text{CoO}_4$  under  $\text{N}_2$  (①), which reacts with acetylene (②) to produce pure Co metal (Figure 5.7).

<sup>3</sup>Spinel is a typical cubic structure of  $\text{X}_2\text{YO}_4$  compositions with lattice constant of  $\sim 8\text{\AA}$ , where X and Y chemical elements are distributed in tetra- and octahedral coordinations. In case of Fe and Co this is  $\text{Co}_{0.35}\text{Fe}_{0.65}[\text{Co}_{0.65}\text{Fe}_{1.35}]\text{O}_4$ , where the fraction of the tetrahedral sites occupied by Fe ions and the brackets indicating the ions in octahedral sites [103].

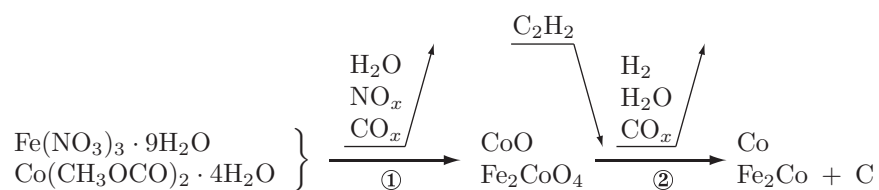


Figure 5.7: The flowchart of the heat treatment of the as-prepared  $\xi > 33$  mol% catalyst.

The fact that the highest yield is obtained with the metal mixture where only  $\text{Fe}_2\text{Co}$  is formed indicates that this alloy is the most active catalyst for CNT growth compared to  $\text{Fe}_3\text{C}$  or  $\text{Co}$ . SEM observations also confirmed the high purity level at  $\xi = 33$  mol% of catalyst (Figure 5.8).

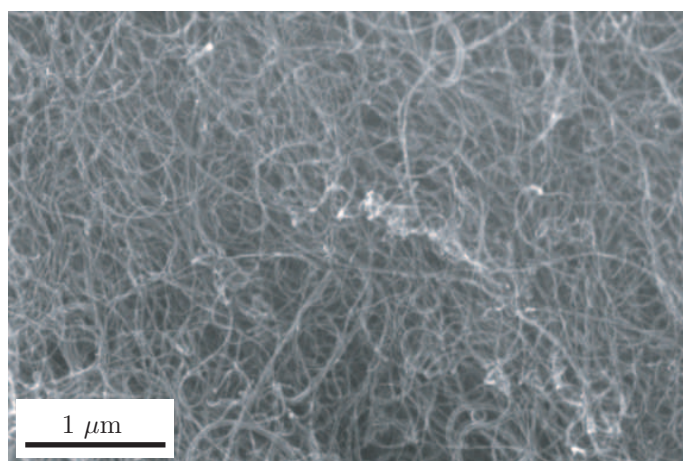


Figure 5.8: SEM micrograph of CCVD nanotubes grown at 33 mol% 660°C for 30 minutes.

TEM analysis of CNTs after the purification step has shown a direct correlation between the catalyst composition and the density of embedded particles. Figure 5.9c shows a TEM image of CNTs grown from  $x = 33$  mol%. Small embedded particles can only rarely be seen whereas for  $x < 33$  and  $x > 33$  mol% (Figure 5.9a,b d-f) the density of the partial filling significantly increases.

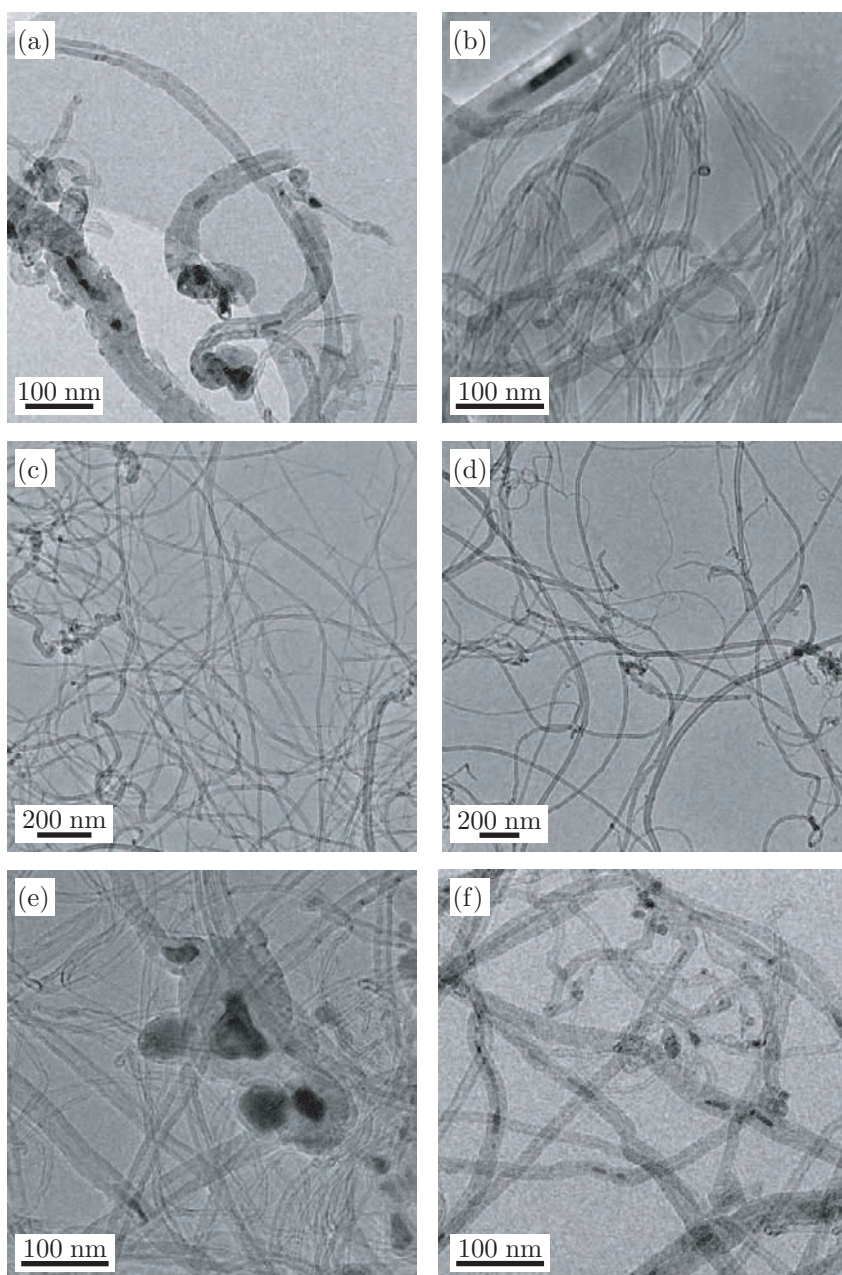


Figure 5.9: TEM micrograph of purified CCVD nanotubes grown at different cobalt contents of catalyst: (a) 0 mol%, (b) 25 mol%, (c) 33 mol%, (d) 50 mol%, (e) 75 mol%, (f) 100 mol%.

EELS was carried out on encapsulated particles present in a sample grown on an  $\text{Fe}_{0.75}\text{Co}_{0.25}$  catalyst (Figure 5.10). No embedded particles with  $\text{Fe}_2\text{Co}$  composition were found. Most of the particles are iron rich with a small amount of Co. Detailed quantitative analysis revealed that the cobalt content is lower than 10%, which suggests a phase different from that of  $\text{Fe}_2\text{Co}$ .

As derived from XRPD measurements, the catalyst of that composition forms a mixture of  $\text{Fe}_3\text{C}$  and  $\text{Fe}_2\text{Co}$ . Therefore we can conclude that the encapsulated particles predominantly originate from  $\text{Fe}_3\text{C}$  cementite doped with cobalt. For  $x > 33$  mol%, the catalyst forms  $\text{Fe}_2\text{Co}$  and  $\text{Co}$ . By increasing the cobalt content, the quantity of embedded  $\text{Co}$  particles increases. When  $\text{Co}/\text{CaCO}_3$  is used, up to 80% of MWNTs are partially filled (Figure 5.9f). Therefore, we assume that the lower catalytic activity of  $\text{Fe}_3\text{C}$  and  $\text{Co}$  compared to  $\text{Fe}_2\text{Co}$  originates from their tendency of being encapsulated in the nanotubes. The encapsulation reduces the surface contact of the  $\text{Fe}_3\text{C}$  or  $\text{Co}$  catalytic particles with acetylene. Therefore, this could be considered as a catalyst poisoning, which limits CNT production.

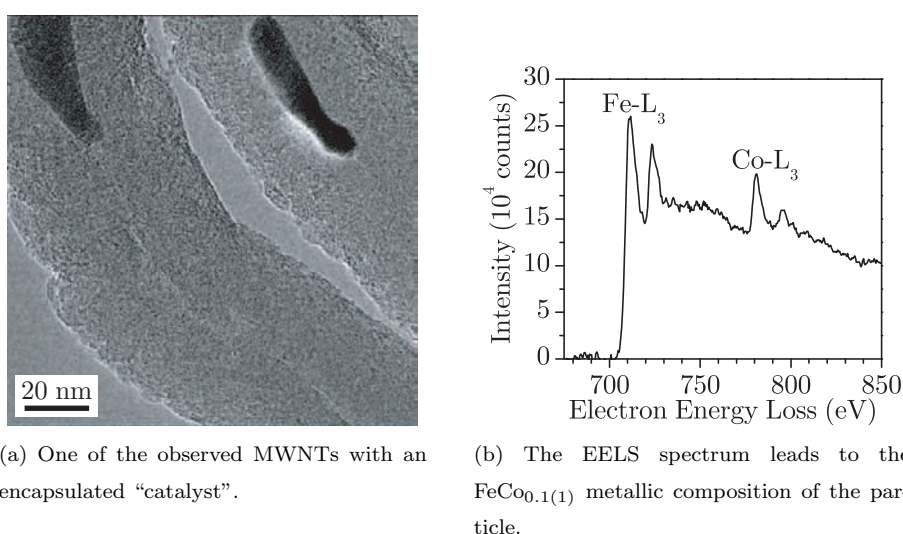
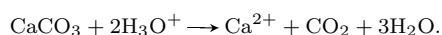


Figure 5.10: TEM micrograph and EELS spectrum of an encapsulated particle. MWNT was grown on  $\text{Fe}_{0.75}\text{Co}_{0.25}$  catalyst.

### 5.3 Catalyst support

During purification of the crude product, an interesting feature emerged about CNTs grown using a  $\text{CaCO}_3$  support. In some growth conditions, CNT dispersion in diluted  $\text{HCl}$  was accompanied with gas release<sup>4</sup>. No remarkable release was observed when CNTs grown under the optimum yield composition (100 mg of  $\xi = 33$  mol% as-prepared catalyst, at  $660^\circ\text{C}$  for 30 minutes) were dispersed in the diluted acid while some deviations from these parameters led to a significant gas release. Moreover, no gas release was observed when unsupported catalyst was

<sup>4</sup>When a carbonate, for instance  $\text{CaCO}_3$  is mixed with a diluted acid ( $\text{HCl}$ ),  $\text{CO}_2$  gas is released.





used. The gas, identified as  $\text{CO}_2$ , seems to be a side-product of the catalyst carrier  $\text{CaCO}_3$ , which decomposes into  $\text{CaO}$  and  $\text{CO}_2$  during CNT production. Actually, these phenomena induced a detailed study of the influence of the  $\text{CO}_2$  groups in the support of the CNT growth.

Consequently, the presence of gas development during purification can directly be correlated with the decomposition state of  $\text{CaCO}_3$  during growth. When no gas is released during purification, the decomposition can be considered as having fully taken place during growth whereas the remaining  $\text{CaCO}_3$  decomposes during the purification and leads to gas release. Since the amount of  $\text{CO}_2$  released was found to depend strongly on the growth condition, we assume that the  $\text{CO}_2$  groups originating from  $\text{CaCO}_3$  decomposition also play a role in the growth of MWNTs. When optimum parameters are used,  $\text{CO}_2$  is completely consumed during the growth process (no release during purification). Whereas with a different catalyst composition than  $\xi = 33$  mol  $\text{CO}_2$  is not completely devoured during growth and a  $\text{CO}_2$  release is observed during purification.

In order to substantiate any role of the support, CNTs were grown using different alkaline earth carbonates ( $\text{MCO}_3$ ,  $\text{M}=\text{Mg}$ ,  $\text{Ca}$ ,  $\text{Sr}$  or  $\text{Ba}$ ) as support, and keeping the optimum conditions for growth ( $\text{C}_2\text{H}_2$ ,  $\text{N}_2$ , 100 mg of  $\xi = 33$  mol% as-prepared catalyst,  $700^\circ\text{C}$ , 30 min of reaction time).

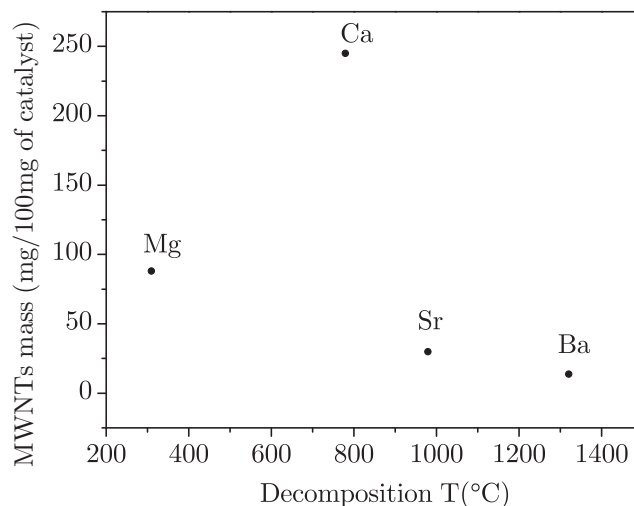


Figure 5.11: The obtained nanotubes on earth carbonates as a function of their decomposition temperature in the case of 100 mg  $\xi = 33$  mol% as-prepared catalyst, at  $700^\circ\text{C}$  for 30 minutes.

The plot of Figure 5.11 shows the evolution of the deposited carbon quantity versus the decomposition temperature of the carbonates<sup>5</sup>. SEM confirmed the pro-

<sup>5</sup>Decomposition temperature of  $\text{MCO}_3$ -s were quantified by thermogravimetry analysis (TGA).

duction of nanotubes for all samples and showed that the yield is higher when the working temperature of the furnace is closer to the decomposition temperature, which is in agreement with earlier observations (Figure 5.12). The highest yield is obtained with  $\text{CaCO}_3$ , with a decomposition temperature ( $770^\circ\text{C}$ ) closest to the CNT growth temperature ( $700^\circ\text{C}$ ).

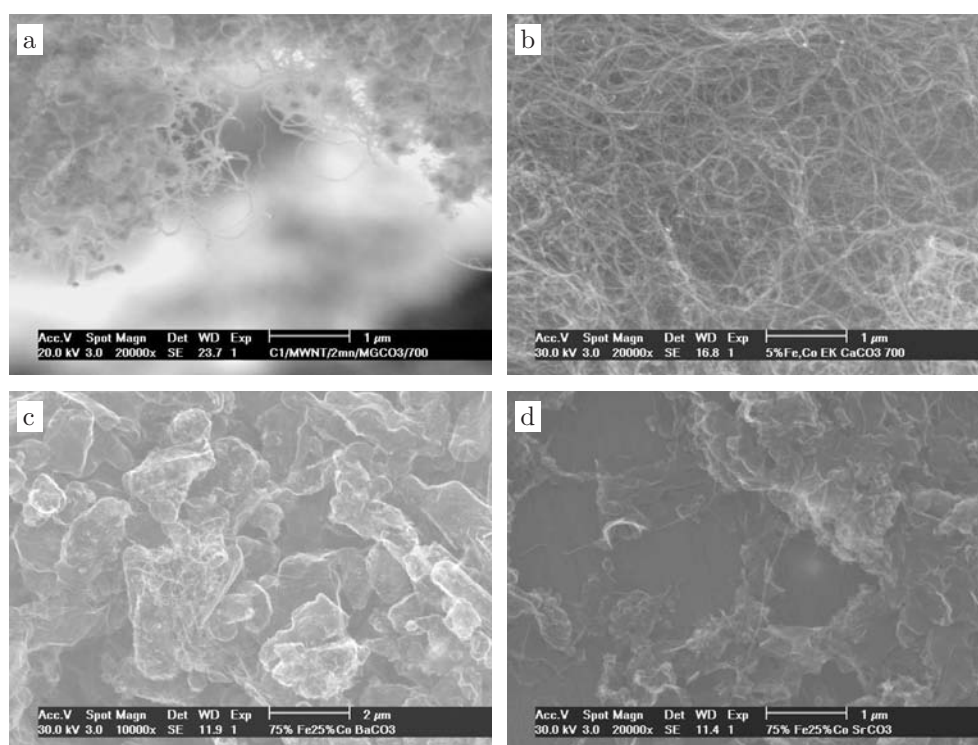
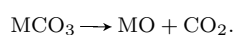


Figure 5.12: SEM micrographs of the CNTs obtained on  $\xi = 33$  mol% catalyst supported by earth alkaline supports (a)  $\text{MgCO}_3$ , (b)  $\text{CaCO}_3$ , (c)  $\text{BaCO}_3$  and (d)  $\text{SrCO}_3$ .

In the case of  $\text{MgCO}_3$  and  $\text{CaCO}_3$ , nets of CNTs are clearly visible at  $700^\circ\text{C}$  of growth temperature. For  $\text{SrCO}_3$  and  $\text{BaCO}_3$  only a few nanotubes were found in the product. In case of  $\text{MgCO}_3$ , since the growth temperature is much higher than the decomposition temperature, the support is completely transformed to the corresponding oxide ( $\text{MgO}$ ). At the growth temperature, where acetylene is introduced, no  $\text{CO}_2$  is present to take part in the growth process.

For  $\text{SrCO}_3$  and  $\text{BaCO}_3$ , the decomposition temperatures are substantially higher than the working temperature. Hence, both carbonates are very stable at the temperature of the CNT growth. Decomposition is avoided, since  $\text{CO}_2$  groups are

The decomposition is as follows:



strongly bonded to the support and the reaction with acetylene is limited. Indeed a strong  $\text{CO}_2$  release during the purification has been observed.

According to previous experiments, the  $\text{CO}_2$  groups can be involved in the growth of CNTs. A new series of experiments was performed with  $\text{Fe}_2\text{Co}$  catalyst over  $\text{CaCO}_3$  support and the growth temperature ranging from  $600^\circ\text{C}$  to  $820^\circ\text{C}$  for 30 minutes of retention time. This corresponds to the temperature range of the decomposition of  $\text{CaCO}_3$  determined by TGA (Figure 5.13) The evaluation of the CNT yield as a function of temperature is plotted in Figure 5.14. Fitting a lognormal function to the points the maximum yield is about  $660^\circ\text{C}$ .

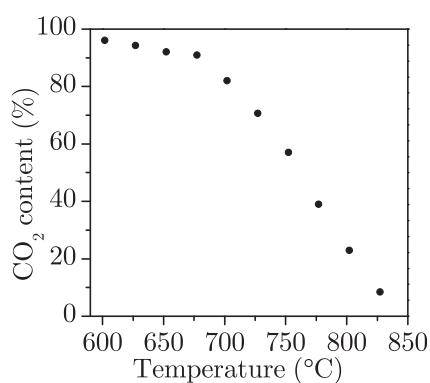


Figure 5.13:  $\text{CO}_2$  content of  $\text{CaCO}_3$  versus temperature from TGA analysis.

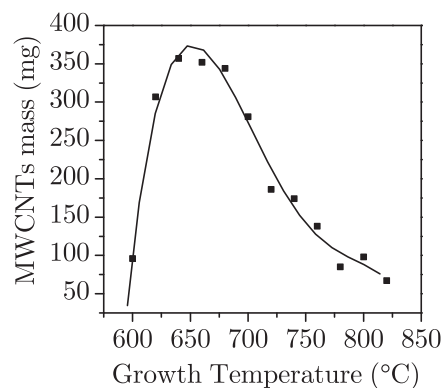


Figure 5.14: Carbon yield in function of growth temperature.

A clear correlation is visible between the decomposition behaviour of  $\text{CaCO}_3$  and the quantity of MWNTs.

For temperatures below  $680^\circ\text{C}$ , the decomposition of  $\text{CaCO}_3$  is reduced (i. e. the  $\text{CO}_2$  content of the support is lost) by 10%. Between  $600^\circ\text{C}$  and  $680^\circ\text{C}$  the  $\text{CO}_2$  groups are thermally activated as the temperature is raised ( $\text{CaO-CO}_2$  bonds in the support are weakened). Therefore CNT mass increases dramatically with temperature. Nevertheless, a saturation of CNT production is observed due to kinetic limitation.

Above  $680^\circ\text{C}$ , the  $\text{CO}_2$  content of the support dramatically decreases as the growth temperature is raised. Consequently, growth of MWNTs is drastically reduced.

One should note, that when the temperature is increased to  $1000^\circ\text{C}$ , thick nanofibers along with amorphous carbon are produced instead of MWNTs (Figure 5.15). Below  $800^\circ\text{C}$  acetylene decomposition is kinetically limited while it is not catalysed. Above  $800^\circ\text{C}$   $\text{C}_2\text{H}_2$  dissociates spontaneously and the reaction gas

contains, therefore, a significant fraction of free carbon, which will form larger aggregates in order to avoid dangling bonds. These large carbon clusters travel with the carrier gas and are deposited everywhere; on the substrate, on the surface of carbon fibres as well as on the quartz tube.

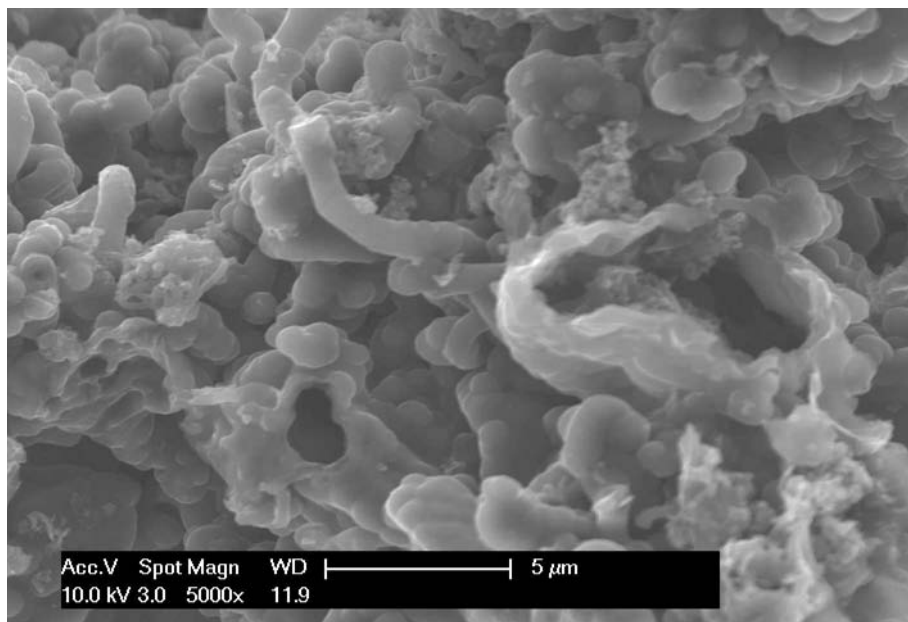


Figure 5.15: High temperature growth of “nanotubes”. At 1000°C the acetylene decomposes spontaneously forming thick fibers.

## 5.4 Retention time

Once the catalyst composition, support and the temperature had been optimised, the carbon yield versus retention time was studied, Figure 5.16. At the optimal parameters ( $\text{Fe}_2\text{Co}/\text{CaCO}_3$  catalyst at 660°C) a rapid increase in the CNT yield is followed by a saturation of nanotube production. The maximum quantity of CNTs is reached after 30 min of reaction time.

The process of CNT production, actually, can be divided in two regions:

1. The first part of the reaction (2 to 30 minutes) is dominated by the rapid growth of the CNTs. Within this period, no clear variation in the length or in the outer diameter of CNTs have been observed. This means that the growth kinetic of tubes is much faster than our shortest reaction time (2min). 1-50 microns per minute growth rate have been measured previously by Bonard et al. [104] and Geohegan et al. [105] by in situ growth rate measurements.

2. For Longer exposure time than 30 minutes, almost all the catalyst particle or  $\text{CO}_2$  groups from the carbonate were completely consumed.

One should note that the saturation level is reduced by raising the temperature and also that the saturation point is shifted towards higher exposition time.

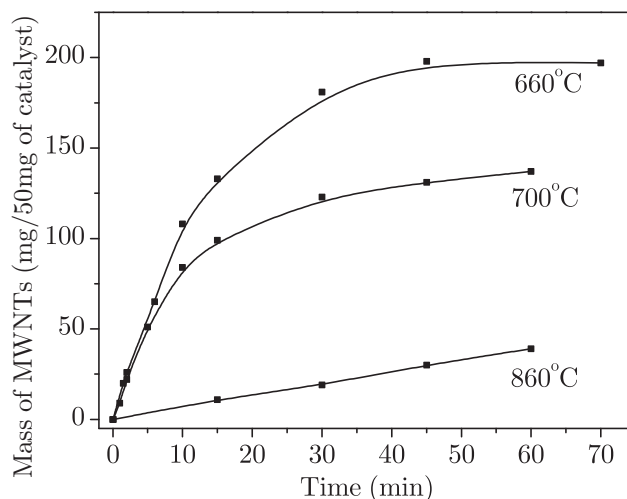


Figure 5.16: The amount of the nanotubes produced as a function of time at three different temperatures. CNTs were grown over 50 mg of  $\text{Fe}_2\text{Co}/\text{CaCO}_3$  catalyst.

## 5.5 Mass production

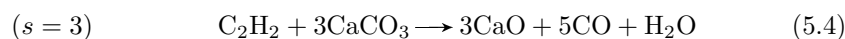
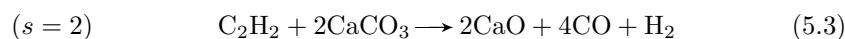
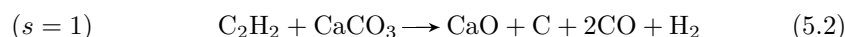
From the previous parametric study, 5 wt% of  $\text{Fe}_2\text{Co}$  catalyst supported by  $\text{CaCO}_3$ , annealed for 30 minutes under  $\text{C}_2\text{H}_2/\text{N}_2$  (fluxed at 1 L/h and 70 L/h respectively) at  $660^\circ\text{C}$  were found as the optimum parameters. High Resolution TEM observations have not shown drastic structural improvement of the structures of CNTs at higher temperatures but much less quantity,  $660^\circ\text{C}$  reaction temperature was therefore chosen for mass production. Obviously, some of the optimum parameters are strongly correlated: the gas flux and the retention time to the quantity of catalyst used. In the rotary tube furnace, a larger quantity of powder is passes at the same time through the heated zone of the rotary tube. Therefore we had to enrich the gas with acetylene and increase the retention time of the powder. The influence of rotation speed and inclination of the quartz tube were checked. After several runs, they were set to 1 rpm and  $15^\circ$ , respectively.

In the standard fixed-bed reactor, where the parametric study was performed, up to 6.5 g a day of purified MWNTs can be produced. With this rotary furnace technique, a daily production rate reached the order of kg for high quality purified MWNTs.

## 5.6 Growth mechanism

In order to understand the chemical mechanism (role of carbonate) which takes place during growth, first, the possible reactions between  $\text{CO}_2$  and  $\text{C}_2\text{H}_2$  should be studied.

Reactions can occur when acetylene is adsorbed on the catalyst surface and when it is in contact with  $\text{CO}_2$  groups from carbonate. The  $\text{C}_2\text{H}_2/\text{CO}_2$  proportion can be illustrated by the symbols  $s$ ,  $p$  and  $q$ , where the  $s$  index is calculated as  $s = p/q$  from  $p \text{ C}_2\text{H}_2 + q \text{ CaCO}_3 \rightarrow \text{CaO}, \text{C}, \text{H}_2, \text{CO}, \text{H}_2\text{O}$ . Possible reactions between acetylene and  $\text{CO}_2$  groups for  $s = 1, 2, 3$ :



In these suggested chemical processes carbon could be produced directly from reactions 5.1 and 5.2 or afterwards from end-products of reactions 5.2, 5.3 and 5.4 via the disproportionation of carbon monoxide ( $2\text{CO} \rightarrow \text{C} + \text{CO}_2$ ). In order to establish the favoured reactions according to the temperature range, Gibbs energies have been calculated for each reaction listed above using Barin tables [106] and represented as a function of temperature<sup>6</sup>.

According to the calculation of Gibbs energies,  $s = 1$  reactions are favoured below  $790^\circ\text{C}$ . At  $680^\circ\text{C}$ , the curve of reaction 5.1 intersects with that of reaction 5.2 indicating a change in the chemical process of the growth. This temperature corresponds to the discontinuity observed in Figure 5.13. Actually, due to the reaction stoichiometry, below  $680^\circ\text{C}$  two carbon atoms are produced in one step per  $\text{C}_2\text{H}_2$  molecule (reaction 5.1). Above  $680^\circ\text{C}$  carbon atoms are produced within two steps: the first from the reaction of  $\text{C}_2\text{H}_2$  and  $\text{CaCO}_3$  (Reaction 5.2) and the second during CO disproportionation. Considering the growth conditions, CO disproportionation is limited [107], therefore, above  $680^\circ\text{C}$  less than two carbon atoms per acetylene molecule can be produced for MWNTs. This is in agreement with the decrease of the amount of MWNTs produced for the growth temperature above  $680^\circ\text{C}$  (Figure 5.14 on page 51).

<sup>6</sup>The calculation of Gibbs energies:  $\Delta G_{\text{reaction}} = \Delta G_{f_{\text{products}}} - \Delta G_{f_{\text{reactants}}}$ , where  $f$  means formation. Example:  $\Delta_{\text{reaction},s=2} = 2\Delta_{f_{\text{CaO}}} + 4\Delta_{f_{\text{CO}}} - \Delta_{f_{\text{C}_2\text{H}_2}} - 2\Delta_{f_{\text{CaCO}_3}}$ .

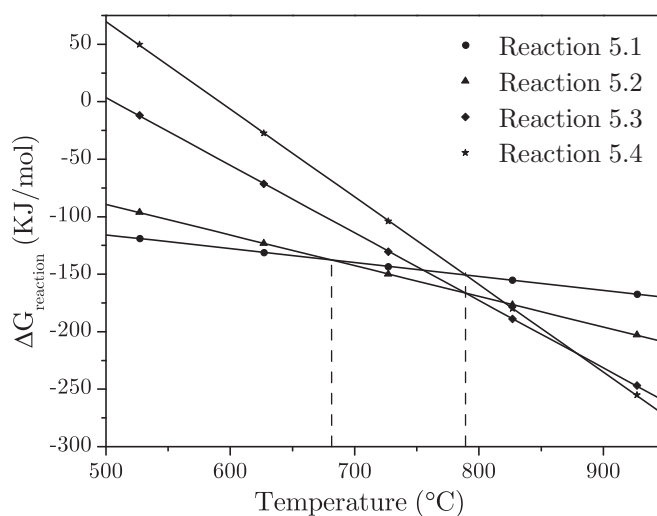


Figure 5.17: The calculated Gibbs energies for all the reaction equations listed above.

Above 790°C reactions 5.3 and 5.4 are favoured according to Gibbs energy calculations. Nevertheless,  $\text{CaCO}_3$  is almost fully decomposed. Therefore, the contribution of carbon produced from the reaction of  $\text{C}_2\text{H}_2$  and  $\text{CO}_2$  is negligible. MWNTs are produced via spontaneous acetylene cracking reaction ( $s = 0$ ,  $\text{C}_2\text{H}_2 \rightarrow 2\text{C} + \text{H}_2$ ).

## 5.7 Conclusion

This chapter described a systematic study of the effect of catalyst composition, catalyst carrier and retention time on the yield and quality of CNTs grown by CCVD.

The catalyst composition has a great influence on the final product. The highest yield, the narrowest diameter distribution, the least defects have been obtained at  $\xi = 33$  mol%. For this composition, the metallic pair of the catalyst consists of a single phase  $\text{Fe}_2\text{Co}$  alloy. Enrichment in Co or Fe produces an extra phase, which lowers the catalytic activity for CNT production due to particle encapsulation.

During this parametric study,  $\text{CaCO}_3$  and 660°C were found to be the optimum support and growth temperature, respectively. This is related to the involvement in the growth process of the alkaline earth carbonate we have reported.

Some reports indicated the usefulness of oxygenated species in addition to the reactor chamber during the growth, in order to enhance the production quality of CNTs. They refer to the role of these species as agents avoiding the formation of amorphous carbon but not directly involved in the chemistry of the growth process. Other groups showed the influence of the support on the CNT production. Up to

now, no clear understanding of the role played by the support itself has presented.

In this chapter, we have shown a clear involvement of the support in the nanotube growth process by reaction of  $C_2H_2$  and  $CO_2$  species from the support. Possible growth processes were also presented depending on the growth conditions. Finally, the understanding of the effect of each growth parameter allowed a high yield production of nanotubes of the order of kilogram per day.



## Chapter 6

# Assembly, Mechanical Characterisation and Reinforcement of Macroscopic Carbon Nanotube Fibres

We have seen in Chapter 2 that due to their tubular structure nanotubes are expected to have very remarkable mechanical properties. In the previous chapter, the growth of good quality CNTs has been described and a method for the large-scale production of them presented. These two things raise the possibility of using nanotubes as reinforcement in composites. In fact, this possibility has been the subject of intense research [108, 11, 109, 110, 10, 111].

In this chapter we will focus on the fabrication of CNT based materials with interesting *macroscopic* properties. Since the mechanical and electronic properties of CNTs are strongly anisotropic, aligned CNT-based fibres are of particular interest. We will present results obtained earlier and starting from Section 6.4 we will talk about methods of preparation, the mechanical and electrical measurements and the reinforcement of CNT fibres we have done.

From the mechanical point of view, SWNTs in fibres are weakly coupled to each other by van der Waals interaction [12]. This leads to very weak fibres despite the enormous strength of the nanotubes themselves. This phenomenon of intertube

sliding is analogous to the mechanical behaviour of graphite. A single layer of graphite (graphene) has a high interplane modulus. Still, due to the weak van der Waals interaction between the successive layers, these can easily be peeled off; this enables the use of graphite in pencils. Similarly, the mechanical strength of a macroscopic nanotube fiber is limited by the small intertube shear modulus. (The fiber is torn apart before the individual nanotubes would break.) This leads almost naturally to the idea that tubes should be crosslinked, preferably with chemical bonds to increase the shear strength. We will present two ways to do this.

## 6.1 Overview of measurement techniques

### 6.1.1 Mechanical measurements

Because of their size, almost all measurements on individual CNTs require a microscope: SEM, TEM or AFM. The development of mechanical measurements on nanoscale objects inside microscopes was highly motivated by the exceptional properties of carbon nanotubes. In order to relate the elastic properties of CNTs to the macroscopic world, CNTs are usually described by using terms from the continuum theory of elasticity like the Young's modulus ( $E$ ) and the shear modulus ( $G$ ).

### 6.1.2 Strength of single carbon nanotubes

#### Thermal and electrical excitations in TEM

The first mechanical measurements of CNTs were based on measuring the amplitude of thermally induced vibration of the tubes inside a TEM [55]. MWNTs were fixed at one end and the other, free end was vibrating due to the thermal excitation of the nanotube's mechanical resonant modes. As the vibrational frequency was high enough compared to the acquisition time, the free end appeared blurred on the TEM images. The elastic modulus was calculated from a series of measurements performed as a function of temperature yielding an average value of 1.8 GPa for the bending modulus. Similar measurements were performed on SWNTs [112] with an average value of  $1.25 \pm 0.35$  TPa. Although the individual measurements were subject to large error bars (20 – 60%), they had a great impact since this was the first indication about the extraordinary Young modulus of carbon nanotubes [64].

Poncharal et al. [56] performed similar TEM measurements, relying on electrical excitation of CNTs. Nanotubes were mounted on a specially designed TEM holder where they were contacted electrically and brought close to a grounded counter-electrode. MWNTs were directly excited using an AC electric field (Figure 6.1) and

$E_{\text{Young}}$  was calculated from the frequencies of the first two resonant modes.

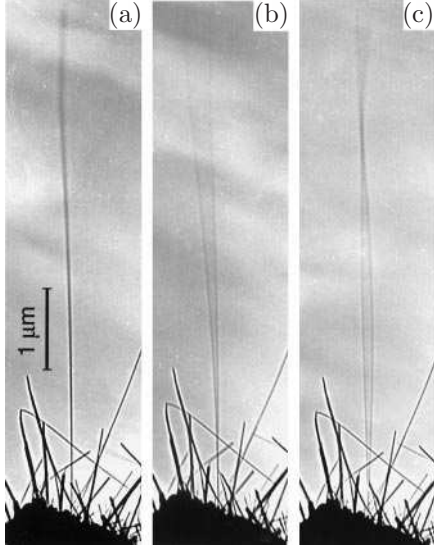


Figure 6.1: Nanotube response to resonant alternating applied potentials. (a) In the absence of a potential, (b) at the fundamental mode of vibration and (c) the second harmonic.

When a static potential  $V_s$  is applied to the tube, it becomes electrically charged and is attracted to the counter-electrode. The induced charge is proportional to the applied voltage and is equal to  $\alpha V_s$ . The force exerted on the nanotube is given by the product of the induced charge and the electric field ( $\beta V_s$ ), and is therefore equal to  $F = \alpha\beta V_s^2$ . Application of an additional time-dependent voltage  $V(t) = V_d \cos(\omega t)$  to the nanotube causes a time-dependent force  $F(t)$  given by the expression:

$$\begin{aligned} F(t) &= \alpha\beta(V_s + V_d \cos(\omega t))^2 \\ &= \alpha\beta \left( V_s^2 + 2V_s V_d \cos(\omega t) + \frac{1}{2} V_d^2 \cos(2\omega t) + \frac{1}{2} V_d^2 \right). \end{aligned} \quad (6.1)$$

By adjusting the frequency  $\nu$  in  $\omega = 2\pi\nu$ , tubes can be resonantly excited (Figures 6.1 and 6.2) and the elastic modulus ( $E$ ) can be calculated from the frequency response using a formula from the Bernoulli-Euler analysis of cantilevered elastic bars:

$$\nu(j) = \frac{\beta_j^2}{\pi} \frac{1}{L^2} \sqrt{D_{\text{out}}^2 + D_{\text{int}}^2} \sqrt{\frac{E}{\rho}}, \quad (6.2)$$

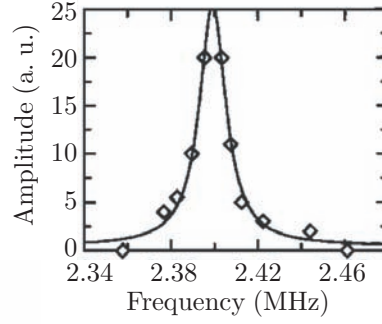


Figure 6.2: Mechanical resonance of a nanotube in an applied electric field [56].

where  $D_{\text{out}}$  is the outer diameter,  $D_{\text{int}}$  the inner diameter,  $L$  the length,  $\rho$  the density,  $\beta_j$  a constant for the  $j^{\text{th}}$  harmonic:  $\beta_1 = 1.875$  and  $\beta_2 = 4.694$  [64].

For MWNTs with diameters below 10 nm the elastic modulus was about 1 TPa, while it dropped to 100 GPa for thicker tubes. Such a great reduction in the modulus was associated with the emergence of another bending mode of the tube. A wave-like distortion or ripple on the inner arc of the bent nanotube shown in Figure 6.3 was observed for slightly bent, relatively thick nanotubes. In contrast, a thin slightly bent nanotube (8 nm in diameter) did not present them. The ripples presumably appear in order to reduce the compression of the carbon bonds of the inner arc.

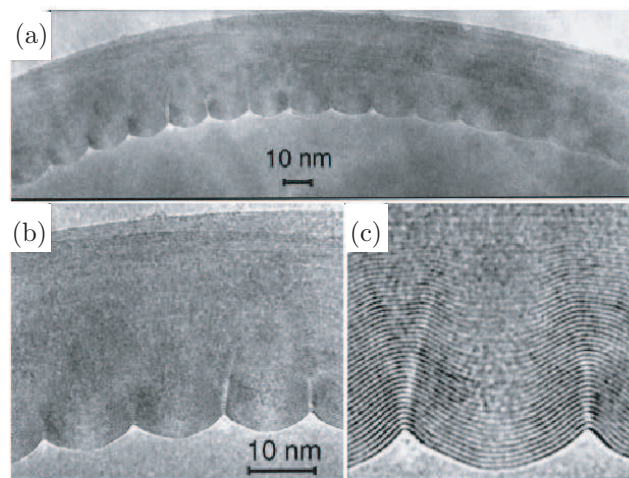


Figure 6.3: (a) High-resolution TEM image of a thick, bent nanotube showing a characteristic wave-like distortion – rippling. (b) and (c) are magnified views of a portion of (a) [56].

### Elastic and shear moduli of nanotubes measured by AFM

Salvetat et al. measured the Young's modulus of isolated SWNTs and SWNT ropes, MWNTs produced by arc discharge and catalytic chemical vapour deposition as well as shear modulus in SWNT ropes by a series of experiments in an AFM (Figure 6.4) [12, 57, 113].

In this measurement, CNTs were dispersed in ethanol and deposited on the surface of a polished alumina ultrafiltration membrane. Tubes adhered to the surface due to van der Waals interaction, occasionally spanning holes (Figure 6.4a). When a nanotube was found lying over a hole, a series of contact-mode AFM images were taken under increasing loads. During AFM imaging in contact mode, the tube deforms under an applied normal force and this deformation is recorded as local height in the corresponding AFM image [64].

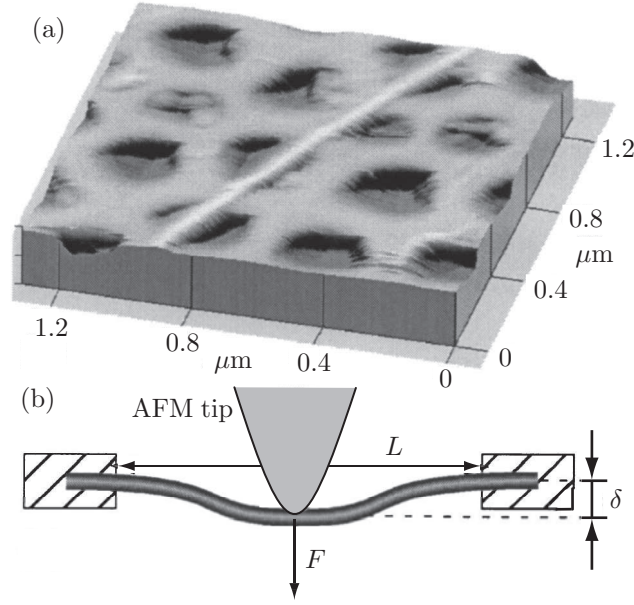


Figure 6.4: (a) AFM image of a SWNT rope adhering to the polished alumina ultrafiltration membrane, with a portion bridging a pore of the membrane. (b) Schematic of the measurement: the AFM is used to apply a load to the nanobeam and to determine directly the resulting deflection [12].

Extracted line-scans across the tube, like the one in Figure 6.4a, reveal the vertical deformation. For the range of applied normal loads, the midpoint deflection of a long, thin nanotube under a nominal point load  $F$  can be fitted using the clamped beam formula:

$$\delta = \frac{FL^3}{192E_{\text{Young}}I}, \quad (6.3)$$

where  $L$  is the suspended length and  $I = \frac{d^4}{64}\pi$  the second moment of the cross-section for a solid cylinder of diameter  $d$  [114].

Using this technique, Young's modulus of  $1.0 \pm 0.5$  TPa was found for SWNTs. Values for MWNTs show a strong dependence on the amount of disorder in the graphitic layers – an average value of  $E_{\text{Young}} = 870$  GPa was found for the arc-discharge grown tubes, while the catalytically grown thick MWNTs, known to have a high concentration of defects can have a Young's modulus as low as 12 GPa [57].

When measuring SWNT ropes, the bending modulus decreases. In order to account for this, intertube shearing has to be taken into consideration. Single CNTs are held together in the rope only via the weak van der Waals interaction. As a consequence, ropes behave as an assembly of individual tubes and not as a homogeneous, thick beam. In their model, the entire nanotube bundle is treated as a single anisotropic cylinder. The Young's modulus  $E_{\text{Young}}$  corresponds to the

“stretchiness” of nanotubes. The shear modulus  $G$  describes the intertube sliding. In no way does it represent the shear modulus of single nanotubes – it is called the shear modulus because it plays the same role in the bending of nanotube bundles as the shear modulus in the bending of macroscopic beams [64]. The deflection can be modelled as a sum of deflections due to bending and shearing [114]:

$$\delta = \delta_{\text{bending}} + \delta_{\text{shearing}} = \frac{FL^3}{192E_{\text{Young}}I} + f_s \frac{FL}{4GA} = \frac{FL^3}{192E_{\text{bending}}I}, \quad (6.4)$$

where  $f_s = \frac{10}{9}$  is the shape factor for a cylinder,  $G$  is the shear modulus and  $A$  the area of the beam’s cross-section.  $E_{\text{bending}}$  is the effective bending modulus, equal to the Young’s modulus when the influence of shearing can be neglected (for long, thin ropes). The elastic and the shear modulus can thus be determined by measuring the  $E_{\text{bending}}$  of an ensemble of ropes with different diameter to length ratios [64].

### 6.1.3 Electrical resistivity measurements

Electrical resistivity is calculated from the measurement of the resistance, the length and the cross-section of the sample according to Ohm’s law:

$$\varrho = \frac{RA}{L}, \quad (6.5)$$

where  $\varrho$ ,  $R$ ,  $A$ ,  $L$  denote electrical resistivity, resistance, cross-section and length of the sample, respectively. In the case of CNT measurements the classical two-probe configuration is not applicable since the value of contact resistance can be quite high, thus four-point measurements have to be done.

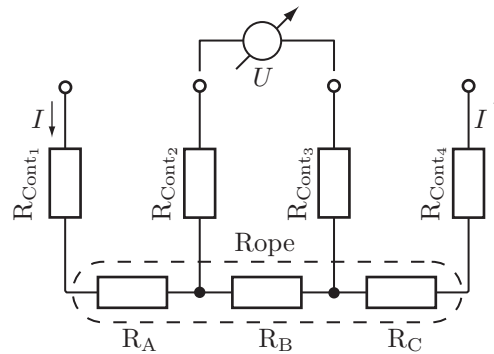


Figure 6.5: Schematics of the four-contacts measurement. The resistance ( $R_B$ ) measured between the two middle contacts and the calculation of the resistivity ( $\varrho$ ) is based on equation (6.5).

This method gives the real specimen resistance since the current and the voltage contacts are separated. Four contact resistivity measurements are performed as follows: the current passes through the sample via the two outer contacts, while the voltage is measured on the two inner contact points. The resistance is calculated from Ohm's law.

#### 6.1.4 Four-probe resistivity measurements

Electrical measurements on individual CNTs by the four-probe technique rely on sub-micron fabrication technology. Single multiwall carbon nanotubes could successfully be connected with relatively low-ohmic contacts by Bachtold et al. [115, 45]. In order to make four electric contact to a MWNT, high-resolution electron beam lithography was used to pre-structure a  $2 \times 2 \text{ cm}^2$  oxidised silicon substrate. Figure 6.6 presents the experimental arrangement. The four gold contact electrodes are 25 nm thick, 100 nm wide and  $6 \mu\text{m}$  long. In order to deposit a nanotube above the contacts, purified nanotube powder was homogeneously dispersed in chloroform by ultrasonication. A drop of this solution was deposited on the pre-structured substrate. After the evaporation of the solvent, two and four-probe electrical resistivity was measured. From measurements a resistivity of  $3 \times 10^{-5} \Omega\text{cm}$  was deduced.

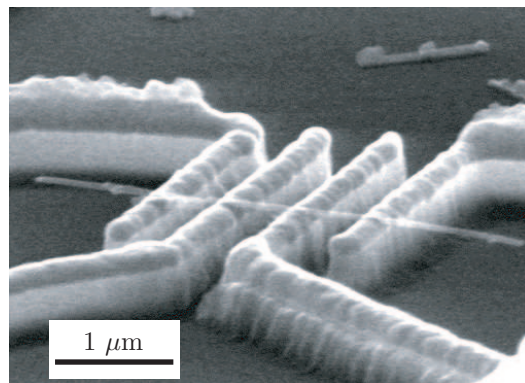


Figure 6.6: A scanning electron microscope image of a multiwall nanotube lying across four gold electrodes. Contacts were fabricated by electron-beam lithography prior to the deposition of the nanotube [116].

## 6.2 Assembly of nanotubes to macroscopic fibers

Large-scale production methods open the way to the use of CNTs as reinforcement in composites. In this section we will present a few methods to produce ordered, macroscopic fibres of CNTs.

### 6.2.1 Methods of alignment of CNTs

To align CNTs the following three different approaches are known:

1. *in-situ alignment*, which means direct synthesis of aligned CNTs. This is done typically by CCVD.
2. *post-synthetic orientation* consists of alignment of dispersed nanotube soot.
3. *hybrid alignment* produces fibres from a CNT carpet by post-processed winding.

#### In-situ alignment

There are two ways to align the CNTs in direct synthesis: either perpendicular to the surface, growing carpet like structures or in fibre form parallel to the axis of the nanotube. The perpendicular alignment can be important in flat screen manufacturing where nanotubes are used as electron emitters, while the parallel aligned fibers can in principle make use of the excellent mechanical properties of CNTs.

#### Perpendicular alignment

In this case catalyst is deposited on a flat carrier. Nanotubes are grown by CCVD, and they align with each other perpendicular to the surface. As an illustration, in 2004, Iijima and coworkers [99] performed a very simple synthesis method to obtain a dense, thick and high purity SWNT “forest”, see Figure 6.7. They introduced an oxygenated species in the reactor in order to promote and preserve catalytic activity and lifetime. SWNTs were grown from ethylene by using argon or helium,  $H_2$  and a small and controlled amount of water vapour. By balancing the relative levels of ethylene and water, a dramatic improvement in CNT yield and purity was observed.

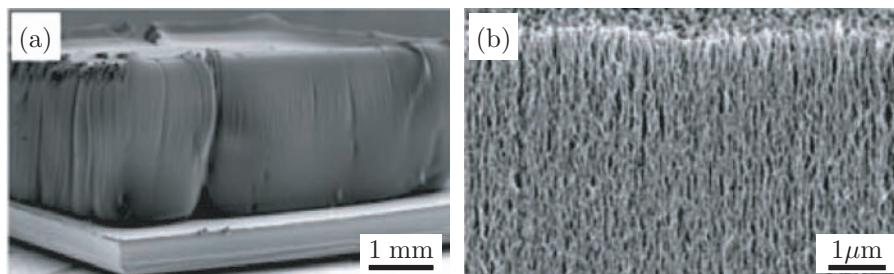


Figure 6.7: (a) SEM image of the obtained SWNT forest. (b) Magnified image of the SWNT forest edge [99].



### Parallel alignment

Zhu et al. [117] produced aligned strands using the float catalyst method in a vertical furnace where n-hexane ( $C_6H_{14}$ ) was catalytically pyrolysed in the presence of thiophene ( $C_4H_4S$ ) and hydrogen.<sup>1</sup> They used ferrocene ( $Fe(C_5H_5)_2$ ) as catalyst. The temperature and flow rates were optimised in order to produce long (up to 20 cm) SWNT strands in a continuous process containing roughly 5 wt% impurities such as iron and amorphous carbon, see Figure 6.8.

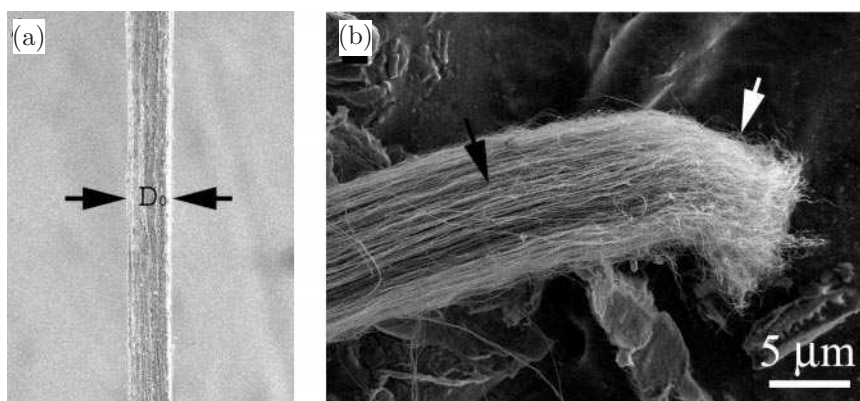


Figure 6.8: SEM micrograph of the SWNT strand from the article of Zhu [117].

### Post-synthetic orientation

Forming an oriented fibre from an isotropic powder of nanotubes is a major challenge. In most cases, the nanotubes are initially dispersed in a liquid medium [108, 118, 10]. For a stable suspension, CNTs either have to be chemically modified [119] or coated by adsorbed amphiphilic molecules [108]. From this suspension the alignment can be achieved magnetically, electrically or mechanically [120]. Many different methods have been published during the last few years to achieve ordered films or fibres of nanotubes. Here, we discuss melt and solution spinning, and the electrophoretic method.

### Melt-spun composite fibres

Melt spinning is used to produce many polymer fibres such as nylon. It can be applied to single components as well as composite fibres. In general, the components are melted and extruded under tension. Rapid cooling induces the solidification of the fibre. The schematic view of the three main spinning processes is drawn in Figure 6.9: melt, dry and wet spinning, respectively.

<sup>1</sup>Typically, ferrocene-assisted CCVD results in MWNTs at temperatures around 800°C and a mixture of single- and multiwall nanotubes at temperatures above 1000°C.

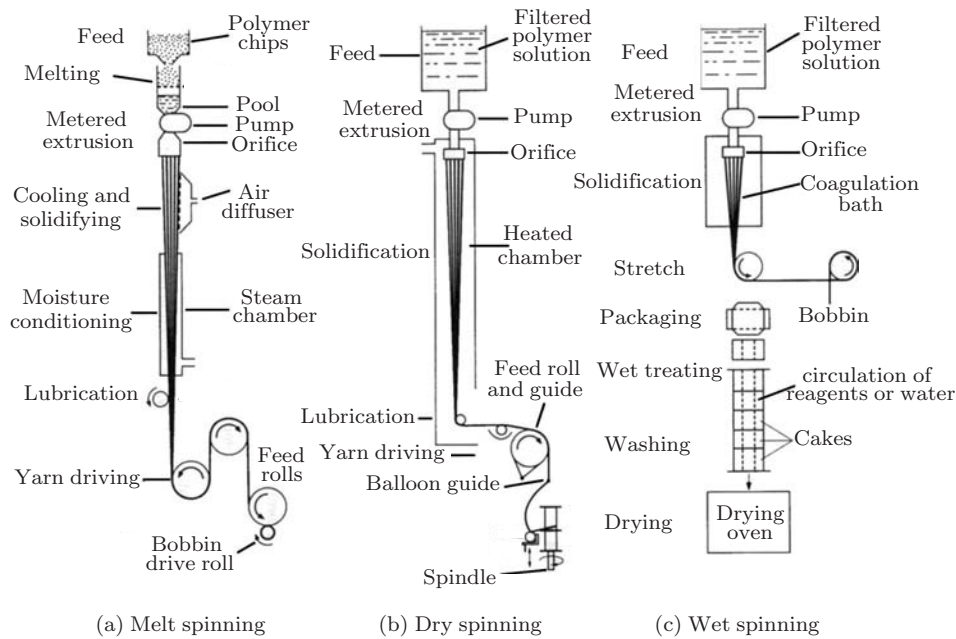


Figure 6.9: Schematic drawings about the three main type spinning process.

In the melt spinning, as described above, the first step is to melt all the components or to make a composite fluid. Since SWNTs decompose without melting at approximately  $750^{\circ}\text{C}$  in air, melt spinning is not a viable option for fibres where SWNTs are the only component. In the case of multi-component extrusion with a low melting temperature polymer, SWNTs can reinforce the polymer matrix [121, 10].

Some of the first melt-spun SWNT composite fibres were produced by Andrews et al. [122] using carbon pitch as matrix. Commercially available SWNTs were purified and sonicated with isotropic petroleum pitch in quinoline. The solvent was removed and the fibres were melt spun, drawn, and put through a two-stage heat treatment in air and nitrogen. Fibres containing 8 and 10 wt% of SWNTs were too viscous to be extruded. However, for fibres produced with 1 wt% and 5 wt% of SWNTs an improvement was observed in mechanical properties of up to 90% in tensile strength and up to 150% in elastic modulus, while the electrical resistivity dropped by 70%.

SWNT/Poly-methyl-methacrylate (PMMA) films and fibres were also produced by extrusion [123]. The SWNTs were dispersed in N,N-dimethyl-formamide<sup>2</sup> (DMF) and then in PMMA by prolonged sonication. After evaporation of the DMF, the resulting SWNT/PMMA pellets were extruded from a  $600\ \mu\text{m}$  orifice, and drawn under tension by a windup spool at high speed. The maximum draw ratio (defined as

<sup>2</sup>(CH<sub>3</sub>)<sub>2</sub>NCHO

$\lambda = (D_0/D)^2$ ) ranged from 60 to 3600, corresponding to fibre diameters between 75 and 10  $\mu\text{m}$ , respectively. Increasing SWNT content dramatically increased the melt viscosity; this resulted in melt fracture evidenced by surface roughness, striations along the fibre axis, and nonuniform diameter. Fibres were successfully produced from loadings up to 8 wt% SWNT.

Improvements in mechanical strength and electrical conductivity depended on SWNT concentration and the draw ratio. The improvements were consistent with the high degree of alignment measured by polarised Raman spectroscopy at multiple angles relative to the fibre axis [123].

Efforts to incorporate SWNTs into polypropylene (PP) fibres have been built on earlier success in incorporating carbon nanofibres into PP [124, 125, 126, 127]. Bhat-tacharyya et al. [128] produced 0.8 wt% SWNT-PP fibres using HiPCO<sup>3</sup> SWNTs and polypropylene. The SWNTs were purified and mixed with PP at 240°C, and filtered in order to remove the largest aggregates. This preparation procedure, however, failed to disperse satisfactorily the SWNTs, which remained clumped into domains of tens of micrometres. The SWNTs were found to promote faster PP crystallisation (probably by acting as nucleation sites) and to yield smaller PP crystallites. Mechanical properties were largely unaffected by the presence of the SWNTs as a result of the poor dispersion. In order to improve on the load transfer between the nanotubes and the PP matrix, better dispersing and chemical functionalisation of SWNTs is required [129].

Zhou et al. [10] extruded SWNT fibres from superacid suspensions. Alignment was characterised by X-ray and polarised Raman scattering. Electrical resistivity and thermal conductivity measurements showed that the fibres are heavily *p*-doped and conductivity can be enhanced by alignment. Further improvements in fibre alignment and properties would be facilitated by a more complete understanding of nanotube suspensions.

### **Solution-spun fibres and ribbons**

Although solution spinning is more complicated than the melt spinning process, it is favourable to use it for SWNT fibre assembling. The procedure, compared with melt spinning, involves additional steps because of the solidification of the fibre. First, the nanotubes must be finely dispersed in a solvent, and the solvent must be extracted after the extrusion to form the solid fibre. Therefore, solution spinning is typically used to produce fibres from materials that decompose before reaching their melting point or do not have a suitable viscosity for stable fibre formation.

---

<sup>3</sup>“HiPCO” process: from the words high-pressure carbon-monoxide [107].

The first truly scalable continuous process for making fibres composed primarily of SWNTs was developed by Vigolo et al. [108]. The original process is reminiscent of the flow induced alignment processes already used for rigid polymers or anisotropic colloids [108]. The fibres were composed of a network of SWNTs and an amphiphilic polymer, polyvinyl alcohol (PVA).

The nanotube bundles are dispersed in water with the aid of a commercially available surfactant molecule, sodium-dodecyl-sulfate (SDS). A detailed study of the phase diagram of the surfactant stabilised nanotube dispersions has been performed, in order to obtain a homogeneous suspension with a relatively important concentration of nanotubes (an optimum was found for 0.35 wt% of SWNTs and 1 wt% of SDS) [108, 9, 130]. The SWNT dispersion was then injected in a co-flowing stream of the polymer solution that contained 5 wt% of PVA. Amphiphilic polymers such as PVA are ineffective at stabilizing SWNTs; they only stick to each other almost as soon as they enter the bath. This can be considered as coagulation through bridging flocculation [9].

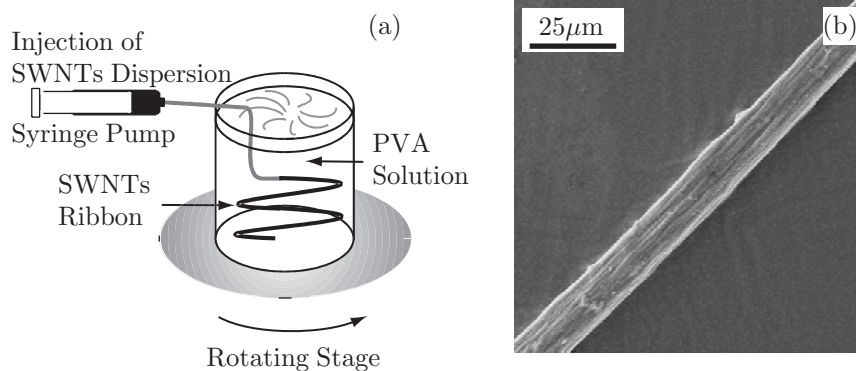


Figure 6.10: Schematic of the setup for producing carbon nanotube fibres by solution spinning. Suspension of purified nanotubes in SDS solution is introduced into a spinning beaker containing PVA. The nanotube suspension is destabilised by PVA and the nanotubes coagulate into fibres aligned with the flow direction. (b) A scanning electron micrograph showing a portion of the nanotube fibre [108].

Most of the surfactant leaves the filament during coagulation, while at the same time some of the PVA molecules penetrate the forming fibre and stabilise it by forming bridges with the SWNTs [108, 9]. The polymer can also be removed by washing the fibre repeatedly and by heating the fibre to temperatures between the decomposition temperature of the polymer and that of the SWNTs.

Polarised optical microscopy of ribbons suspended in water showed that there is a preferential alignment along the ribbon axis. The SEM micrograph in Figure

6.10b shows the preferential axial alignment in the cleaned dry ribbons although the dried ribbons displayed weaker anisotropy than the ribbons suspended in water.

Injecting the SWNT dispersion in a co-flowing stream of polymer has two benefits on the fibre formation. It aligns the SWNTs by tensioning the protofibre via velocity mismatch. Moreover the rotating bath supports and transports the protofibre during the early stages of coagulation, while it is still too weak to support any applied tension. If the coagulation bath were not moving, the fibre would have to be drawn mechanically through it, which is not possible unless the liquid filament has a high enough viscosity and withstands tension along the streamlines.

A modified, scaled-up process developed by the University of Texas uses a co-flowing stream of polymer solution [11]. SWNT suspensions are analogous to solutions of rod-like polymers or anisotropic colloids [130]. Just as the nature of surfactant plays a critical role in the phase behaviour of classical colloids, the same is true for nanotubes.

Four-probe electrical resistivity measurements gave a room temperature resistivity of approximately  $0.1 \Omega\text{cm}$  and showed nonmetallic temperature dependence. This value is three orders of magnitude higher than that of small bundles of SWNTs and is thought to be influenced by the presence of the polymer and carbon impurities.

Since nanotubes are connected only via van der Waals interaction or with the help of the intercalated polymer, their Young's modulus is determined by the intertube coupling and is low: Ranging from 15 GPa [108] to 80 GPa [11], depending on the production method.

### **Fibres made by electrophoretic spinning**

Gommans et al. [118] have developed a method for making fibres of SWNTs with a substantial degree of alignment along the fibre axis. This process is based on the electrostatic behaviour of SWNTs. First, a suspension is prepared consisting of 1 wt% of purified laser grown SWNTs in DMF. A commercially available carbon fibre is connected to a conducting wire and attached to a motor-driven translation stage, Figure 6.11. The carbon fibre is immersed into the nanotube suspension to a depth of few millimetres. The set-up is designed so that a voltage can be applied between the carbon fibre and a cylindrical electrode around it. The carbon fibre is connected to the positive electrode and the nanotubes migrate toward it and form a cloud around the carbon fibre. These nanotubes are polarised and thus they are aligned by the electrostatic field. Ordered macroscopic ropes of SWNTs are formed by slowly pulling out the the carbon fibre. As the carbon fibre is slowly replaced by

a fibre made from the cloud of nanotubes, at the end, pure CNT fibre is obtained.

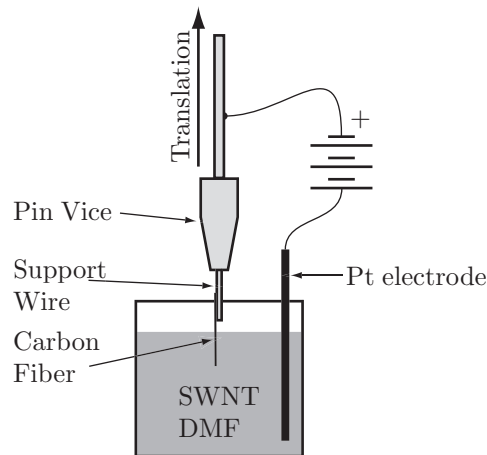


Figure 6.11: Electrophoretic SWNT fibre production setup. A potential of 1-2 V is applied between the commercial carbon fibre and the platinum counter-electrode for 10-30 min, leading to the formation of an ordered SWNT cloud. When the carbon fibre is slowly withdrawn from the solution it “draws” the aligned SWNT fibre [118].

The formation of a SWNT cloud around a positive electrode indicates that nanotubes are negatively charged when dispersed in DMF. Consequently, they migrate electrophoretically towards the positively charged carbon fibre. The fibres obtained are several centimetres long and their diameters typically range between 2 and 10 microns depending on the preparation conditions.

Selected area electron diffraction has been used to characterise the structure of the fibres. The results show a substantial degree of alignment of the nanotubes parallel to the fibre axis. The FWHM of the distribution was found to be  $23^\circ$ , showing a rather good alignment of nanotubes. However this probe was restricted to the side of the fibres to allow transmission of the electron beam.

### Hybrid alignment

This method has two distinct parts; the first is the growing of a very dense CNT carpet followed by the winding of the fibre. Baughman and coworkers [110] scaled down an ancient technique to form a MWNT yarn from a perpendicularly aligned dense MWNT film. The method is based on the spinning process of Jiang et al. [131] involving CNT drawing from a MWNT “forest”.

In this process CCVD MWNTs of 8-15 nm diameter were grown on a Si substrate coated by 5 nm thick iron catalyst. The feedstock was 5 mol% acetylene in helium at

680°C. MWNTs were simultaneously drawn from the MWNT carpet and twisted. The yarn diameters obtained ranged from 1 to 10  $\mu\text{m}$ , depending on the MWNT forest sidewall width (0.15 to 3 mm). A 200  $\mu\text{m}$  wide sidewall produced twisted yarn  $\sim 2 \mu\text{m}$  in diameter.

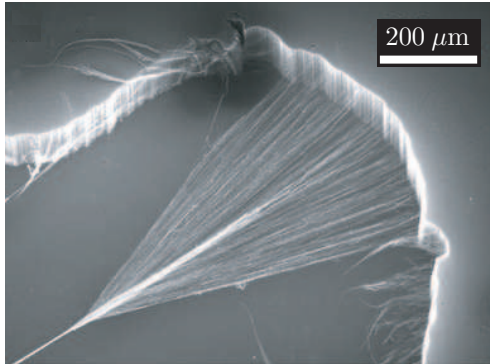


Figure 6.12: SEM image of a CNT yarn in the process of being simultaneously drawn and twisted during spinning from a nanotube forest outside the SEM.

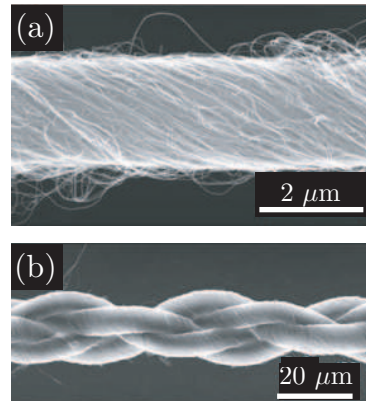


Figure 6.13: A scanning electron micrograph showing a portion of the nanotube fibre, single and four plied [110]. The single yarn was 3.2  $\mu\text{m}$ .

The draw-twist process was interrupted and the sample transferred to a SEM for image recording (Figure 6.12). A forest strip (width roughly 600  $\mu\text{m}$ ) formed the pictured twisted yarn, 3.2  $\mu\text{m}$  in diameter (Figure 6.13a). The MWNTs,  $\sim 10$  nm in diameter with length 10 000 times their width, form small bundles of a few nanotubes each in the forest, with individual nanotubes moving in and out of different bundles.

The investigated fibres had a typical four-probe resistivity of 3.3  $\text{m}\Omega\text{cm}$ . Mechanical tests were done on the twisted yarns as singles (Figure 6.13a), and two- or four-ply (Figure 6.13b) fibres. The untwisted yarns were so weak that they broke when pulled away from surfaces that they accidentally contacted, whereas the singles yarns had measured tensile strengths between 150 and 300 MPa. Higher strengths, between 250 and 460 MPa, were observed for two-ply yarns. Infiltration with PVA increased the observed strengths of singles yarns to 850 MPa. A hysteretic stress-strain curve was observed when the fibres were subjected to load-unload cycles. Although the mechanical strength is improved by twisting, the effective Young's modulus of the yarns is still limited by the low intertube coupling, ranging from 5 to 30 GPa.

### 6.2.2 Conclusion

We have seen that there are several methods to produce macroscopic structures of aligned CNTs. Films, ribbons and fibres have been realised. Anisotropic electrical, thermal and optical properties were measured and correlated with the degree of alignment of nanotubes. The Young's modulus increases with the degree of orientation of nanotubes, with the best being around 100 GPa. Unfortunately, this value is still very far from the value obtained for SWNTs and good quality MWNTs, 1 TPa. The reason for this is the weak coupling between the CNTs in the fiber. Further improvement, to approach the properties of individual tubes, could be achieved by improving the tube-tube contacts.

## 6.3 Irradiation and reinforcement of ropes of CNTs

The solution to the problem of shearing is to introduce links between the tubes. In the ideal case these links should be pure covalent carbon-carbon bonds, because of their high strength. It has been known that irradiation has a very strong effect on the out of plane strength of graphite. Thus, in what follows, we will give a summary of irradiation effects on graphite, nanotubes and other carbon structures. We will also show the results of Kis et al. concerning electron irradiation of SWNT ropes [13].

### 6.3.1 Irradiation effects on carbon nanostructures

There are several ways an energetic charged particle (such as an accelerated electron) can transfer energy to the target. These interactions can be divided into two major categories:

1. Knock-on effects – leading to:
  - atomic displacements in the interior,
  - atomic displacements on the surface (sputtering).
2. Excitations:
  - collective electronic excitations (plasmons),
  - localised electronic excitation or even ionisation of atoms,
  - vibrational excitations – phonons (heating),
  - bond breaking and/or cross-linking,
  - secondary emission of photons – visible light or X-rays,



- secondary emission of Auger electrons.

The cross-sections of these processes vary differently as a function of the incoming particle energy and strongly depend on the target's local structure and electronic properties. In general, with increasing particle energy, excitations decrease in importance, while knock-on effects increase. Excitations are substantial in insulators where ionisation can play the dominant role. On the other hand, ionisation is strongly suppressed in metals due to conduction electrons that can screen and neutralise ions on the timescale of 1 fs. Radiation damage in metals – and in carbon nanotubes – are therefore limited to knock-on displacements [64].

### 6.3.2 Irradiation effects on graphite

In irradiated graphite, a generally complex defect population evolves over many different length scales. Macroscopic measurements on particle irradiated graphite revealed several irradiation effects: large strains (growth parallel to c-axis and contraction within the basal planes), increased thermal and c-axis electrical conductivity. These are largely results of lattice disorder and structural damage associated with irradiation and depend on irradiation temperature, flux, dose and type of source [132, 133].

Atoms knocked out from the graphite lattice by projectile particles produce interstitial and vacancy defects. Telling et al. [133] studied the structures of defects and involved processes by simulations using density functional theory. Calculations pointed out that a number of defect species form strong covalent bridges between the atomic layers. Because of the large anisotropy of the graphitic lattice, displacement within the basal planes is difficult while displacement into channels between them is facilitated, with several stable interstitial positions (Figure 6.14). Free interstitials have been assumed to have a migration energy of 0.1 eV or below, making them mobile even at room temperature. Two or more mobile interstitials can combine and form a less mobile cluster. This agglomerate can then act as a seed, to which other atoms could bind. Further aggregation pushes the adjacent planes apart and eventually leads to the formation of a new lattice plane, which is accompanied with macroscopically observed swelling of graphite.

Theoretical modeling demonstrated that two of the atoms surrounding a vacancy form a weak bond and displace the third neighbour out of the graphitic layer by about  $0.7\text{\AA}$  [133], see Figure 6.14. This vertical displacement confers a greater tendency for inter-plane interactions around vacancies. Moreover, two interplanar vacancies can be formed in perfect AB-stacking neighbouring graphene sheets in order to join into a metastable divacancy. The participating vacancies are both

of the  $\beta$ -type (ring centre above and below vacant lattice site). The first nearest interplane neighbour divacancy  $V_2^1(\beta\beta)$  with a bridging bond of  $1.43\text{\AA}$  in length is more stable than two isolated vacancies. The second-nearest interplanar neighbour divacancy  $V_2^2(\beta\beta)$  is stabilised with a slightly shorter bridging bond of  $1.38\text{\AA}$  (Figure 6.14). The shared bond is less twisted in this symmetric geometry, allowing a double bond to form. For comparison, the  $\text{sp}^3$  bond is only  $1.57\text{\AA}$  long, while the  $\text{sp}^2$  bond is  $1.42\text{\AA}$  long. Consequently, interstitials can also form cross-links between graphitic layers.

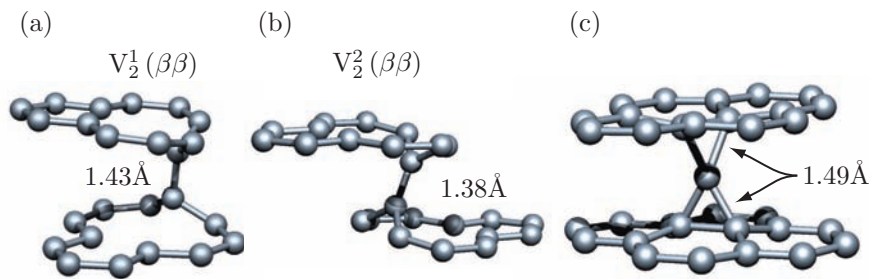


Figure 6.14: Two possible types of cross-link (a) and (b) promoting divacancies in graphite, from the paper of Telling et al.  $V_2^1(\beta\beta)$  and  $V_2^2(\beta\beta)$  the first and the second nearest interplane-neighbour divacancy configurations allow bonding between the twofold coordinated carbon atoms. Corresponding bond lengths are  $1.43\text{\AA}$  and  $1.38\text{\AA}$ . The fourfold coordinated interstitial (c) (bond lengths are  $1.49\text{\AA}$  each), that can occur when the basal planes are shifted by half a bond length ( $0.71\text{\AA}$ ) from their equilibrium configuration [133].

In addition to the configurations given in Figure 6.14, a range of other topological possibilities exist for interplanar divacancies in sheared graphite structures or in multiwall nanotubes. Such a basal shearing can occur when interstitial atoms are attracted to existing basal dislocation, which exist in high densities in most types of graphite with a shift of exactly  $0.71\text{\AA}$ .

There are therefore two possible ways of connecting atomic planes within graphite: one is involving two vacancies on opposite sides and the other is with an interstitial atom, acting as a bridge. Cross-linked defects of this kind will play an important role in explaining the occurrence of nanotube cross-linkings.

### 6.3.3 Irradiation effects on carbon nanotubes

In the first years following the discovery of CNTs, most of the research was limited to structural studies using TEM. Very soon, it was discovered that prolonged exposure of carbon nanotubes to the electron beam can lead to irreversible shape changes.

Ajayan et al. [134] and Kiang et al. [135] have shown that nanotubes develop ripples and eventually break under intense irradiation.

In TEM, CNTs are exposed to knock-on collisions of energetic electrons which can break the carbon-carbon bonds. The value of the threshold energy strongly depends on the direction of the incoming electrons. Obviously, the smallest value is expected for the radial displacement in the direction perpendicular to the nanotube's surface, and highest for in-plane displacements. According to tight-binding molecular dynamics simulations, the threshold energy of ejection can vary from 17 eV up to 43.5 eV, for directions normal and parallel to the nanotube's surface [136]. This means that ballistic displacements perpendicular to the tube's surface are possible with electrons above the threshold kinetic energy of 86 keV [137].

Irradiation on CNTs has been shown to provoke structural changes like shrinking, breaking [138], collapse into ribbons [136], amorphisation [139, 13], coalescence [140] or junction formation [141]. The fate of nanotubes under irradiation is determined by particle energy, flux and the temperature at which the nanotubes are maintained. Exposure of isolated single-walled nanotubes under uniform irradiation conditions can lead to atom removal from the nanotubes [138]. Atom loss creates vacancies which could further cluster into larger holes in the structure, and due to the dangling bonds associated with these defects, the system will become energetically unstable. Continuous atom removal from the surface of a nanotube could hence either leave a highly unstable nanotube structure of the original diameter or could shrink by mending these holes through atomic rearrangements which should necessarily be constrained to the monoatomic layer. In Figure 6.15 the images illustrate an irradiation sequence of a SWNT. Under uniform electron irradiation the tube shrank from the initial diameter of 1.4 nm down to 0.4 nm before breaking.

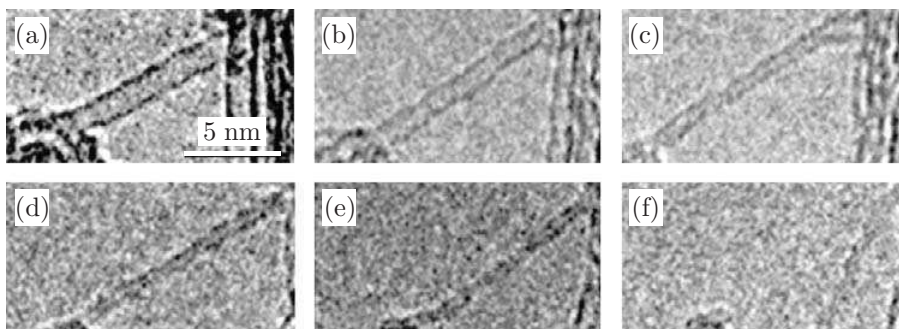


Figure 6.15: An isolated SWNT exposed to a low-intensity  $1 \left( \frac{\text{\AA}}{\text{cm}^2} \right)$  200 keV electron beam. Atom extraction from the surface leads to a series of surface reconstructions in which the nanotube diameter decreases from the original value of 1.4 nm (a) to 0.4 nm (f) before eventually breaking [138] after half an hour of irradiation.

Irradiation damages in MWNTs appear as collapsing, indicating a mechanical weakening of their structure. If the irradiation damage is anisotropic, damaged portions of the tube weaken, so that the elastic energy cost of flattening a tube is smaller than the gain in cohesive energy. Crespi et al. [136] provoked MWNTs to collapse using electron with energies of 800 keV and fluxes of  $2 \times 10^{19} \frac{\text{electron}}{\text{cm}^2\text{s}}$ . Due to the anisotropy of the threshold energy, atom extraction and weakening proceeds faster in regions perpendicular to incoming electrons. This provokes gradual flattening which was registered on the same MWNT irradiated with 800 keV electrons after 10, 70 and 100 seconds, respectively. Essentially the same effect can be reproduced when irradiating the tubes with a 200 keV electrons and an order of magnitude lower flux of  $2.5 \times 10^{18} \frac{\text{electron}}{\text{cm}^2\text{s}}$  [142]. The beam energy therefore doesn't seem to play a crucial role, as long as it's above the threshold value. Threshold energy for radial displacements have been calculated about 15 eV, which corresponds to a threshold electron accelerating voltage of 76.8 keV.

Electron irradiation not only shrinks the tubes but it can also coalesce [140] or link CNTs together [141]. When SWNTs are assembled into bundles – which is the case in general – coalescence is energetically more favourable because it minimises the strain energy, so that the process goes in the direction of diameter increase. Terrores et al. [140] showed coalescence of SWNTs under 1.25 MeV electron beams at 800°C under beam intensity of  $20 \frac{\text{A}}{\text{cm}^2}$ , Figure 6.16. During irradiation, highly mobile interstitial carbon atoms were created, due to annealing of vacancy-interstitial pairs. Vacancies induced coalescence via a zipper-like mechanism, imposing a continuous reorganisation of atoms on individual tube lattices along adjacent tubes.

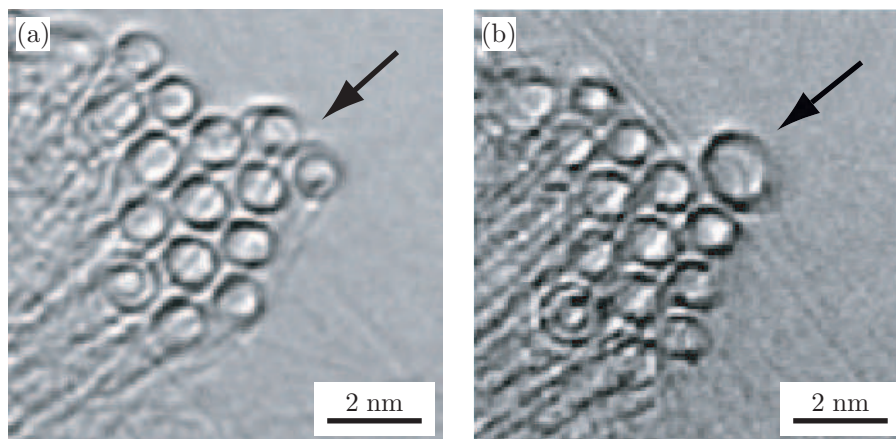


Figure 6.16: (a) HRTEM image of a nanotube bundle before and (b) after a couple of seconds under a high-intensity 1.25 MeV electron beam [140].

Coalescence is an avalanche process; initially, two tubes coalesce rapidly into a larger cylinder of two times the circumference. Subsequently, this coalesced tube establishes a link with a neighbouring tube of a smaller diameter. After a while, this bridge develops into a dumb-bell-like configuration. This kind of process was frequently observed on the edge of the bundle, probably because the coalescence requires free space.

Junctions consisting of a pair of crossed individual SWNTs have been reported by also Terrones et al. [141]. Nanotubes were linked to “X”, “Y” and “T” junctions. However, the tubes in junctions appear defective and electrical characterisation of these structures will be needed in order to assess their potential usefulness and the extent to which irradiation induced damage influences the tube’s electronic properties.

Mechanical measurements of carbon nanotubes as a function of electron irradiation was performed by Kis et al. [13]. This experiment represented a measurement of  $E_{\text{bending}}$  on bundles of SWNTs under irradiation.

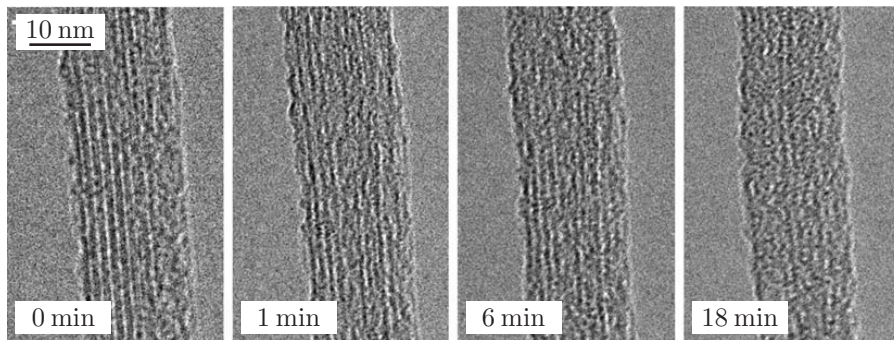


Figure 6.17: Evolution of the morphology of a carbon nanotube rope under intense electron beam irradiation. The acceleration voltage was 80 kV and the current density  $0.4 \frac{\text{A}}{\text{cm}^2}$ . Corresponding doses are:  $3.4 \times 10^{20}$ ,  $17 \times 10^{20}$  and  $67 \times 10^{20} \frac{\text{electron}}{\text{cm}^2}$  [13].

Irradiation was done at both 200 keV and 80 keV. TEM pictures showed the appearance of cross-linking between neighbouring nanotubes in the rope before amorphisation. In the 80 keV case,  $E_{\text{bending}}$  reached 750 GPa, which is 70% of the Young’s modulus value of an isolated nanotube.

Radiation experiments have illustrated that irradiation is not always a destructive process, but that it can also be exploited as a cure for one of the most serious flaws of carbon nanotubes, the weak intertube interaction.

## 6.4 Sample preparation

As was described in Chapter 5, even at laboratory scale CNTs can be produced at the rate of 1kg per day, allowing experiments on assembly of macroscopic fibres. In order to study the possibilities of reinforcing CNT fibres, first we used different alignment techniques to make them. Methods were first characterised by commercially available SWNTs and then we modified them in order to use our CCVD grown MWNTs.

### 6.4.1 Electrophoresis

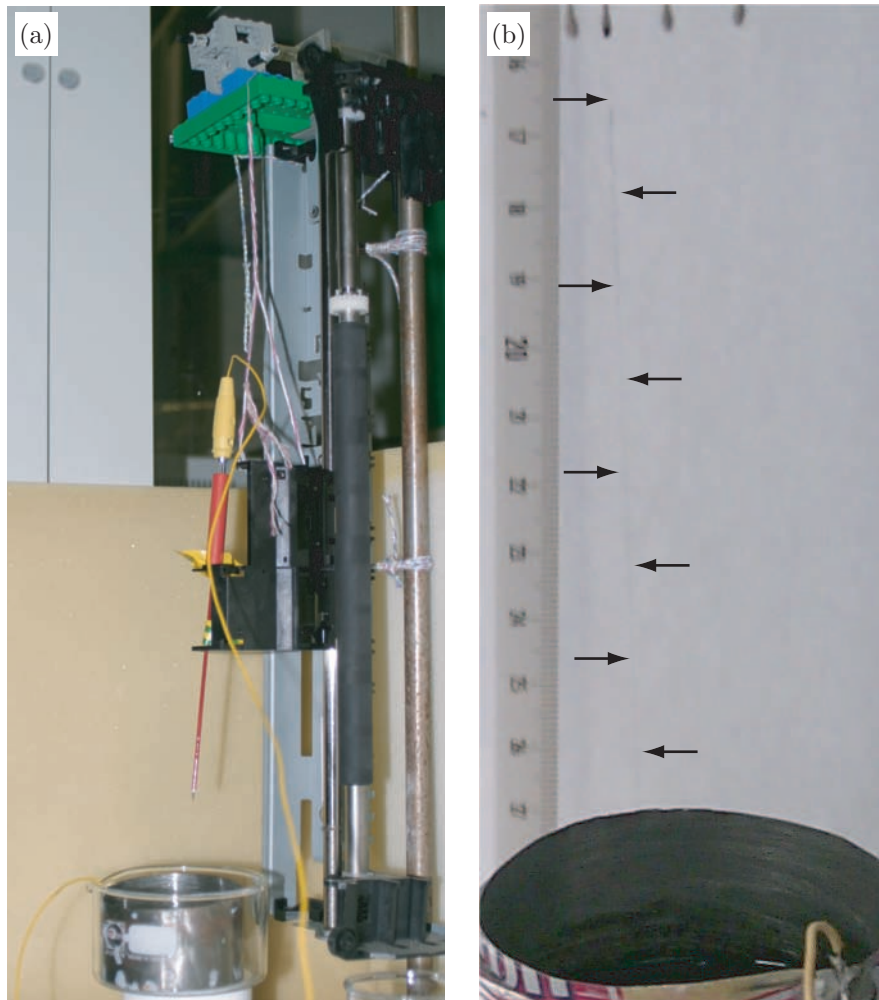


Figure 6.18: (a) The motor driven translational stage with the negative electrode around the 1 wt% of SWNT/DMF suspension and four positively charged graphite electrodes immersed into the suspension. (b) After six hours of pulling, long fibres appear on the electrodes.

The first method we tried was the one developed by Gommans et al. [118], as described earlier. Some drawbacks of this method are sensibility to the stability and purity of the suspension as well as to external vibrations. Figure 6.18 presents the realisation of the electrophoresis alignment. By improved the stability of the system, we obtained several cm long fibres with diameters ranging from 2 to 50  $\mu\text{m}$ . Figure 6.19 shows a SWNT fibre obtained by the electrophoresis method.

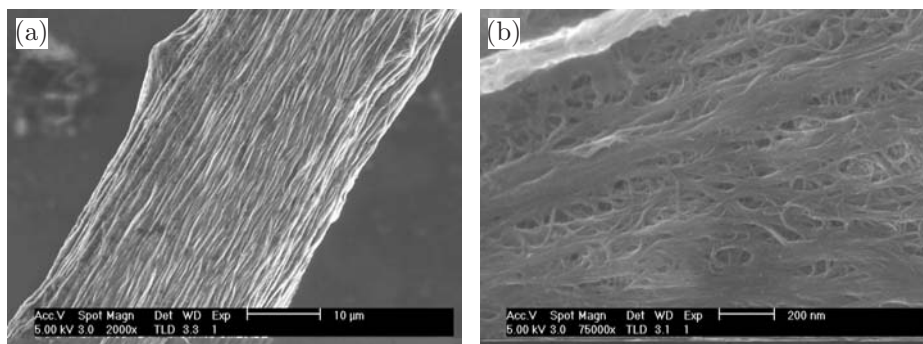


Figure 6.19: SWNT rope, (a) small magnification and (b) high resolution scanning electron micrograph.

We also found that the use of the solution of PmPV (poly- (m-phenylene vinylene-co-2,5-dioctoxy-p-phenylene)) in toluene instead of the solvent DMF improved the pulling procedure of CNT fibres; it was more stable and variable. Using DMF, only SWNT fibres could be successfully pulled whereas using PmPV also fibres consisting of MWNTs could be obtained, see Figure 6.20. MWNTs are in general more difficult to assemble since they form much less stable liquid suspensions and hardly assemble into bundles.

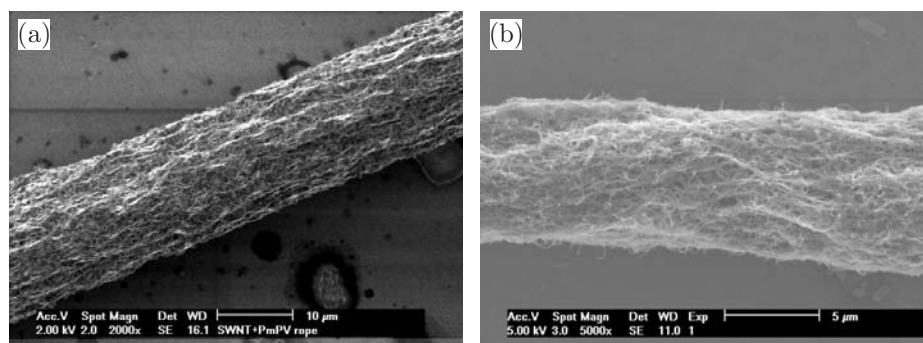


Figure 6.20: Scanning electron micrograph of SWNT (a) and MWNT (b) rope using PmPV/toluene solution.

## 6.4.2 Extrusion

Flow alignment [108] seemed to be a promising method because of its aptitude to scale up [11]. We could produce SWNT fibres with this technique but it was impossible to apply the method to MWNTs since the MWNTs do not easily form bundles.

Other groups have already made successful trials to obtain single- and multiwall CNT composite fibres by spinning [10, 121, 143] as shown in Figure 6.9b. In order to characterise the process a micro-extruder was used. Before the micro-extrusion, CNTs were dispersed in a liquid solution of the precursor of polypropylene and later on mixed with polypropylene by prolonged sonication. The polymer-MWNT mixture was dried and pelletized. These were extruded at 220°C (Figure 6.21). Fibres from 0.5 wt% to 10 wt% of MWNT concentrations were successfully made, while no coagulations were observed above 20 wt% of MWNTs.

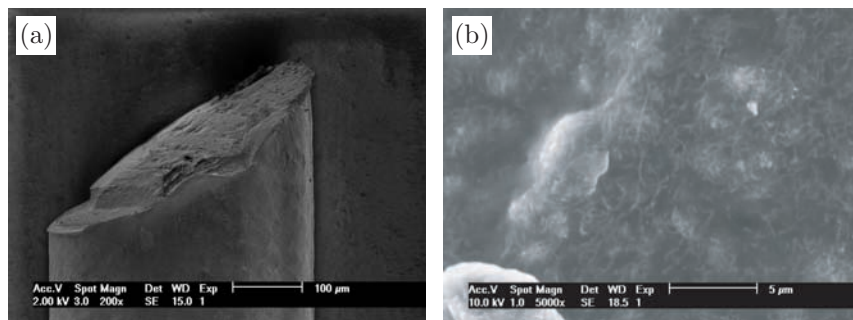


Figure 6.21: Scanning electron micrograph of MWNT/polypropylene fibre smaller (a) and higher (b) magnification.

## 6.5 Experimental results on as-prepared samples

### 6.5.1 Mechanical measurements

The measurement of the Young's modulus of the SWNT fibre, made by the electrophoresis or fibre spinning methods, is based on the measurement of the resonant frequency in a displacement excitation system [144]. In this method a fibre-mass system is excited into vertical oscillations by a shaker, whereby the specimen acts as a spring element rigidly suspended at one end and loaded by a mass glued to the other, see Figure 6.22. This configuration enables a non-destructive elasticity measurement of the CNT fibre. Since it is not torn apart, there is a possibility to do in-situ measurements during polymerisation, for instance. In the case of a homogeneous fibre this measurement gives the Young's modulus.



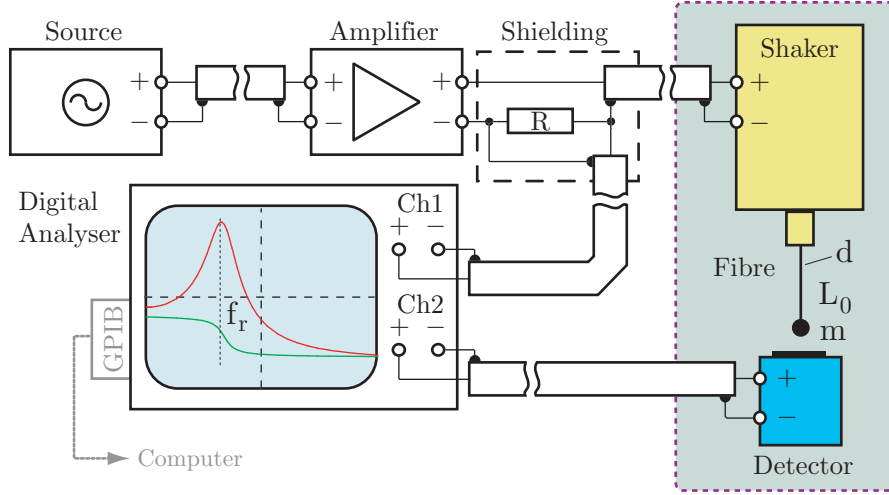


Figure 6.22: Schematic drawing of the non-destructive elastic modulus measurement. The fiber is shaken by an amplified random noise signal. The digital signal analyser compares the signal from the amplifier and the response of the fiber.

In the experiments, specimens of 10-15 mm length were cut from a long rope and suspended on a loudspeaker membrane (type: Bruel-Kjaer) at one end, and a ferromagnetic ball was glued to the other end. This was hung above a transducer (detector), which detected the displacement of the ferromagnetic ball. The fibre was shaken with a random noise signal, which was measured together with the sample response by a two channel HP Digital Signal Analyser. This allowed calculation of the sample's frequency response curve. The method is described in detail in Appendix B. The measurement of phase together with the amplitude allows the unambiguous identification of resonances: if a peak at a certain frequency is accompanied by a phase turn, then this frequency is a resonant frequency of the fiber. Figure 6.23 is a typically observed frequency response.

In vibration, the fibre periodically stretches and returns to its original length. This small variation in length is detected by the response of the system during excitation and used for calculation of the Young's modulus of the fibre [144]. In the linear region, the relation between Young's modulus ( $E$ ) and the frequency response ( $f$ ) is as follows:

$$E = 4\pi^2 \frac{f^2 l_0 m}{A}, \quad (6.6)$$

where  $l_0$ ,  $A$  and  $m$  denote the initial length and cross-section of the fibre, and the mass of the load, respectively [144, 145].

This expression is valid for a homogeneous, uniform fibre. One has to keep in mind that the macroscopic fibres consist of loosely connected ropes of SWNTs, and

within the rope the nanotubes interact with weak van der Waals forces. Therefore, in such a “mosaic” system the frequency response of the fibre to a periodic elongation corresponds to the shear modulus  $G$  between the nanotubes within the fibre, rather than to the elongation of the nanotubes themselves. The measured number is a mean value which is characteristic for the intertube interactions.

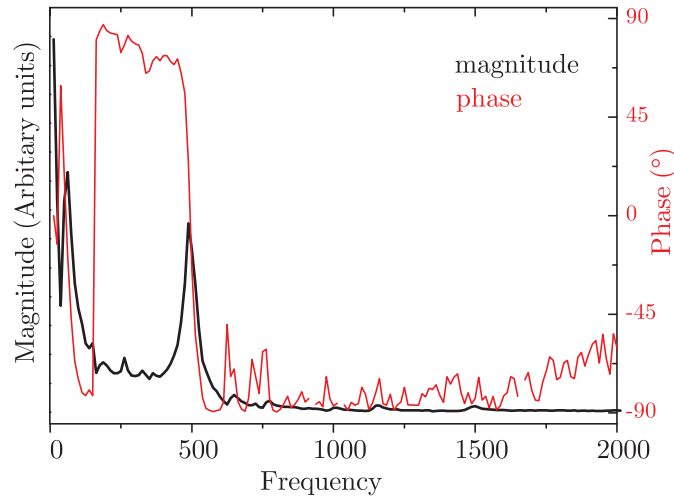


Figure 6.23: Frequency response curve of a carbon nanotube rope. The peak at 50 Hz is line pick-up. The peak at 487.5 Hz corresponding to the resonant frequency of the fibre, which accords with the value 5.3 GPa based on equation (6.6).

| Fibre           | Young's modulus (GPa) |
|-----------------|-----------------------|
| SWNT            | 5.3                   |
| SWNT+PmPV       | 42.5                  |
| PP              | 0.9                   |
| PP+MWNTs (0.5%) | 2.2                   |
| PP+MWNTs (4%)   | 1.9                   |
| PP+MWNTs (6%)   | 1.0                   |
| PP+MWNTs (8%)   | 0.8                   |
| PP+MWNTs (10%)  | 0.7                   |

Table 6.1: Young's moduli of fibres made by electrophoresis and spinning methods.

Table 6.1 summarises the results of the Young's modulus measurements on the ropes and composite fibres. For PP/MWNT fibres, the Young's modulus depended on the concentration of the nanotubes. In the case of 0.5 wt% of SWNT containing fibres reinforcement has been observed in contrast to the 10 wt% of nanotube

concentration, where the tubes weakened the fibre.

### 6.5.2 Four-probe measurements on the ropes of SWNTs

We have seen that in the case of graphite the increase of conductivity in the perpendicular direction was a telltale sign of crosslinking due to radiation damage. We also see that in order to increase the strength of CNT fibres the tubes must be interlinked. This will certainly have an effect on the resistivity, thus we performed resistivity measurements on the fibres we made.

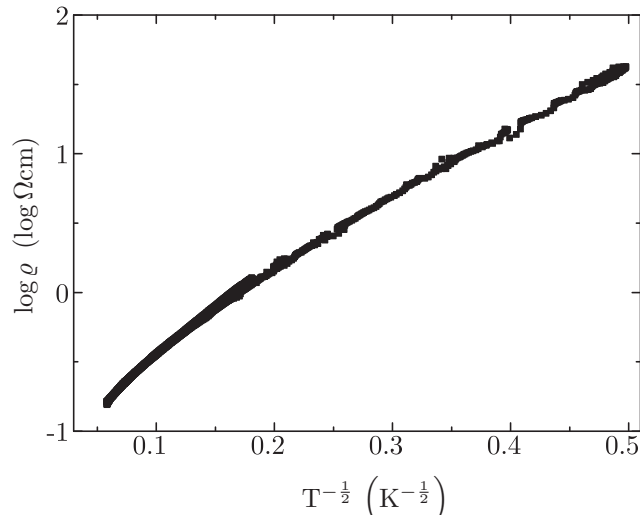


Figure 6.24: Temperature dependence of the electrical resistivity of the SWNT fibre. The resistivity of SWNT fibre as a function of temperature indicating hopping-like conduction [146].

Resistivity measurements were done on 3 to 5 mm long sections of electrophoretically grown SWNT fibres. These were placed on a mica support, and contacted by four gold electrodes glued by conducting silver paint under an optical microscope. The average room temperature resistivity of the fibres was  $0.2 \pm 0.08 \Omega\text{cm}$ . Temperature dependence was measured in a He cooled cryostat, Figure 6.24 shows the result. It shows that the logarithm of the resistivity increases linearly with  $T^{-\frac{1}{2}}$ :

$$\rho \propto e^{\left(\frac{\tau_0}{T}\right)^{\frac{1}{2}}}, \quad (6.7)$$

This indicates Coulomb-repulsion limited hopping conduction, as in many granular carbon materials [147, 148]. The value of the resistivity is 3-4 orders of magnitude higher than the resistivity of individual tubes, see Subsection 6.1.4). This indicates that the conduction is limited by the intertube connection.

Although SWNTs can be either semiconductors or metals, the conductivity of macroscopic samples always shows semiconducting properties. The reason for this is that the individual nanotubes are much shorter than the distance between two electrical contacts on a fibre, thus electrons must hop from one nanotube to the other, and it is this that limits conductivity. Doping or simply linking the nanotubes is expected to reduce resistivity.

## 6.6 Cross-linking CNT fibres by e-beam: a resistivity study

Previously, it has been shown by AFM measurement that nanotubes in a rope can be linked to each other by a low dose of electron irradiation, enhancing the shear modulus [13]. In order to study this effect on macroscopic SWNT fibres, we measured the electrical resistivity *in situ* inside a TEM.

SWNT fibers made by the electrophoretic method [118] – detailed in this chapter on page 69 – were irradiated by 200 keV energy electrons. In order to investigate the influence of electron irradiation on the electrical conductivity, a TEM specimen holder with four electrical contacts was employed, see Figure 6.25. This configuration enabled the *in situ* measurement of the electrical resistivity during electron irradiation in a TEM. The SWNT fiber with four electrical contacts was mounted on a TEM ring, insulated by a thin mica layer.

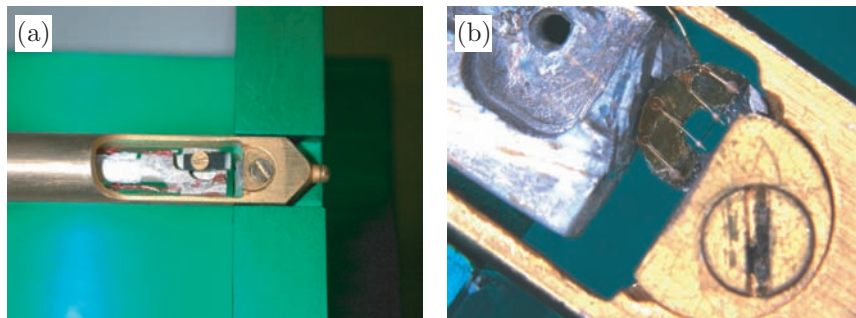


Figure 6.25: (a) TEM specimen holder with electrical contacts. (b) A SWNT fiber is mounted on a TEM ring (in the middle) which is placed and contacted to the specimen holder.

For electron irradiation a Hitachi TM 700 microscope was used operating at 200 kV. In order to expose uniformly the fiber between the two inert contacts to electrons at the start of the irradiation the electron beam was defocused onto a 470  $\mu\text{m}$  diameter circle. The homogeneous irradiation was then carried out for

approximately 29 hours at a constant electron flux of about  $2.43 \times 10^{13} \frac{\text{electron}}{\text{cm}^2\text{s}}$ . In order to avoid prohibitively long exposure time, in the second part of the experiment the incident beam was focused to a diameter of  $15 \mu\text{m}$ , increasing the flux to  $23 \times 10^{16} \frac{\text{electron}}{\text{cm}^2\text{s}}$ , and this spot was moved step by step along the fiber between the two central electric contacts.

Figure 6.26 shows the resistivity of a SWNT fiber as a function of irradiation time. At the beginning, the ropes had a typical four-probe resistivity of  $0.2 \pm 0.08 \Omega\text{cm}$ , which is in agreement with the results of Vigolo et al. [108]. Upon irradiation – with a flux of about  $2.43 \times 10^{13} \frac{\text{electron}}{\text{cm}^2\text{s}}$  –, the resistivity dropped approximately to one-third of the initial value and reached a minimum after about 35 min. Past this minimum, the resistance increased linearly with the irradiation time with a slope of about  $1.15 \frac{\Omega}{\text{min}}$ . This dependence remained the same for many hours. In order to study the effect of some more important radiation damage, the beam was focused to a  $15 \mu\text{m}$  diameter spot to get a flux of  $23 \times 10^{16} \frac{\text{electron}}{\text{cm}^2\text{s}}$ . We irradiated each spot until the resistivity saturated, then moved the beam to a neighbouring section along the fiber axis – this gives rise to the step-like time dependence shown in Figure 6.26.

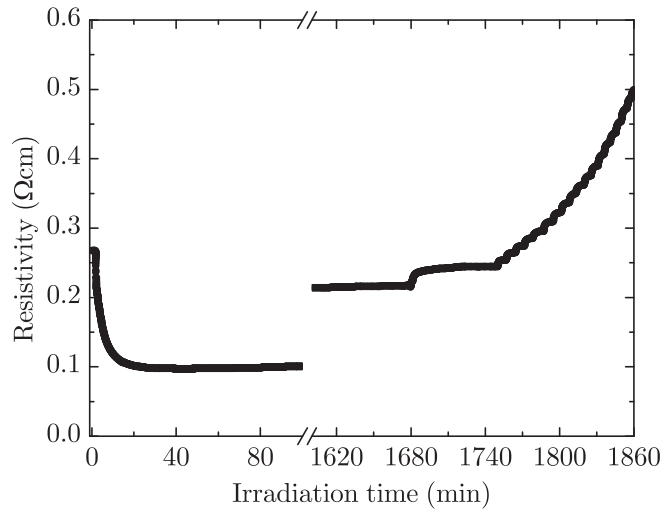


Figure 6.26: The resistivity of a SWNT fiber as a function of electron irradiation time. After 35 minutes of electron irradiation, the fibre reached the minimum of resistivity. The step-like variation towards the end of the irradiation is the result of the stepwise moving of the irradiated zone along the sample.

Besides measuring the resistivity during irradiation, the  $\rho$  vs  $T$  was also measured at three stages of the irradiation:

1. before the irradiation,
2. at the minimum resistivity point and
3. after the full irradiation.

Figure 6.27 presents these three curves in log scale in their ordinate values. As can be seen, except for the magnitude of the resistivity, there is not much change in the behaviour. All of them are semiconducting with an exponential temperature dependence of the resistivity, which is well described by:

$$\rho \propto e^{\left(\frac{T_0}{T}\right)^{\frac{1}{2}}} \quad (6.8)$$

This indicates Coulomb-repulsion limited hopping conduction as we have seen earlier [147]. The slope of the curve for the most irradiated sample is much higher, and the curve is more linear. This presumably reflects the higher degree of homogeneity of the completely amorphized sample.

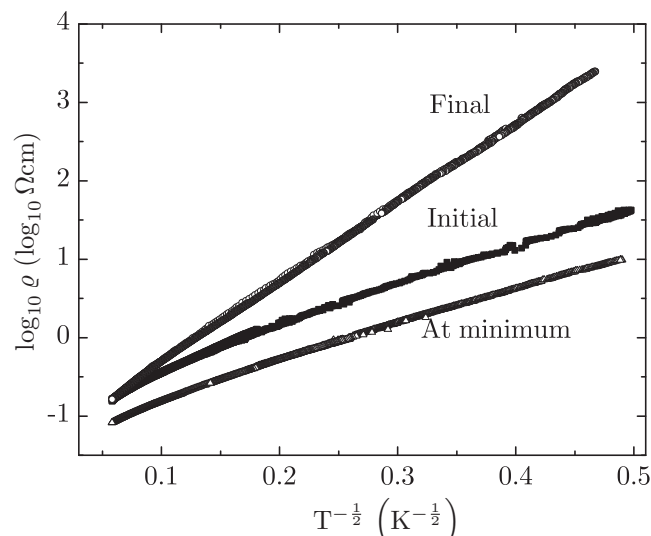


Figure 6.27: The resistivity of pristine and irradiated nanotubes as a function of temperature. The temperature dependence indicates hopping-like conduction.

With the aim of determining the interaction between the electron beam and the rope microstructure, TEM was carried out in the initial and final states. In order to keep the irradiation damage during observation to a minimum, the observation time at the same sample location was limited to below 1 min, and TEM images were taken within a couple of seconds. The TEM micrograph in Figure 6.28a shows

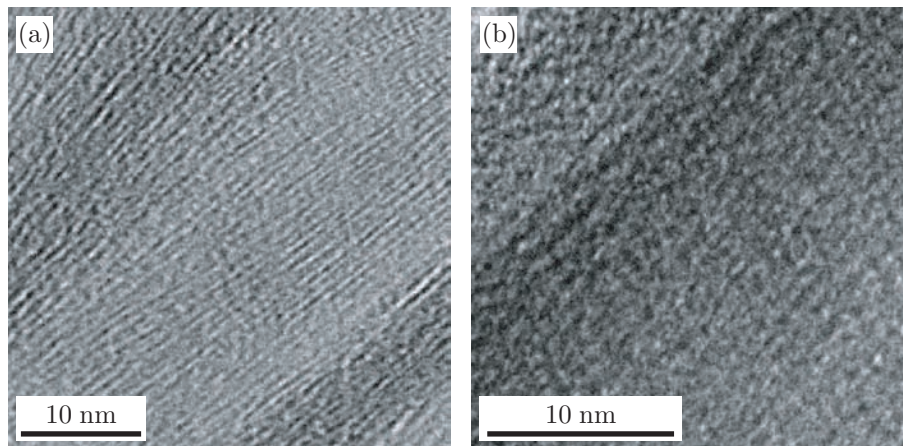


Figure 6.28: TEM images of the rope before (a) and after (b) the irradiation experiment. Before irradiation, the CNT wall structure of parallel layers of graphene sheets is clearly visible. After irradiation the wall structure is fully destroyed.

clearly the wall structure of SWNTs, which are visible as fringes with about 1.5 nm spacing. These fringes disappeared after irradiation, leaving behind an amorphous-like disordered structure, as in Figure 6.28b.

The results of the electrical measurements can be explained as follows. The electron irradiation creates displacements of the carbon atoms in nanotubes, leading to very reactive broken chemical bonds. These bonds can quickly relax with other dangling bonds on the surface of other nanotubes due to the chemical purification and/or previous radiation damages. This has a twofold effect on the resistivity: one process is the cross-linking of nanotubes in a bundle, improving the electric conductivity (Figure 6.26 at the start). This is not necessarily due to conduction across the covalent bonds, it may simply be due to steric effect, i.e. the decreased tube-tube distance as a result of covalent bonding at some sites. The other effect, however, is the disruption of the graphite layer by these point defects, increasing the resistivity with increasing concentration (Figure 6.26 after reaching the minimum resistivity). This increase is linear at the beginning, but becomes saturated when the system is completely transformed into amorphous carbon and further irradiation no longer increases the disorder. For low damage level, the first process dominates since the creation of covalent bonds between two nanotubes represents a tremendous improvement in the intertube conductivity while the same few point defects have little effect on the on-tube conduction. With increasing defect concentration the second effect starts to dominate.

## 6.7 Enhancement of the macroscopic fibre by ultraviolet light

As could be seen in the previous section, a gentle dose of electron irradiation can enhance the interconnectivity in SWNT fibres. However, a high electron dose leads to deterioration and finally to amorphisation of the CNT wall structure resulting in a significant loss of both mechanical strength [13] and electric conductivity [146]. Therefore an alternative non-destructive way is desirable to strengthen the fibers.

### 6.7.1 Interlinking SWNTs by UV light

It is well established that exposure of materials to UV light can give rise to various photo-induced phenomena, one of which is photo-induced polymerisation [149]. The group of prof. Rao has already reported that UV light acts as an oxidation accelerator of CNTs, both in theory [150] and in experiments [151].

Savage et al. [151] performed thermoelectric power measurement at room-temperature as a function of the UV irradiation time, and a significant change was observed from its initial value. Their results suggest that UV light accelerates the oxygen absorption by CNTs and this leads to a change in the thermoelectric power (since oxygen acts as a dopant).

Density functional theory calculation showed that the results of Savage et al. can be related to UV-light excitation of oxygen molecules from their ground spin-triplet state into a higher-energy spin-singlet state. Such excitation lowers the activation energy for molecular-oxygen chemisorption to a nanotube, increases the adsorption energy and promotes charge transfer from the nanotube to the oxygen molecule. Lattice defects such as 7-5-5-7 and Stone-Wales defects are found to play a critical role in enhancing oxygen molecule/nanotube bonding and in affecting the extent of charge transfer. Compared to this, the effects of nanotube diameter and chirality and the number of walls appear to be less significant [150].

Dimethyl-formamide (DMF) is known to be ultraviolet (UV) active in the presence of free radicals [152, 153, 154]. Thus, macroscopic ropes of CNTs prepared from a suspension of acid-treated SWNTs in DMF by electrophoresis and illuminated by UV light was thought to be a valuable experiment for non-destructive reinforcement of the fiber.

### 6.7.2 In-situ resistivity measurements on the SWNT fibres

In the UV irradiation experiment the samples were prepared exactly as for electron irradiation. For homogeneous irradiation, a UV spot light source (Hamamatsu



Lightningcure<sup>TM</sup> LC5) was used, operating at  $3500 \text{ mW/cm}^2$  ( $\lambda = 365 \text{ nm}$ ). In order to keep the temperature constant ( $19^\circ\text{C}$ ) and to avoid that changing temperature falsifies the result, the rope was cooled by a Peltier refrigerator.

Figure 6.29 shows the the electrical resistivity obtained in a four-probe configuration of the SWNT fiber as a function of UV irradiation time. At the starting point the average resistivity of the fibers was  $0.2 \pm 0.08 \text{ }\Omega\text{cm}$ .<sup>4</sup> During the first two minutes of irradiation, the resistivity abruptly dropped to about  $15 \text{ m}\Omega\text{cm}$  and did not vary upon further irradiation. This drop corresponds to a reduction by approximately 90% of the original value and is four times stronger than the decrease observed during our electron irradiation experiment ( $60 \text{ m}\Omega\text{cm}$  in Figure 6.29a). Thus, UV irradiation is significantly more effective in improving the conductivity of the fiber than electron irradiation. In order to exclude that this behaviour originates from a heating effect caused by the UV lamp, the measurement was continued by switching the illumination off and on. As can be seen in Figure 6.29b, the effect is less than 1% and the strong resistivity change remains irreversible. Consequently, the observed change in resistivity has to be attributed to a permanent UV irradiation effect.

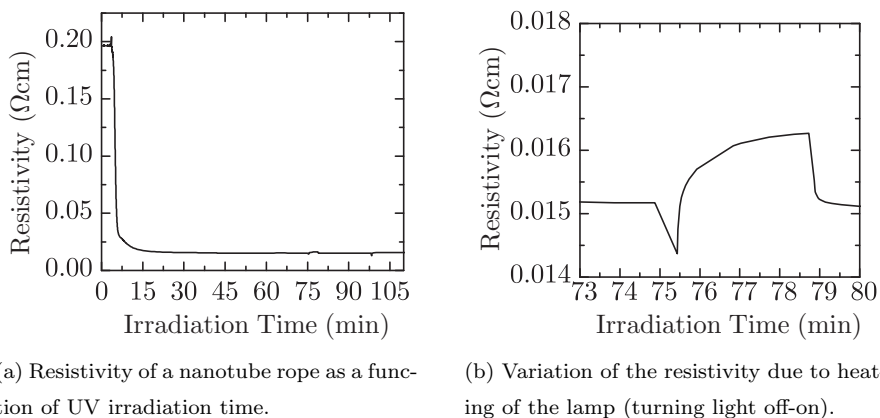


Figure 6.29: Four-probe electric measurement as a function of irradiation time.

### 6.7.3 Young's modulus measurements

In order to continue the examination of the interaction of the UV light and SWNT yarns, we also measured the Young's modulus at different stages of irradiation using the displacement excitation system [144].<sup>5</sup> This arrangement enables a non-destructive measurement of the CNT fiber with the possibility to access the effect

<sup>4</sup>As also measured in Section 6.6 on page 84.

<sup>5</sup>Detailed description is given in Subsection 6.5.1 on page 80 and in the Appendix B on page 107.

of the irradiation *in situ*. Figure 6.30 shows the UV illumination of the fibre during Young's modulus measurement. (The schematic drawing is in Figure 6.22.)

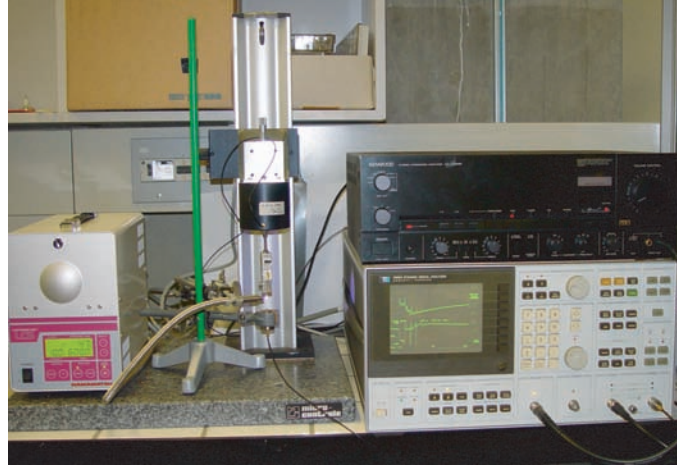


Figure 6.30: *In situ* Young's modulus measurement during UV illumination of the SWNT fibre. The UV lamp is on the left hand side, the SWNT fibre is attached to a loudspeaker and hanging on over a transducer. The frequency response is evaluated by a digital analyser (on the right hand side).

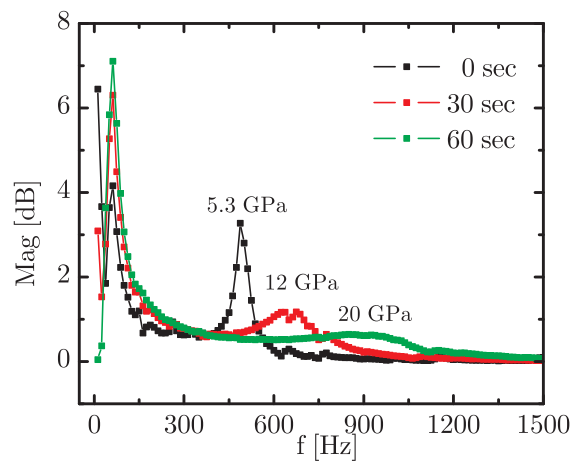


Figure 6.31: Frequency response curves of a carbon nanotube rope at different irradiation times. Note the shift of the resonance from 450 Hz to 950 Hz upon 60 seconds of ultraviolet irradiation. The peak at 50 Hz is line pick-up.

Samples were prepared as described earlier. UV irradiation time was varied between zero and two minutes. Figure 6.31 shows the amplitude of the frequency response obtained for the irradiation period of 0, 30 and 60 seconds.

As can be seen, a resonant peak appears for all three measurements, and the res-

onant frequency increases as the irradiation time increases. At the beginning of irradiation the average resonant frequency was 487 Hz, which corresponds to a modulus of  $5.3 \pm 0.5$  GPa. This value is in agreement with the shear modulus of SWNT ropes derived from the direct mechanical-property measurement by means of AFM [13]. After 60 seconds of irradiation the resonant frequency increased to 950 Hz, which corresponds in this case to a Young's modulus of  $20 \pm 0.5$  GPa. Hence, the irradiation causes a factor of four improvement.

Besides the shift of the resonance peak, its broadening is also observed which can be explained by the distribution of the intertube bindings and/or to the inhomogeneous penetration of the UV light. For example, the bonds close to the surface are more stiffened than the bonds in the middle of the fiber, whereas the measured modulus is averaged over the section of the fiber. Further illumination did not bring any more stiffening, similarly to the resistivity, which was also saturated after 1 minute of irradiation.

In order to investigate the structural changes caused by the irradiation, TEM was done. Figure 6.32 shows representative TEM images of the rope material before and after irradiation. The starting material exhibits aligned SWNTs with well-graphitised side walls, which appear in the Figure as lines with a spacing of 1.5 nm. After about one hour of exposure to UV light, these lines are still clearly visible, and no indication of amorphisation can be found.

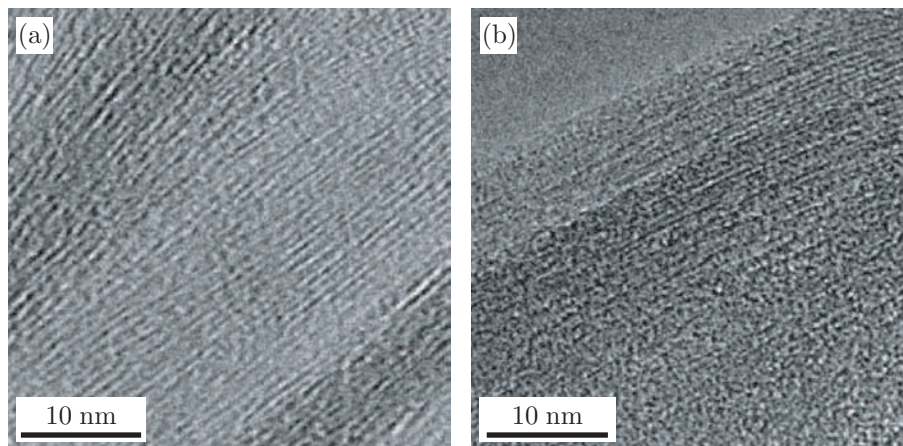


Figure 6.32: TEM image of a SWNT fiber before (a) and after UV irradiation (b). Note that there is no sign of amorphisation of the nanotubes.

In order to verify the effect of UV irradiation, two hours of continuous irradiation was carried out. There was neither shrinking nor amorphisation observed. This shows that the shift of the resonance peak was due to the strengthening of the fibre induced by ultraviolet light, gluing by photochemistry. In contrast to the electron

beam, where the ropes started to amorphise after 18 minutes of irradiation [13] (at 200 keV with a flux of  $1.35 \times 10^{19} \frac{\text{electron}}{\text{cm}^2\text{s}}$ ), UV irradiation does not destroy the graphitic side walls of SWNTs. This is a very important aspect for the reinforcement of carbon fibers, as the strength and the perfect graphitic structure go hand in hand.

The electrical and mechanical measurements show the sensitivity of CNT fibres to UV illumination but it is obvious that the ultraviolet light cannot kick out carbon atoms from the surface of nanotubes leaving dangling bonds behind. Hence, the graphitic structure of the tubes remains intact as testified by the TEM pictures in Figure 6.32 and, therefore, another mechanism has to take place. The SWNTs used in this study were subjected to harsh acid treatment during their purification, leaving their surface cluttered with free radicals. Fibers were pulled out from a suspension of SWNTs in DMF, which might be trapped in the fibers. It is plausible to suppose that under UV illumination the residual DMF together with the surface functional groups leads to the generation of chemical bonds between nanotube bundles.

Although a high degree of macroscopic alignment is deduced from the small magnification electron microscopy studies, at higher magnification the disorder appears. Hence, the nanotube bundles touch each other rather at points than along their whole length. In our opinion, DMF is likely to act around these contact points which are strengthened due to the UV illumination. Electronic excitation of the surface molecules by high energy photons relaxes in cross-linking, binds the tubes together, which increases the shear modulus of the fibers. This bridging structure is limited to the surface, has a distribution, giving rise to in the smearing of the resonance peak in Figure 6.31. These cross-linkings also facilitate the percolation of the electronic charge through the fiber, hence its resistivity decreases. However, these bindings are expected to be not as strong as in the case of electron irradiation for which in some cases (at 80 keV accelerating voltage) 75-fold shear modulus increases were observed [13] before amorphisation. On the other hand, the advantage of UV-light is, that the graphitic structure of the tubes remain intact as TEM pictures in Figure 6.32 have revealed, so reinforcement by ultraviolet light is a promising alternative compared to electron irradiation.

## 6.8 Conclusion

Assembly of carbon nanotubes into fibres has been a great challenge since the discovery of their excellent mechanical properties. In this chapter, different alignment methods were introduced together with measurement techniques of electrical and

mechanical properties.

Fibres consisting of singlewall and multiwall nanotubes were prepared in two different ways. Macroscopic measurements on these yarns have shown that the elastic properties are not even close to that of an individual nanotube. Increase of mechanical strength has been observed in CNT reinforced polymer fibres in the case of low concentration of nanotubes. A solution to the problem of the weak elastic properties would be to introduce links between the tubes or strengthen the load transfer between the tubes and the polymer matrix. In the ideal case these links should be pure covalent carbon-carbon bonds, because of their high strength.

Electrical measurements on the ropes of SWNTs pointed out the hopping-like conductance of the fibres. Consequently, resistivity can be a good indicator of the bond strength between tubes, since anything affecting this intertube bonding strength has a strong impact on the conductivity of the fibre.

Reinforcement of fibres consisting of single- or multiwall carbon nanotubes is a crucial problem since the “neat” fibres lack the strength of an individual tube. One of the evident solutions was the irradiation of nanotubes by different particles such as electrons or high energy photons in order to build cross-links between nanotube bundles. We presented two effective ways to strengthen the CNT fibres. It was found that not only the irradiation by electrons but ultraviolet light as well leads to covalent C-C bond formation of nanotubes in the fiber. Illumination of DMF treated fibres by UV light increases both the conductivity and the mechanical strength, which can be explained by the photo-chemistry between the free radicals on the surface of CNTs and DMF molecules. The fact that graphitic structures are not destroyed under UV and that the drop in resistivity is about four times stronger than with electron beam, makes UV irradiation more promising for reinforcement of CNT fibers. Since UV light is also applicable to larger surfaces, it opens the door to produce CNT based composites with high strength and conductivity in a large scale.



## Chapter 7

# General Conclusions

In this work, two related subjects have been investigated: (i) growth of carbon nanotubes by catalytic chemical vapour deposition of acetylene and (ii) assembly and reinforcement of macroscopic carbon nanotube fibres.

A systematic study of the growth of carbon nanotubes by chemical vapour deposition has been elaborated. In particular, the effect of catalyst composition, catalyst carrier and retention time on the yield and quality of CNTs was investigated. It was found that  $\text{Fe}_2\text{Co}$  is the most active catalyst in the bimetallic family of  $\text{Fe}_{1-\xi}\text{Co}_\xi$ , whereas enrichment in Co or Fe produces an extra phase, which lowers the catalytic activity for CNT production due to particle encapsulation. Furthermore, the  $\text{CaCO}_3$  support was found to be an additional source of carbon. The chemical reaction is the decomposition of  $\text{CaCO}_3$ , which produces  $\text{CO}_2$  groups that react with acetylene to result in carbon for the growth of CNTs.

Some reports [99] indicated the usefulness of oxygenated species in the reactor chamber during the growth, others [98] showed the influence of the support on the CNT production. Up to now, no clear understanding of the role played by the support itself or the oxygenated species have been presented.

In Chapter 5, we have shown a clear involvement of the support in the nanotube growth process by reaction of  $\text{C}_2\text{H}_2$  and  $\text{CO}_2$  species from the support. Possible growth processes were also presented depending on the growth conditions. Finally, the understanding of the effect of each growth parameter allowed a high yield production of nanotubes of the order of kilogram per day.

The second subject was to assemble CNTs into macroscopic fibers in order to exploit their extraordinary mechanical properties. In general, macroscopically aligned arrays of CNTs show an enhancement of the mechanical, electrical and thermal properties compared with the random tangles of bundled tubes typically found in

as-grown bulk samples [7, 8, 9, 10, 11].

Macroscopic fibers consisting of aligned SWNTs and MWNTs were prepared by two different ways: electrophoresis and extrusion. Although both semiconducting and metallic CNTs are present in the starting material, electrical measurements revealed semiconducting properties of the macroscopic fibres. The reason for this is that the individual nanotubes are much shorter than the distance between two electrical contacts on a fibre, thus electrons must hop from one nanotube to the other, and it is this that limits conductivity. Consequently, resistivity can be a good indicator of bond strength between tubes, since anything affecting this intertube bonding strength has a strong impact on the conductivity of the fibre.

From the mechanical point of view, ropes of SWNTs are weakly coupled to each other by van der Waals interaction [12]. Consequently, the mechanical strength of a macroscopic nanotube fiber is limited by the small intertube shear modulus: The fiber would be torn apart before the individual nanotubes would break. Macroscopic mechanical measurements on these yarns have confirmed that the elastic properties are not even close to that of an individual nanotube. This problem was addressed by irradiation experiments, where we presented two ways to strengthen the CNT fibres. It was found that not only irradiation by electrons but ultraviolet light as well leads to a covalent C-C bond formation of nanotubes in the fiber. Illumination of DMF treated fibres by UV light increases both the conductivity and the mechanical strength, which can be explained by the photo-chemistry between the free radicals on the surface of CNTs and DMF molecules.

Electrical measurements have demonstrated that a low dose of electron irradiation can significantly increase the shear modulus via cross-linking of CNTs in the fibre, but a high electron dose disorders the graphitic structure and results in a loss of the intrinsically high Young's modulus of the individual tubes. In contrast to electrons, the ultraviolet photons do not displace carbon atoms in the nanotube, therefore reinforcement can be achieved by keeping the graphitic structure of the tubes intact.

Furthermore, if the fibre thickness is comparable with the penetration of UV, the reinforcement of CNT fibres is homogeneous and this type of irradiation becomes an even more promising method for strengthening composite materials. Since UV light is also applicable to larger surfaces, it opens the door to produce CNT based composites with high strength and conductivity on a large scale.



# Appendix A

## Purification of Nanotubes

Purification of nanotubes is, in general, a very demanding task with lots of difficulties. The as-produced MWNT soot, for instance, by arc-discharge (AD) contains lots of different impurities. Mainly these are graphite sheets, catalyst particles, smaller fullerenes, graphitic polyhedrons and amorphous carbon in the form of particles or coating on the sidewalls of CNTs. They should all be removed before further investigations. The ideal purification method subtracts all the contamination without modifying the structure of CNTs. Unfortunately, the common industrial methods use strong oxidation and/or acid refluxing techniques, which have an influence on and sometimes degrade the structure of the tubes.

### A.1 Overview of purification methods on CNTs

In this appendix, different purification methods of MWNTs and in some cases SWNTs will be discussed. With a view to determining the level of purity and CNT structure after the treatment employed electron microscopy techniques were used. For the first approximation scanning electron microscopy (SEM) analyses were performed. The graphitisation level and the damage caused by purification can be observed by transmission electron microscopy (TEM) investigation before and after purification. For instance, Figure A.1b shows an inferior quality purification process with wall structure of the nanotube destroyed. A properly chosen purification method results in invisible deformations by TEM, see in Figure A.1a.

Considering further applications and measurements the most important parameter for CNT purification is the method chosen, as the effect on an entire sample will also depend on the technique applied. Unfortunately, most of the techniques have an influence on the CNT such as cutting, functionalising or oxidation. Conse-

quently, measurements always have to keep in mind the influence of the purification method applied.

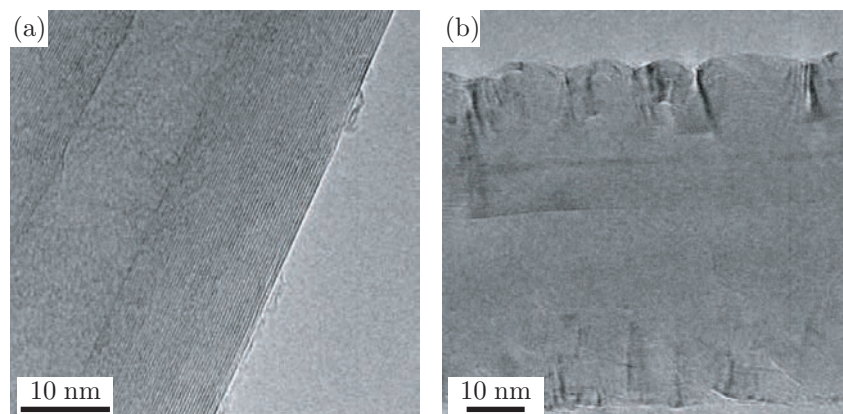


Figure A.1: TEM micrograph of nanotubes produced by CVD. (a) represents a good purification process while (b) shows the nanotube walls damaged by purification.

### A.1.1 Chemical purification

Many different purification schemes have been developed, aiming at oxidising the amorphous carbon, removing the catalytic particles and retaining only the tubes. Chemical purifications not only involve acid or base treatments, but also simple oxidation in air, where the carbon atoms are removed in the form of  $\text{CO}_2$  or  $\text{CO}$ .

#### Oxidation in air

In the first attempts, nanotubes were heated to  $600^\circ\text{C} - 800^\circ\text{C}$  in air. Unfortunately, both tubes and impurities oxidise at high temperatures. Oxidation is favoured for tubes at their tips (because of the high curvature). The small difference in oxidation rates of particles and tubes results in little control over the purification.

#### Oxidation in acidic solvent

Wet oxidation techniques are based on oxidation in acidic solutions such as hydrochloric-acid ( $\text{HCl}$ ), nitric-acid ( $\text{HNO}_3$ ), hydrogen-peroxide ( $\text{H}_2\text{O}_2$ ) or potassium permanganate ( $\text{KMnO}_4$ ). For purification, the CNTs are oxygenised in an ultrasound bath. After a couple of hours of sonication, the impurities are dissolved. The suspension is then filtered and washed with distilled water. The other modification of this technique is ultrasonically assisted filtration, where the nanotube suspension is *in situ* sonicated during filtration [155].

Refluxing is also widely used. This method, in general, involves boiling a liquid

in a vessel attached to a condenser so that the vapours condense continuously for reboiling. In the case of CNT purification, the suspension of nanotubes and for instance,  $\text{H}_2\text{O}_2$  is continuously stirred in a hot environment. The advantage of this method is that the reaction can be maintained for long a period with a relatively small amount of substance. Figure A.2 shows a typical arrangement of the reflux system.

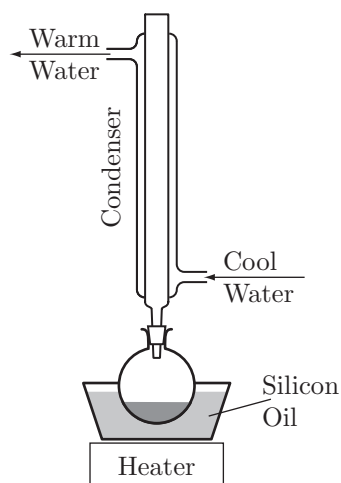


Figure A.2: Schematic drawing about the reflux purification of CNTs

Wet oxidations have given much better yields (< 40%) than the oxidation in air, since the solvent-based oxidation is slower and more homogeneous. However, nanotubes exposed to long refluxation in strong acid, introduce many defects into the surface of the CNTs or may even be chemically cut. Oxidation of nanotubes in solution also results in the attachment of many hydroxyl (-OH) and carboxyl (-COOH) functional groups on the surface [51, 156], which can change the reactivity and the chemical properties of nanotubes as well.

### A.1.2 Mechanical purification

Oxidation of carbon impurities is a simple process contrary to metallic particles. In the case of oxidation in air, metallic particles are oxidised but in the sample. For wet oxidation, the nature of the metal is an important parameter. For instance, Fe and Co based catalysts can be dissolved easily in contrast to Y. One of the most difficult problems in SWNT purification is separating the encapsulated metallic particles and carbon nanotubes. Transition metal particles, necessary for SWNT synthesis are mostly surrounded by graphitic layers. Very aggressive chemical purification using acids is required in order to remove these protective graphitic layers before the

metallic particle is reached. Unfortunately, together with the protective graphite layer CNTs can also be destroyed by acid treatment. The aim of the mechanical purification is to remove the graphite-covered metal particles without destroying the nanotubes. Thien-Nga and co-workers found a way to kick out the catalyst particles from the protecting shell [157].

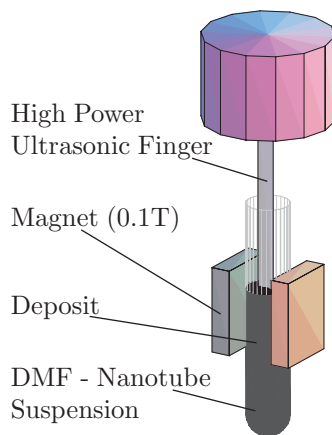


Figure A.3: Schematic drawing of the mechanical purification scheme [157].

The presence of these ferromagnetic particles overwhelms the magnetic response and prevents the intrinsic magnetic properties of carbon nanotubes from being measured. Knocking out the catalyst particles from their shell is possible by sonicating a mixture of SWNT suspension and hard inorganic nanoparticles like  $\text{ZrO}_2$  or  $\text{CaCO}_3$ . Placed in a magnetic field, the ferromagnetic particles can be effectively removed and collected (Figure A.4a and b).

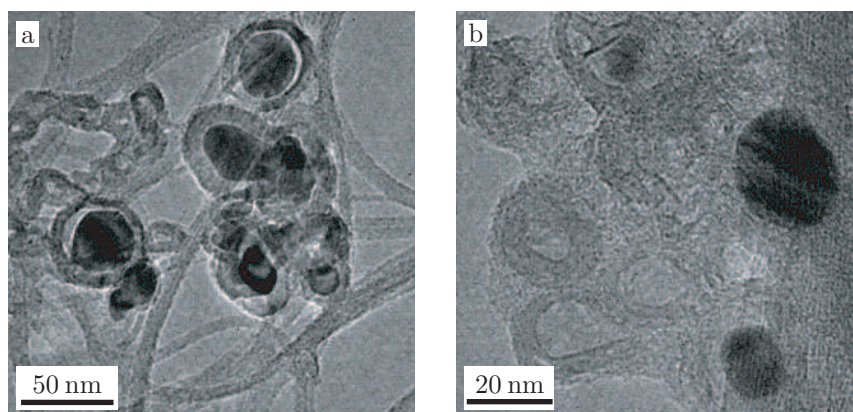


Figure A.4: (a) magnetic particles enclosed in graphitic shells. (b) after 24 hours of sonication in the presence of  $\text{ZrO}_2$  [157].

Hard inorganic particles can eject the metallic core from the graphitic shells

(Figure A.3.a and b). The ferromagnetic impurities form a deposit trapped close to the magnets. Subsequent electron-spin resonance (ESR) measurements have demonstrated that the presence of ferromagnetic particles in the purified material was negligible.

### A.1.3 Purification with surfactant by ultrasonication

A difficult problem in MWNT purification is separating the graphitic nanoparticles and carbon nanotubes produced by AD. Since both are made from carbon, selective oxidation is not a suitable method. With acid treatment, both the particles and nanotubes are damaged. The surfactant purification technique can clean the nanotubes without damaging the nanotubes through the use of reversible interaction of nanotubes and surfactant.

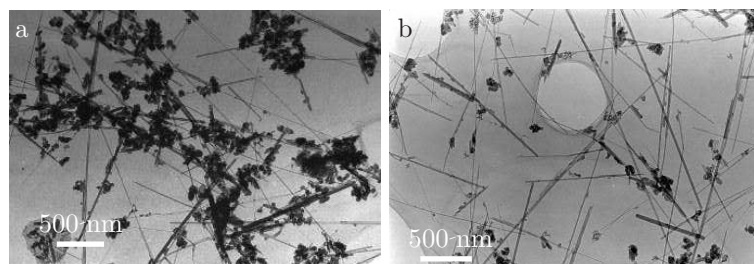


Figure A.5: Results of surfactant purification in the method of Bonard et al. [158]. Raw nanotubes (a) were dispersed in the aqueous suspension of an anionic surfactant followed by filtration resulting in separation of nanotubes from impurities (b).

In this method the raw product is dispersed in an aqueous solution of SDS. In order to ensure that the nanotubes form micelles<sup>1</sup>, 2 critical micelle concentrations (CMC) were taken. Particles were separated from nanotubes due to ultrasonic vibration [158]. CNT-nanoparticle agglomerates are forced to vibrate and become more dispersed. The colloidal suspension is then centrifuged and filtrated using large pore size filter paper (400  $\mu\text{m}$ ). In order to enhance the separation yield, successive sonication-filtration is carried out.

Surfactant adsorption at interfaces has been widely studied because of its importance in detergents, lubrication and colloid stabilisation. CNTs are insoluble and hardly dispersible in most solvents, especially in water. However, they form a stable suspension when dispersed in 1 wt% aqueous solution of an anionic surfactant: Sodium-Dodecyl-Sulfate (SDS) [158].

<sup>1</sup>Micelle: aggregates of the colloid particles. Amphiphilic molecules with hydrophobic tails and hydrophilic heads form micelles of various shapes and sizes above a minimum threshold concentration known as the critical micelle concentration CMC [159, 160]

The chemical absorption of SDS molecules creates a distribution of negative charges which prevent aggregation and induce a stable suspension. Richard et al. [161], together with other surfactants, investigated the different organisations of SDS<sup>2</sup> molecules on the surface of nanotubes. The SDS is a long chain molecule containing a hydrophobic and a hydrophilic parts with C<sub>12</sub>H<sub>25</sub> alkyl chain and SO<sub>4</sub><sup>2-</sup>, respectively. Above CMC of SDS in the solution, the hydrophobic part attaches to the nanotube surface by van der Waals interactions. While the hydrophilic part is toward the aqueous phase. TEM observations showed that the SDS molecules organise themselves in cylinders around CNTs (like hedgehog) and they can also be spooled up on the surface of the tube at a well defined angle depending on the tube diameter A.6.

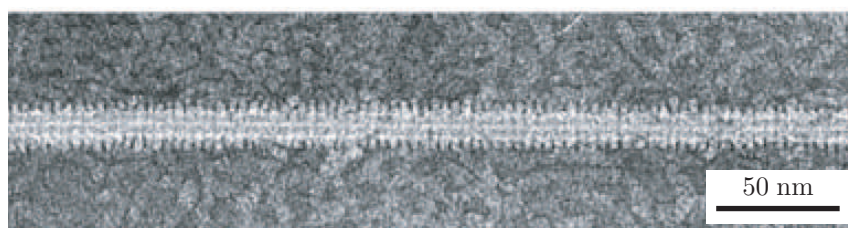


Figure A.6: TEM images of the supramolecular organisation of the SDS molecules on CNTs.

It was also noticed that below the CMC after 12 hours of dialysis no striations were detected even with the covered nanotubes which could indicate the presence of SDS molecules. These observations suggest that the interaction of the hydrophobic part is reversible below CMC of the surfactant [161].

## A.2 Results on the purification of CNTs

### A.2.1 Purification of multiwall nanotubes grown by CCVD

During the optimisation of CNT production, almost all the above mentioned wet purification techniques were attempted including also sonication in diluted and concentrated HNO<sub>3</sub>, refluxation of the nanotubes in concentrated hydrogen peroxide, H<sub>2</sub>O<sub>2</sub>. In order to avoid that the wall of nanotubes is damaged by the acid and preserve the well-graphitised parallel structure, gently acid treatment was preferred. Since the applied support was CaCO<sub>3</sub>, diluted HNO<sub>3</sub> or HCl ( $\approx$ 1M) could completely dissolve the residual CaCO<sub>3</sub> by short sonication.

---

<sup>2</sup>NaC<sub>12</sub>H<sub>25</sub>SO<sub>4</sub>

In order to observe the influence of the acid treatments, SEM and TEM were carried out. The best results were obtained at 15 minutes of sonication in  $\approx 1\text{M}$  of HCl. The resulting solid was filtered, washed with distilled water and safely stored in ethanol. Figure A.7a and b show that inside the as-product CCVD not only nanotubes grow (spaghetti-like wires) but also residual support and catalyst particles (large and small white spots).

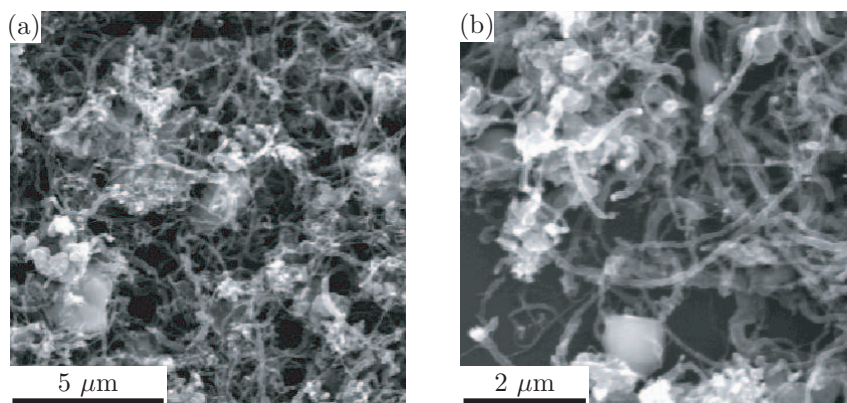


Figure A.7: SEM micrograph of raw CCVD nanotubes at (a) 4000 and (b) 8000 magnification. The large and small white spots are most probable the calcium carbonate and catalyst particles, respectively.

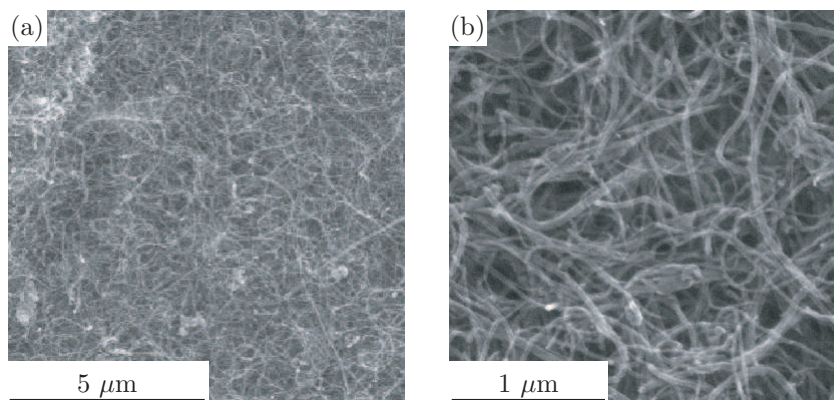


Figure A.8: SEM micrograph of purified samples from the CCVD furnace with a dense mat of CNTs. a) 5000 and (b) 20000 magnification.

Figure A.8.a and b show SEM images of purified CNTs grown at  $680^\circ\text{C}$  using a catalyst with 33 mol% of cobalt. A dense network of nanotubes can be seen with an outer diameter of about 15 nm and a length of few microns without any indication of catalyst or support particles. The  $\text{CaCO}_3$  and  $\text{Fe}_2\text{Co}$  catalyst are removed in one step. Actually this is a very good choice, because it speeds up the purification

process because both materials are easily dissolved in diluted HCl.

As also confirmed by TEM in Figure A.9.a and b, the applied one-step purification allows a complete removal of the residual catalyst, thus CNTs with a high level of purity can be produced by CCVD. The good purity level of the process, here, can be stressed, because of its importance in reproducibility and further applications.

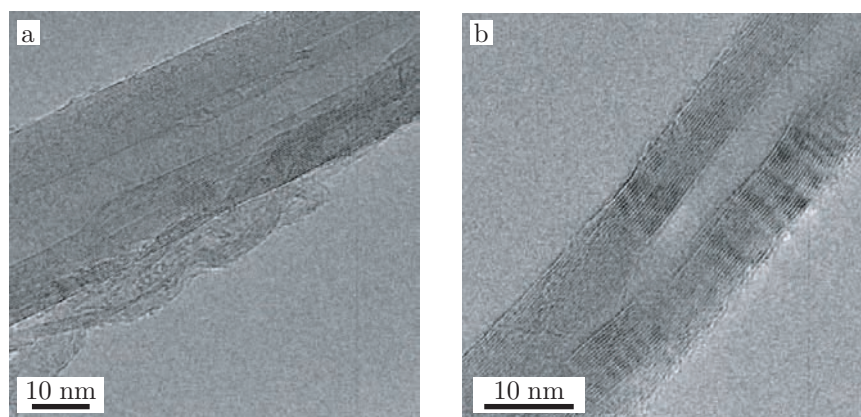


Figure A.9: High resolution TEM picture of (a) raw and (b) purified CCVD nanotubes.

### A.2.2 Purification of multiwall nanotubes grown by AD

In the case of arc-discharge growth, the same simple purification method in HCl is not applicable as it was for CCVD grown nanotubes. In the case of AD different impurities exist so they can be removed in a different way.

The most difficult part is to remove the polyhedral graphitic particles which make up one-third of the volume in the raw product. Since they are also made from carbon, they react similarly as CNTs. Hence, wet oxidation will consume both the impurities and the CNTs, as well. Because oxidation is faster where the curvature is higher, there is a small differentiation in the speed and the impurities will disappear faster. Capes et al. [162] developed diluted acidic purification with the mass yield of typically 70%. The only problem with this technique is the oxidation of the surface of the nanotubes. CNT purification in a basic solvent, as mentioned above on page 101, is a long procedure. Nevertheless, many groups choose this way, since it does not modify the CNT surface and it is easy to wash them out with pure water.

1 g of raw MWNTs require 5l distilled water and 25g SDS for purification. The procedure is the following: MWNTs produced by AD are mixed with H<sub>2</sub>O and SDS. In order to make a homogeneous suspension it is necessary to sonicate with an ultrasonic probe (Bandelin UW200) for 80 minutes. Sedimentation followed by centrifugation at 5000 rpm for 15 min. removes the large impurities from the



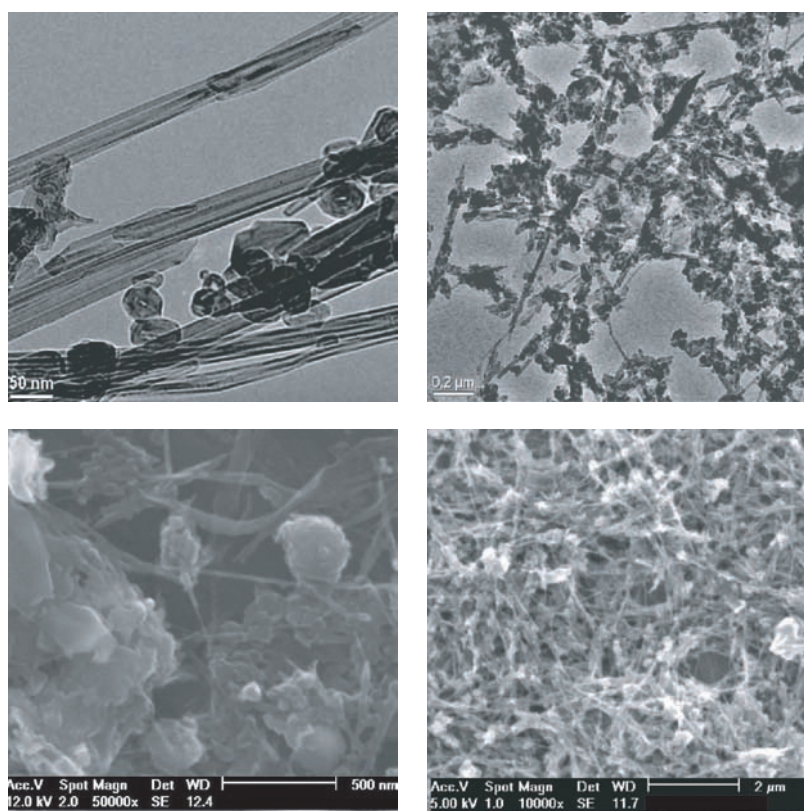


Figure A.10: SEM and TEM micrographs of raw AD nanotubes.

suspension. A filtration apparatus with a large enough funnel allows sonication of the colloidal suspension during the filtration process. In order to enhance the separation yield, sonication-filtration was repeated twice. To this end, the residue was re-dispersed in a fresh water-SDS solution and filtered. Finally, the nanotubes were recuperated from the paper.

In order to follow the level of purity, CNTs were observed in SEM after all the purification steps. TEM investigations were done for structural comparison at the final stage. Results after three repetition are shown in Figure A.11.

The presence of surfactant can be checked using energy dispersive X-ray analysis (EDX)<sup>3</sup>, which confirmed a considerable presence of SDS at the beginning of the cleaning process. After the second and the third wash, it was impossible to detect any sulfur by EDX. Electron energy loss spectroscopy (EELS) was also carried out because of its better sensibility to the elements with low mass number. EELS confirmed with 1% of accuracy that purified nanotubes after the third wash did not contain a detectable amount of SDS.

<sup>3</sup>Detailed description of microscopy techniques is available in Chapter 4.

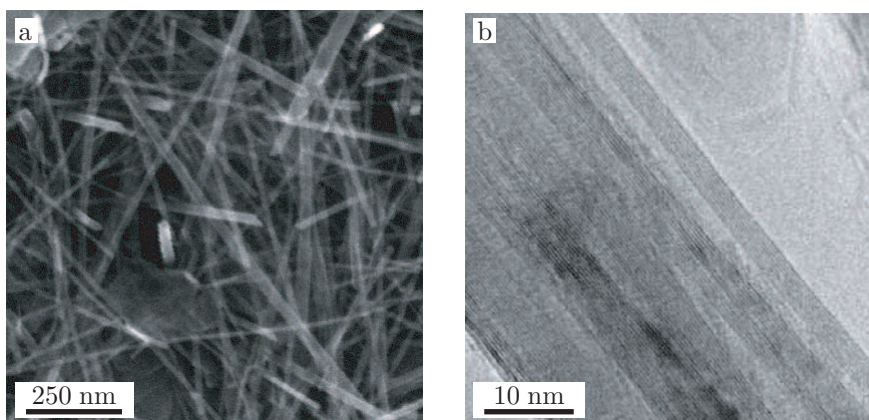


Figure A.11: (a) SEM and (b) TEM micrographs of the purified AD nanotubes.

As was presented in this appendix, many different purification methods exist depending on the method of growth of nanotubes. Purification of CNTs can be performed cautiously with regard to further applications. In the case of optimised CCVD growth of CNTs described in Chapter 5, a one-step wet oxidation technique was employed. Sonication in diluted HCl ( $\approx 1\text{M}$ ) completely dissolved the residual catalyst particles and  $\text{CaCO}_3$  without visible damage to the walls of nanotubes.

## Appendix B

# Data Acquisition from the HP3562A Digital Signal Analyzer


For the measurement of the Young moduli of different CNT ropes, we used a HP3562A Digital Analyzer in the configuration shown in Figure 6.22 and discussed in Chapter 6. In order to handle later the measured data – obtained during the series of measurement, – we had to develop a simple, clearly structured, PC based application. It had to carry out the following four tasks:

1. Communication. First establish a connection with a PC and then send and receive the executing commands.
2. Manipulation. After obtaining the measured data from the digital analyser in a raw format, it had to separate the global variables and initial conditions, i.e. the header from the measured data and converting them to floating point numbers.
3. Visualisation. The results (magnitude and phase vs. frequency) had to be plotted out.
4. Archivation. For comparison and documentation purposes we wanted to save the processed lists and the corresponding information in an automated way.

Since the measuring speed (sampling) did not play a critical role, it was possible to use high-level programming tool. We chose Labview, because both the data manipulation modules together with the GPIB interfacing and the graphical user interface (GUI) were manageable in an easy manner.

## B.1 The program in Labview

The user interface (Figure B.1) shows the main functionalities, which can be understood by the process of measurement and by running the Labview code:

1. We first set up the digital analyser – the settings are shown later on the right hand side of Figure B.1.
2. During the experiment the digital analyser registers internally the measured data.
3. We complete the administrative and rope property fields (name, diameter, length, mass) in the left upper corner.
4. After the measurement finished, we start the program by clicking the  button. In the background the following tasks are running:
  - (a) With the command DDAS the program takes over control from the analyser and loads the data to the PC (Figure B.2)
  - (b) In the main frame (Figure B.3) first the raw string is divided into the header and measured data, which will be converted to floating point numbers and forwarded to the internal box, where the real and imaginary components and the corresponding magnitude and phase values are calculated.
  - (c) Automatic archiving is done in Figure B.4.
  - (d) When the above tasks are finished, then the program gives back control to the analyser by the command LCL (Figure B.5). (Possibly the analyser is required to press the “local” button.)

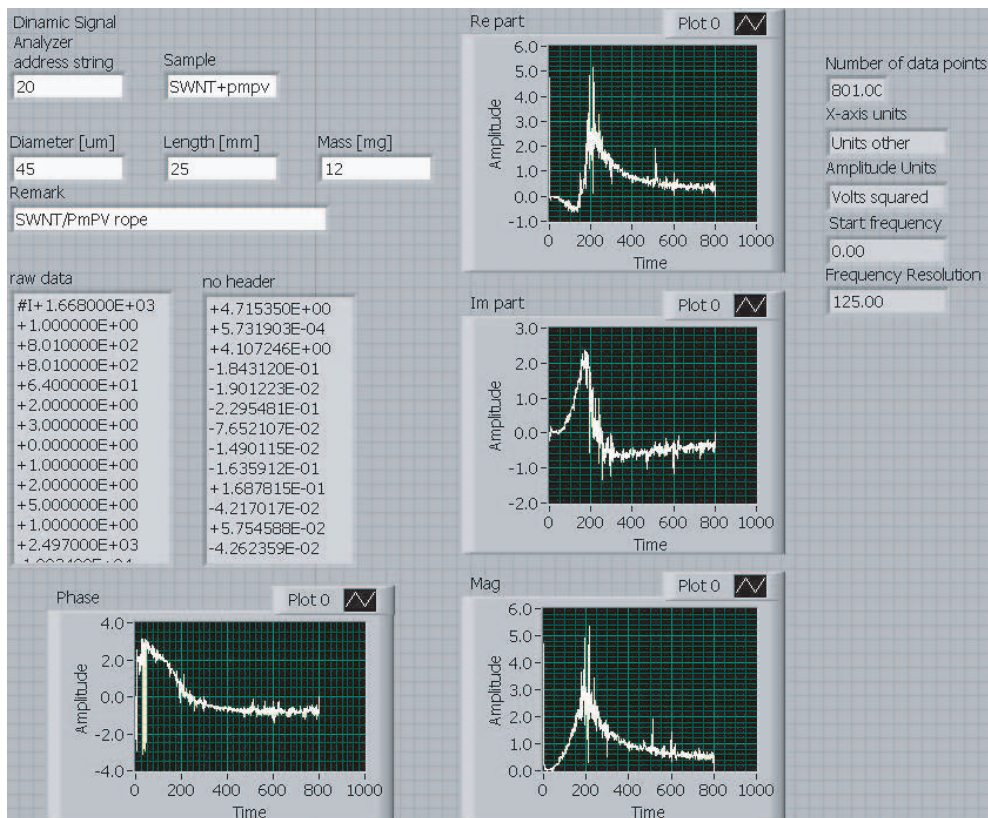


Figure B.1: The graphical user interface (GUI).

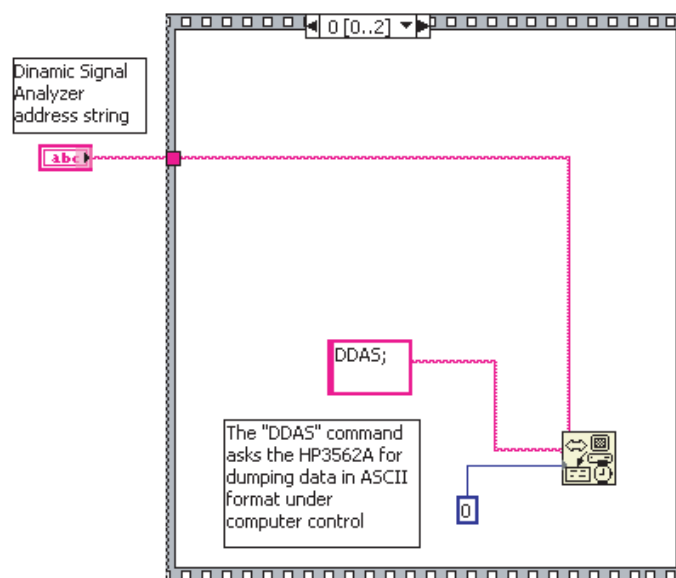


Figure B.2: DDAS takes over control from the analyser and interrogates it for dumping data in ASCII format.

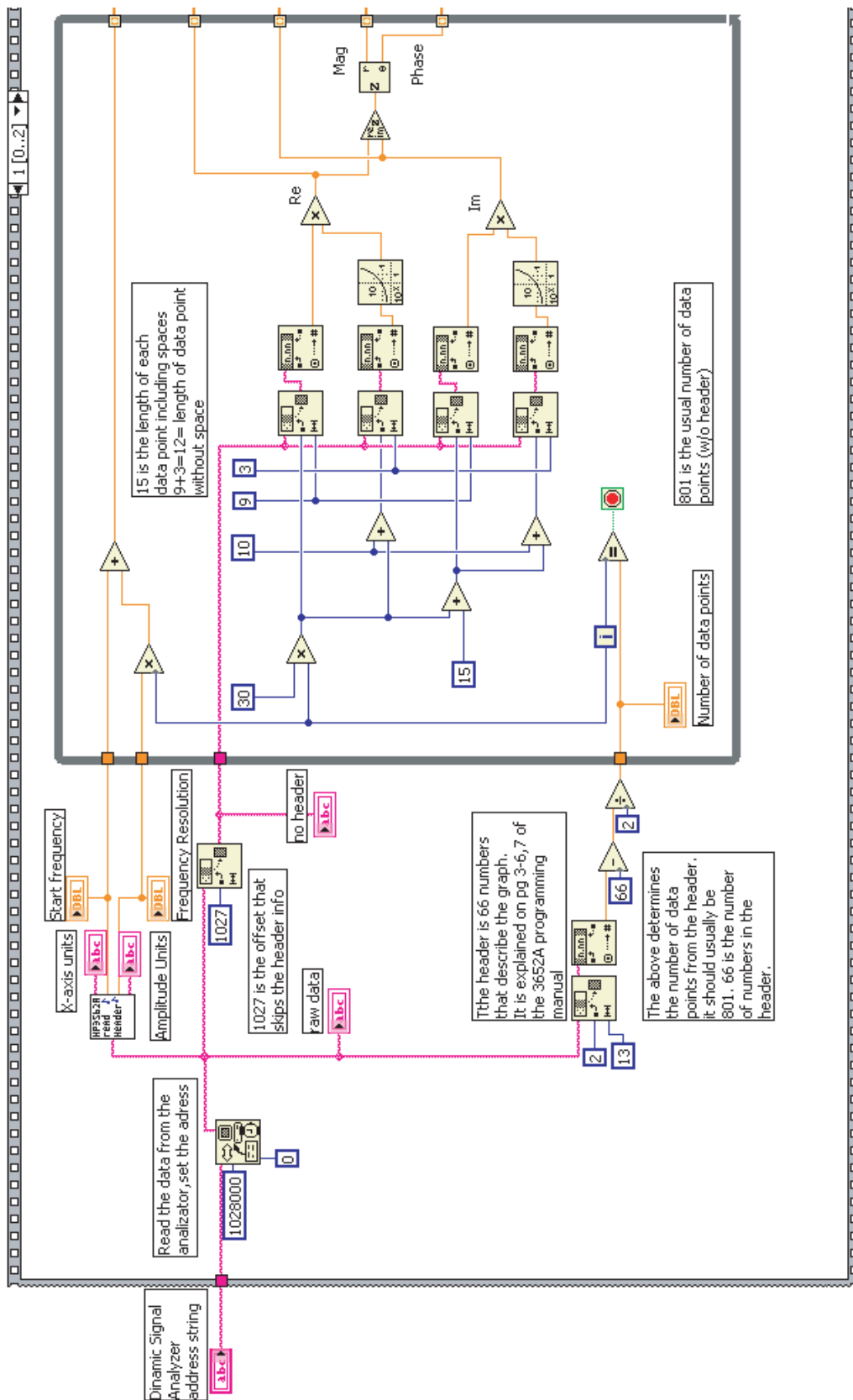


Figure B.3: Separating the header from the measured data, from which the phase and the magnitude are calculated.

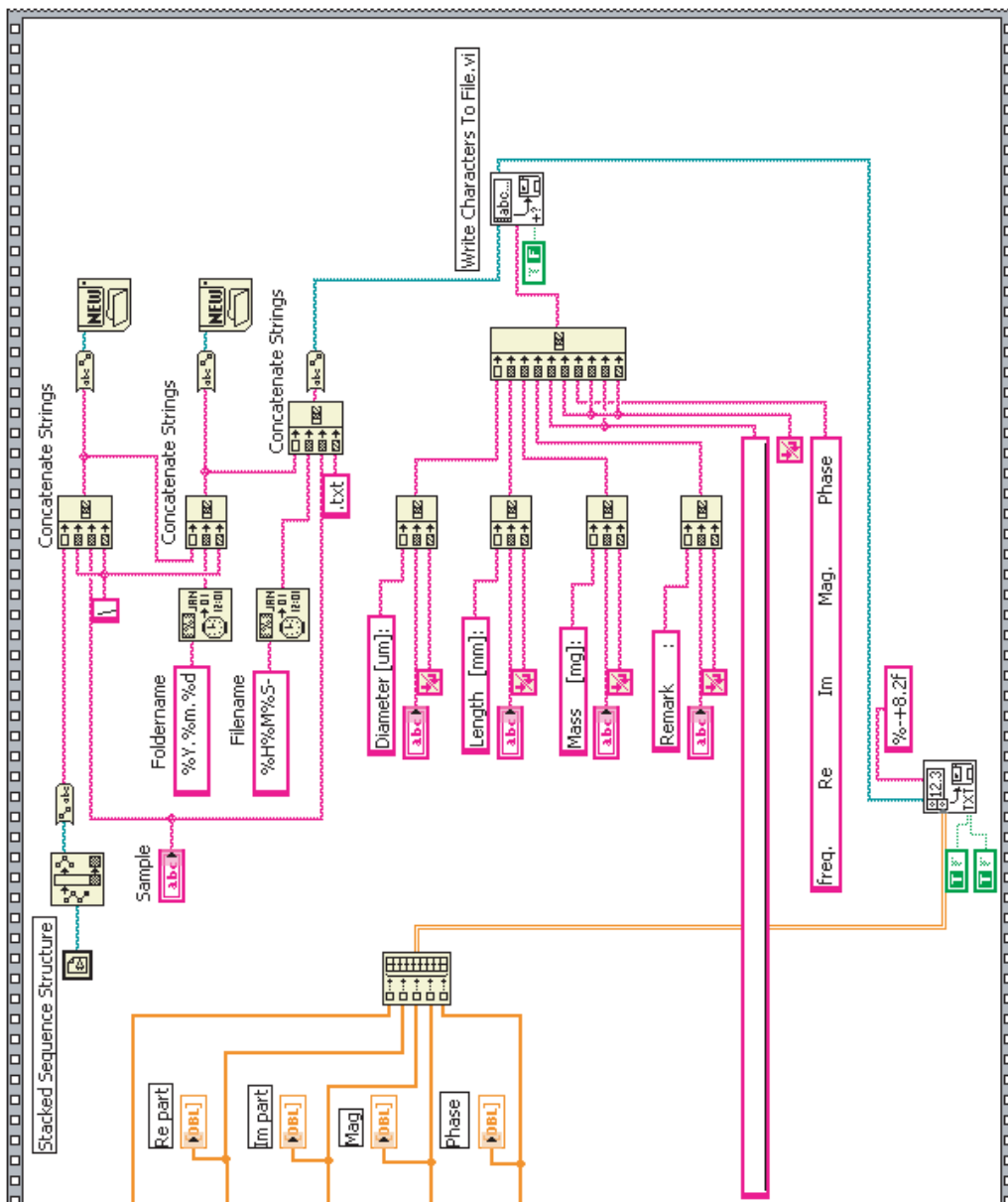


Figure B.4: Automated archiving in ASCII format.

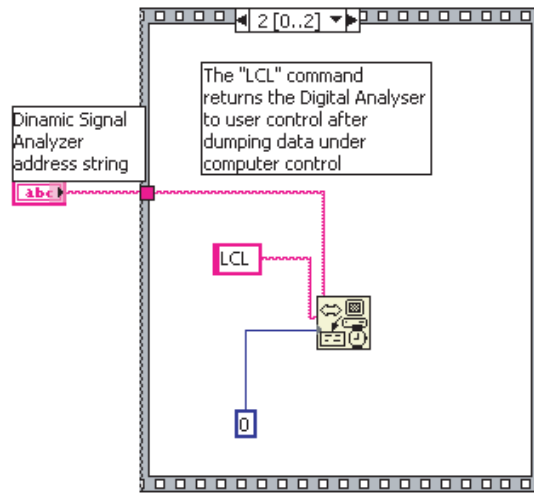


Figure B.5: LCL gives back control to the analyser.



# Bibliography

- [1] Richard Feynman. Quantum mechanical computers. *Optics News*, February:11, 1985.
- [2] A. Huczko. Synthesis of aligned carbon nanotubes. *Applied Physics A*, 74:617, 2002.
- [3] C. M. Lieber. One dimensional nanostructures: Chemistry, physics and application. *Solid State Communication*, 107:607, 1998.
- [4] N. de Jonge, Y. Lamy, K. Schoots, and T. H. Oosterkamp. High brightness electron beam from a multi-walled carbon nanotube. *Nature*, 420:393, 2002.
- [5] Z. Chen, Z. Wu, J. Sippel, and A. G. Rinzler. Metallic/semiconducting nanotube separation and ultra-thin, transparent nanotube films. *AIP Conference Proceedings*, 723:69, 2004.
- [6] P. Glatkowski, P. Wallis, and M. Trottier. The twists of carbon nanotubes. *SPIE's oemagazine*, April:22, 2005.
- [7] L. Jin, C. Bower, and O. Zhou. Alignment of carbon nanotubes in a polymer matrix by mechanical stretching. *Applied Physics Letters*, 73:1197, 1998.
- [8] J. Hone, M.C. Llaguno, N.M. Nemes, A.T. Johnson, J.E. Fisher, D.A. Walters, M.J. Casavant, J. Schmidt, and R.E. Smalley. Electrical and thermal transport properties of magnetically aligned single wall carbon nanotube films. *Applied Physics Letters*, 77:666, 2000.
- [9] B. Vigolo, P. Poulin, M. Lucas, P. Launois, and P. Bernier. Improved structure and properties of single-wall carbon nanotube spun fibers. *Applied Physics Letters*, 81:1210, 2002.
- [10] W. Zhou, J. Vavro, C. Guthy, K. I. Winey, J. E. Fischer, L. M. Ericson, S. Ramesh, R. Saini, V. A. Davis, C. Kittrel, M. Pasquali, R. H. Hauge, and R. E. Smalley. Single wall carbon nanotube fibers extruded from super-acid

- suspensions: Preferred orientation, electrical and thermal transport. *Journal of Applied Physics*, 95:649, 2004.
- [11] A. B. Dalton, S. Collins, E. Munoz, J. M. Razal, V. H. Ebron, J. P. Ferraris, J. N. Coleman, B. G. Kim, and R. H. Baughman. Super-tough carbon-nanotube fibres. *Nature*, 423:703, 2003.
- [12] J.-P. Salvetat, G. A. D. Briggs, J.-M. Bonard, R. R. Bacsa, A. J. Kulik, T. Stöckli, N. Burnham, and L. Forró. Elastic and shear moduli of single-walled carbon nanotube ropes. *Physical Review Letters*, 82:944, 1999.
- [13] A. Kis, J. P. Salvetat, T. N. Lee, E. Ljubovic, A. Kulik, W. Benoit, J. Brugger, and L. Forró. Reinforcement of single-walled carbon nanotube bundles by intertube bridging. *Nature Materials*, 3:153, 2004.
- [14] A. V. Rode, E. G. Gamaly, A. G. Christy, J. G. Fitz Gerald, S. T. Hyde, R. G. Elliman, B. Luther-Davies, A. I. Veinger, J. Androulakis, and J. Giapintzakis. Unconventional magnetism in all-carbon nanofoam. *Physical Review B*, 70:054407, 2004.
- [15] H. W. Kroto, J. R. Heath, S. C. O'Brian, R. F. Curl, and R. E. Smalley. C<sub>60</sub>: Buckminsterfullerene. *Nature*, 318:162, 1985.
- [16] A. Oberlin, M. Endo, and T. Koyama. Filamentous growth of carbon through benzene decomposition. *Journal of Crystal Growth*, 32:335, 1976.
- [17] S. Iijima. High-resolution electron-microscopy of some carbonaceous materials. *Journal of Microscopy*, 119:99, 1980.
- [18] S. Iijima. Helical microtubules of graphitic carbon. *Nature*, 354:56, 1991.
- [19] T. W. Odom, J.-L. Huang, P. Kim, and C. M. Lieber. Structure and electronic properties of carbon nanotubes. *Journal of Physical Chemistry B*, 104:2794, 2000.
- [20] J. M. Zuo, I. Vartanyants, M. Gao, R. Zhang, and L. A. Nagahara. Atomic Resolution Imaging of a Carbon Nanotube from Diffraction Intensities. *Science*, 300:1419, 2003.
- [21] M. Hulman, R. Pfeiffer, and H. Kuzmany. Raman spectroscopy of small-diameter nanotubes. *New Journal of Physics*, 6:1, 2004.
- [22] S. Amelinckx, A. Lucas, and P. Lambin. Electron Diffraction and Microscopy of Nanotubes. *Reports on Progress in Physics*, 62:1471, 1999.

- [23] M. Kociak, K. Suenaga, K. Hirahara, Y. Saito, T. Nakahira, and S. Iijima. Linking Chiral Indices and Transport Properties of Double-Walled Carbon Nanotubes. *Physical Review Letters*, 89:155501, 2002.
- [24] C.-H. Kiang, M. Endo, P. M. Ajayan, G. Dresselhaus, and M. S. Dresselhaus. Size effects in carbon nanotubes. *Physical Review Letters*, 81:1869, 1998.
- [25] M.-F. Yu, O. Lourie, M. J. Dyer, K. Moloni, T. F. Kelly, and R. S. Ruoff. Strength and breaking mechanism of multiwalled carbon nanotubes under tensile load. *Science*, 287:637, 2000.
- [26] K. Hernadi, L. Thien-Nga, and L. Forró. Growth and microstructure of catalytically produced coiled carbon nanotubes. *Journal of Physical Chemistry B*, 105:12464, 2001.
- [27] L. Thien-Nga, K. Hernadi, and L. Forró. Catalytic growth of carbon nanorods on a high- $T_c$  substrate. *Advanced Materials*, 13:148, 2001.
- [28] G. Zhang, X. Jiang, and E. Wang. Tubular graphite cones. *Science*, 300:472, 2003.
- [29] R. M. Wang and H. Z. Zhang. Analytical tem investigations on boron carbonitride nanotubes grown via chemical vapour deposition. *New Journal of Physics*, 6:78, 2004.
- [30] Ch. Tang, Y. Bando, and T. Sato. Catalytic growth of boron nitride nanotubes. *Chemical Physics Letters*, 362:185, 2002.
- [31] C. Guerret-Piécourt, Y. Le Bouar, A. Loiseau, and H. Pascard. Relation between metal electronic structure and morphology of metal compounds inside carbon nanotubes. *Nature*, 372:761, 1994.
- [32] B. W. Smith, M. Monthieux, and D. E. Luzzi. Encapsulated  $c_{60}$  in carbon nanotubes. *Nature*, 396:323, 1998.
- [33] E. Philp, J. Sloan, A. I. Kirkland, R. R. Meyer, S. Friedrichs, J. L. Hutchison, and M. L. H. Green. An encapsulated helical one-dimensional cobalt iodide nanostructure. *Nature Materials*, 2:788, 2003.
- [34] R. Saito, M. Fujita, G. Dresselhaus, and M. S. Dresselhaus. Electronic structure of chiral graphene tubules. *Applied Physics Letters*, 60:2204, 1992.
- [35] X. Blase, L. X. Benedict, E. L. Shirley, and S. G. Louie. Hybridization effects and metallicity in small radius carbon nanotubes. *Physical Review Letters*, 72:1878, 1994.

- [36] L. Chico, V. H. Crespi, L. X. Benedict, S. G. Louie, and M. L. Cohen. Pure carbon nanoscale devices: Nanotube heterojunctions. *Physical Review Letters*, 76:971, 1996.
- [37] J. W. Mintmire, B. I. Dunlap, and C. T. White. Are fullerene tubules metallic. *Physical Review Letters*, 68:631, 1992.
- [38] P. Avouris. Carbon nanotube electronics. *Chemical Physics*, 281:429, 2002.
- [39] N. Hamada, S. Sawada, and A. Oshiyama. New one-dimensional conductors: Graphitic microtubules. *Physical Review Letters*, 68:1579, 1992.
- [40] S. G. Louie. Electronic properties, junctions, and defects of carbon nanotubes. *Topics in Applied Physics*, 80:113, 2001.
- [41] C. L. Cheung M. Ouyang, J.-L. Huang and C. M. Lieber. Energy gaps in “metallic” single-walled carbon nanotubes. *Science*, 292:702, 2001.
- [42] S. J. Tans, M. H. Devoret, H. Dai, A. Thess, R. E. Smalley L. J. Geerligs, and Cees Dekker. Individual single-wall carbon nanotubes as quantum wires. *Nature*, 386:474, 1997.
- [43] R. Krupke, F. Henrich, H. V. Lohneysen, and M. M. Kappes. Separation of Metallic from Semiconducting Single-Walled Carbon Nanotubes. *Science*, 301:344, 2003.
- [44] M. S. Strano, C. A. Dyke, M. L. Usrey, P. W. Barone, M. J. Allen, H. Shan, C. Kittrell, R. H. Hauge, J. M. Tour, and R. E. Smalley. Electronic Structure Control of Single-Walled Carbon Nanotube Functionalization. *Science*, 301:1519, 2003.
- [45] C. Schönenberger, A. Bachtold, C. Strunk, J.-P. Salvetat, and L. Forró. Interference and interaction in multi-wall carbon nanotubes. *Applied Physics A*, 69:283, 1999.
- [46] T. W. Ebbesen. Cones and tubes: Geometry and chemistry of carbon. *Accounts of Chemical Research*, 31:558, 1998.
- [47] S. Niyogi, M. A. Hamon, H. Hu, B. Zao, P. Bhowmik, R. Sen, M. E. Itkis, and R. C. Haddon. Chemistry of single-walled carbon nanotubes. *Accounts of Chemical Research*, 35:1105, 2002.
- [48] T. W. Ebbesen. Carbon nanotubes. *Annual Reviews of Material Science*, 24:235, 1994.

- [49] S. Iijima, P. M. Ajayan, and T. Ichihashi. Growth model for carbon nanotubes. *Physical Review Letters*, 69:3100, 1992.
- [50] M. S. Dresselhaus, G. Dresselhaus, and Ph. Avouris. *Carbon Nanotubes: Synthesis, Structure, Properties, and Applications*. Springer-Verlag, 2001.
- [51] A. Hirsch. Functionalization of single-walled carbon nanotubes. *Angew. Chem. Int. Ed.*, 41:1853, 2002.
- [52] M. O'Connell, P. Boul, L. M. Ericson, C. Huffman, Y. Wang, E. Haroz, C. Kuper, J. Tour, K. D. Ausman, and R. E. Smalley. Reversible water-solubilization of single-walled carbon nanotubes by polymer wrapping. *Chemical Physics Letters*, 342:265, 2001.
- [53] B. I. Yakobson, C. J. Brabec, and J. Bernholc. Nanomechanics of carbon tubes: Instabilities beyond the linear response. *Physical Review Letters*, 76:2511, 1996.
- [54] M. R. Falvo, G. J. Clary, R. M. Taylor, V. Chi, F. P. Brooks, Jr. S. Washburn, and R. Superfine. Bending and buckling of carbon nanotubes under large strain. *Nature*, 389:582, 1997.
- [55] M. M. J. Treacy, T. W. Ebbesen, and J. M. Gibson. Exceptionally high young's modulus observed for individual carbon nanotubes. *Nature*, 381:678, 1996.
- [56] P. Poncharal, Z. L. Wang, D. Ugarte, and W. A. De Heer. Electrostatic deflections and electromechanical resonances of carbon nanotubes. *Science*, 283:1513, 1999.
- [57] J.-P. Salvetat, A. J. Kulik, J.-M. Bonard, G. A. D. Briggs, T. Stöckli, K. Méténier, S. Bonnamy, F. Béguin, N. A. Burnham, and L. Forró. Elastic modulus of ordered and disordered multiwalled carbon nanotubes. *Advanced Materials*, 11:161, 1999.
- [58] A. Thess, R. Lee, P. Nikolaev, H. Dai, P. Petit, J. Robert, C. Xu, Y. H. Lee, S. G. Kim, A. G. Rinzler, D. T. Colbert, G. Scuseria, D. Tománek, J. E. Fischer, and R. E. Smalley. Crystalline ropes of metallic carbon nanotubes. *Science*, 273:483, 1996.
- [59] J. P. Lu. Elastic Properties of Carbon Nanotubes and Nanoropes. *Physical Review Letters*, 79:1297, 1997.

- [60] M. Damnjanovic, I. Milosevic, T. Vukovic, and Sredanovic. Full symmetry, optical activity, and potentials of single-wall and multiwall nanotubes. *Physical Review B*, 60:2728, 1999.
- [61] A. J. Stone and D. J. Wales. Theoretical-studies of icosahedral c60 and some related species. *Chemical Physics Letters*, 128:501, 1986.
- [62] S. Iijima. Carbon nanotubes. *MRS Bulletin*, 19(11):43, 1994.
- [63] B. I. Yakobson, M. P. Campbell, C. J. Brabec, and J. Bernholc. High strain rate fracture and c-chain unraveling in carbon nanotubes. *Computational Materials Science*, 8:341, 1997.
- [64] András Kis. *Mechanical Properties of Mesoscopic Objects*. PhD thesis, Ecole Polytechnique Fédérale de Lausanne, 2003.
- [65] S. Iijima, C. Brabec, A. Maiti, and J. Bernholc. Structural flexibility of carbon nanotubes. *Journal of Chemical Physics*, 104:2089, 1996.
- [66] E. W. Wong, P. E. Sheehan, and C. M. Lieber. Nanobeam mechanics: Elasticity, strength and toughness of nanorods and nanotubes. *Science*, 277:1971, 1997.
- [67] M. B. Nardelli, B. I. Yakobson, and J. Bernholc. Mechanism of strain release in carbon nanotubes. *Physical Review B*, 57:R4277, 1998.
- [68] M. B. Nardelli, B. I. Yakobson, and J. Bernholc. Brittle and ductile behavior in carbon nanotubes. *Physical Review Letters*, 81:4656, 1998.
- [69] J. W. Seo, E. Couteau, P. Umek, K. Hernadi, P. Marcoux, B. Lukic, Cs. Mikó, M. Milas, R. Gaál, and L. Forró. Synthesis and manipulation of carbon nanotubes. *New Journal of Physics*, 5:120, 2003.
- [70] J. L. Bahr, I. T. Mickelson, M. J. Bronikowski, R. E. Smalley, and J. M. Tour. Dissolution of small diameter single-wall carbon nanotubes in organic solvents. *Chemical Communications*, 2:193, 2001.
- [71] A. B. Dalton, C. Stephan, J. N. Coleman, B. MaCarthy, P. M. Ajayan, S. Lefrant, P. Bernier, W. J. Blau, and H. J. Byrne. Selective interaction of a semiconjugated organic polymer with single-wall nanotubes. *Journal of Physical Chemistry B*, 104:10012, 2000.
- [72] V. Georgakilas, K. Kordatos, M. Prato, D. M. Guldi, M. Holzinger, and A. Hirsch. Organic functionalization of carbon nanotubes. *Journal of American Chemical Society*, 124:760, 2002.

- [73] T. W. Ebbesen and P. M. Ajayan. Large scale synthesis of carbon nanotubes. *Nature*, 358:220, 1992.
- [74] S. Fan, M. G. Chapline, N. R. Franklin, T. W. Tombler, A. M. Cassel, and H. Dai. Self-oriented regular arrays of carbon nanotubes and their field emission properties. *Science*, 283:512, 1999.
- [75] R. L. Vander Wal, T. M. Tichich, and V. E. Curtis. Diffusion flame synthesis of single-walled carbon nanotubes. *Chemical Physics Letters*, 323:217, 2000.
- [76] D. Laplaze, P. Bernier, W. K. Maser, G. Flamant, T. Guillard, and A. Loiseau. Carbon nanotubes the solar approach. *Carbon*, 36:685, 1998.
- [77] W. Kratschmer, L. D. Lamb, K. Fostiropoulos, and D. R. Huffman. Solid c-60 - a new form of carbon. *Nature*, 347:354, 1990.
- [78] D. S. Bethune, C. H. Kiang, M. S. Devries, G. Gorman, R. Savoy, J. Vazquez, and R. Beyers. Cobalt-catalyzed growth of carbon nanotubes with single-atomic-layer walls. *Nature*, 363:605, 1993.
- [79] M. Daenen, R.D. de Fouw, B. Hamers, P.G.A. Janssen, K. Schouteden, M.A.J. Veld, X.E.E. Reynhout, J.C. Reijenga, P.H.L. Notten, and R.A.H. Niessen. *The Wondrous World of Carbon Nanotubes*. Eindhoven University of Technology, 2003.
- [80] C. D. Scott, S. Arepalliand P. Nikolaev, and R. E. Smalley. Growth mechanisms for single-wall carbon nanotubes in laser-ablation process. *Applied Physics A: Materials Science and Processing*, 72:573, 2001.
- [81] V. Ivanov, J. B. Nagy, Ph. Lambin A. Lucas, X. B. Zhang, X. M. Zhang, D. Bernaerts, G. Van Tendeloo, S. Amelinckx, and J. Van Landuyt. The study of carbon nanotubules produced by catalytic method. *Chemical Physics Letters*, 223:329, 1994.
- [82] V. Ivanov, A. Fonseca, J. B. Nagy, A. Lucas, Ph. Lambin D. Bernaerts, and X. B. Zhang. Catalytic production and purification of nanotubes having fullerene-scale diameters. *Carbon*, 33:1727, 1995.
- [83] N. Nagaraju, A. Fonseca, Z. Konya, and J. B. Nagy. Alumina and silica supported metal catalyst for the production of carbon nanotubes. *Journal of Molecular Catalysis: A*, 181:57, 2002.

- [84] P. Ciambelli, D. Sannino, M. Sarno, A. Fonseca, and J. B. Nagy. Selective formation of carbon nanotubes over co-modified beta zeolite by ccvd. *Carbon*, 43:631, 2005.
- [85] A. Fonseca, K. Hernadi, J. B. Nagy, D. Bernaerts, and A. A. Lucas. Optimization of catalytic production and purification of buckyutubes. *Journal of Molecular Catalysis: A*, 107:159, 1996.
- [86] Christian Klinke. *Analysis of The Catalytic Growth of Carbon Nanotubes*. PhD thesis, Ecole Polytechnique Fédérale de Lausanne, 2003.
- [87] W. Z. Li, J. G. Wen, and Z. F. Ren. Straight carbon nanotube y junctions. *Carbon*, 79:1879, 2001.
- [88] M. S. Kabir, R. E. Morjan, O. A. Nerushev, P. Lundgren, S. Bengtsson, P. Enokson, and E. E. B. Campbell. Plasma-enhanced chemical vapour deposition growth of carbon nanotubes on different metal underlayers. *Nanotechnology*, 16:458, 2005.
- [89] S. Hofmann, B. Kleinsorge, C. Ducati, and J. Robertson. Controlled low-temperature growth of carbon nanofibres by plasma deposition. *New Journal of Physics*, 5:153, 2003.
- [90] M. J. Height, J. B. Howard, J. W. Tester, and J. B. Vander Sande. Flame synthesis of single-walled carbon nanotubes. *Carbon*, 42:2295, 2004.
- [91] S. Helveg, C. López-Cartes, J. Sehested, P. L. Hansen, B. S. Clausen, J. R. Rostrup-Nielsen, F. Abild-Pedersen, and J. K. Nørskov. Atomic-scale imaging of carbon nanofibre growth. *Nature*, 427:426, 2004.
- [92] H. Kanzov, A. Schmalz, and A. Ding. Laser-assisted production of multi-walled carbon nanotubes from acetylene. *Chemical Physics Letters*, 295:525, 1998.
- [93] F. Ding, K. Bolton, and A. Rosen. Nucleation and growth of single-walled carbon nanotubes: A molecular dynamics study. *Journal of Physical Chemistry B*, 108:17369, 2004.
- [94] F. Ding, A. Rosen, and K. Bolton. Molecular dynamics study of the catalyst particle size dependence on carbon nanotube growth. *Journal of Chemical Physics*, 121:2775, 2004.



- [95] D. Ciuparu, Y. Chen, S. Lim, G. L. Haller, and L. Pfefferle. Uniform-diameter single-walled carbon nanotubes catalytically grown in cobalt-incorporated mcm-41. *Journal of Physical Chemistry B*, 108:503, 2004.
- [96] D. B. Williams and C. B. Carter. *Transmission Electron Microscopy*. Plenum Press, New York and London, 1996.
- [97] E. Couteau, K. Hernadi, J. W. Seo, L. Thien-Nga, Cs. Mikó, R. Gaal, and L. Forró. Cvd synthesis of high-purity multiwalled carbon nanotubes using  $\text{CaCO}_3$  catalyst support for large-scale production. *Chemical Physics Letters*, 378:9, 2003.
- [98] T. de los Arcos, M. G. Garnier, J. W. Seo, P. Oelhafen, D. Mathys, and V. Thonmen. The influence of catalyst chemical state and morphology on the carbon nanotubes growth. *Journal of Physical Chemistry B*, 108:7728, 2004.
- [99] K. Hata, D. N. Futaba, K. Mizuno, T. Namai, M. Yumura, and S. Iijima. Water-assisted highly efficient synthesis of impurity-free single-walled carbon nanotubes. *Science*, 306:1362, 2004.
- [100] S. Maruyama, R. Kojima, Y. Miyauchi, S. Chiashi, and M. Kohno. Low-temperature synthesis of high-purity single-walled carbon nanotubes from alcohol. *Chemical Physics Letters*, 360:229, 2002.
- [101] C. H. Kiang and W. A. Goddard. Polyynes ring nucleus growth model for singlelayer carbon nanotubes. *Physical Review Letters*, 75:1086, 1996.
- [102] E. Flahaut, A. Govindaraj, A. Peigney, Ch. Laurant, A. Rousset, and CNR. Rao. Synthesis of single-walled carbon nanotubes using binary (fe, co, ni) alloy nanoparticles prepared in situ by the reduction of oxide solid solutions. *Chemical Physics Letters*, 300:236, 1999.
- [103] G. D. Rieck and J. J. M. Thijssen. The cation distribution in  $\text{CoFe}_2\text{O}_4$ . *Acta Cryst*, B24:982, 1968.
- [104] J. M. Bonard, M. Croci, F. Conus, T. Stockli, and A. Chatelain. Watching carbon nanotubes grow. *Applied Physics Letters*, 81:2836, 2002.
- [105] D. B. Geohegan, A.A. Puretzky, N. N. Ivanov, S. Jesse, G. Fres, and J. Y. Howe. In situ growth rate measurements and length control during chemical vapor deposition of vertically aligned multiwall carbon nanotubes. *Applied Physics Letters*, 83:1851, 2003.
- [106] I. Barin. *Thermochemical data of pure substances*. VCH, 1989.

- [107] M. J. Bronikowski, P. A. Willis, D. T. Colbert, K. A. Smith, and R. E. Smalley. Gas-phase production of single-walled nanotubes from carbon monoxide via the hipco process: A parametric study. *Journal of Vacuum Science and Technology A*, 19:1800, 2001.
- [108] B. Vigolo, A. Penicaud, C. Coulon, C. Sauder, R. Pailier, C. Journet, P. Bernier, and P. Poulin. Macroscopic fibers and ribbons of oriented carbon nanotubes. *Science*, 290(5495):1331–1334, 2000.
- [109] Y-L. Li, I. A. Kinloch, and A. H. Windle. Direct spinning of carbon nanotube fibers from chemical vapor deposition synthesis. *Science*, 304:276, 2004.
- [110] M. Zhang, K. R. Atkinson, and R. H. Baughman. Multifunctional carbon nanotube yarns by downsizing an ancient technology. *Science*, 306:1358, 2004.
- [111] Y. Li, K. Wang, J. Wei, Z. Gu, Z. Wnag, J. Luo, and D. Wu. Tensile properties of long aligned double-walled carbon nanotube strands. *Carbon*, 43:31, 2005.
- [112] A. Krishnan, E. Dujardin, T. W. Ebbesen, P. N. Yianilos, and M. M. J. Treacy. Young’s modulus of single-walled nanotubes. *Physical Review B*, 58:14013, 1998.
- [113] J.-P. Salvetat, J. M. Bonard, N. H. Thomson, A. J. Kulik, L. Forró, W. Benoit, and L. Zuppiroli. Mechanical properties of carbon nanotubes. *Applied Physics A*, 69:255, 1999.
- [114] J. M. Gere and S. P. Timoshenko. *Mechanics of Materials*. PWS-Kent, Boston, 1984.
- [115] A. Bachtold, J.-P. Salvetat, J. M. Bonard, M. Henny, C. Terrier, C. Strunk, L. Forró, and C. Schönberger. Contacting carbon nanotubes selectively with low-ohmic contacts for four-probe electric measurements. *Applied Physics Letters*, 73:274, 1998.
- [116] C. Schönberger and L. Forró. Multiwall carbon nanotubes. *Physics World*, June:37, 2000.
- [117] H. W. Zhu, C. L. Xu, D. H. Wu, B. Q. Wei, R. Vajtai, and P. M. Ajayan. Direct synthesis of long single-walled carbon nanotube strands. *Science*, 296:884, 2002.
- [118] H. H. Gommans, J. W. Alledredge, H. Tashiro, J. Park, J. Magnuson, and G. A. Rinzler. Fibers of aaligned single-walled carbon nanotubes: Polarized raman spectroscopy. *Journal of Applied Physics*, 88:2509, 2000.

- [119] J. Chen, A.M. Hamon, H. Hu, Y. Chen, A.M. Rao, P.C. Eklund, and R.C. Haddon. Solution properties of single-walled carbon nanotubes. *Science*, 282:95, 1998.
- [120] P. Launois and Ph. Poulin. *Macroscopically Aligned Carbon Nanotubes*. Encyclopedia of Nanoscience and Nanotechnology, 2003.
- [121] L. M. Ericson, H. Fan, H. Peng, V. A. Davis, W. Zhou, J. Sulpizio, Y. Wang, R. Booker, J. Vavro, Cs. Guthy, A. N. G. Parra-Vasquez, M. J. Kim, S. Ramesh, R. K. Saini, C. Kittrell, G. Lavin, H. Schmidt, W. W. Adams, W. E. Bilups, M. Pasquali, W. F. Hwang, J. E. Fisher, and R. E. Smalley. Macroscopic, neat, single-walled carbon nanotube fibers. *Science*, 305:1447, 2004.
- [122] R. J. Andrews, D. Jacques, D. Rao, A. M. Rantell, T. Derbyshire, F. Chen, Y. J. Chen, and R. C. Haddon. Nanotube composite carbon fibers. *Applied Physics letters*, 75:1329, 1999.
- [123] R. Haggemueller, H. H. Gommans, A. G. Rinzler, J. E. Fischer, and K. I. Winey. Aligned single-wall carbon nanotubes in composites by melt processing methods. *Chemical Physics letters*, 330:219, 2000.
- [124] F. W. J. Van Hattum, C. A. Bernardo, J. C. Finegan, G. G. Tibbetts, R. L. Alig, and M. L. Lake. A study of the thermomechanical properties of carbon fiber-polypropylene composites. *Polymer Composites*, 20:683, 1999.
- [125] G. G Tibbetts and J. J. McHugh. Mechanical properties of vapor-grown carbon fiber composites with thermoplastic matrices. *Jopurnal of Material Research*, 14:2871, 1999.
- [126] K. Lozano, J. Bonilla-Rios, and E. V. Barrera. A study on nanofiber-reinforced thermoplastic composites (ii): Investigation of the mixing rheology and conduction properties. *Journal of Applied Polymer Science*, 80:1162, 2001.
- [127] H. M. Ma, J. J. Zeng, M. L. Realff, S. Kumar, and D. A. Schiraldi. Processing, structure, and properties of fibers from polyester/carbon nanofiber composites. *Composite Science and Technology*, 63:1617, 2003.
- [128] A. R. Bhattacharyya, T. V. Sreekumar and T. Liu and S. Kumar, L. M. Ericson, R. H. Hauge, and R. E. Smalley. Crystallization and orientation studies in polypropylene/single wall carbon nanotube composite. *Polymer*, 44:2373, 2003.

- [129] V. A. Davis and M. Pasuali. *Macroscopic Fibers of Single Walled Carbon Nanotubes*. CRC press LLC, 2004.
- [130] P. Poulin, B. Vigolo, and P. Launois. Films and fibers of oriented single wall nanotubes. *Carbon*, 40:1741, 2002.
- [131] K. Jiang, Q. Li, and S. Fan. Spinning continuous carbon nanotube yarns. *Nature*, 419:801, 2002.
- [132] B. T. Kelly. *The Physics of Graphite*. Applied Science, London, 1981.
- [133] R. H. Telling, C. P. Ewels, A. A. El-Barbary, and M. I. Heggie. Wigner defects bridge the graphite gap. *Nature Materials*, 5:333, 2003.
- [134] P. M. Ajayan, C. Colliex, P. Bernier, and J. M. Lambert. Shape transformations in single-layer carbon nanotubes. *Microscopy Microanalysis Microstructures*, 4:501, 1993.
- [135] C. H. Kiang, W. A. Goddard, R. Beyers, and D. S. Bethune. Structural modification of single-layer carbon nanotubes with an electron beam. *Journal of Physical Chemistry*, 100:3749, 1996.
- [136] V. H. Crespi, N. G. Chopra, M. L. Cohen, A. Zettl, and S. G. Louie. Anisotropic electron-beam damage and the collapse of carbon nanotubes. *Physical Review B*, 54:5927, 1996.
- [137] B. Smith and D. E. Luzzi. Electron irradiation effects in single wall carbon nanotubes. *Journal of Applied Physics*, 90:3509, 2001.
- [138] P. M. Ajayan, V. Ravikumar, and J.-C. Charlier. Surface reconstructions and dimensional changes in single-walled carbon nanotubes. *Physical Review Letters*, 81:1437, 1998.
- [139] Y. Zhang and S. Iijima. Microstructural evolution of single-walled carbon nanotubes under electron irradiation. *Philosophical Magazine Letters*, 80:427, 2000.
- [140] M. Terrones, H. Terrones, F. Banhart, J.-C. Charlier, and P. M. Ajayan. Coalescence of single-walled carbon nanotubes. *Science*, 288:1226, 2000.
- [141] M. Terrones, F. Banhart, N. Grobert, J.-C. Charlier, H. Terrones, and P. M. Ajayan. Molecular junctions by joining single-walled carbon nanotubes. *Physical Review Letters*, 89:075505, 2002.

- [142] V. H. Crespi, N. G. Chopra, M. L. Cohen, A. Zettl, and V. Radmilovic. Site-selective radiation damage of collapsed carbon nanotubes. *Applied Physics Letters*, 73:1435, 1998.
- [143] M. Sennett, E. Welsh, J. B. Wright, W. Z. Li, J. G. Wen, and Z. F. Ren. Dispersion and alignment of carbon nanotubes in polycarbonate. *Applied Physics A*, 76:111, 2003.
- [144] B. Stisen. Measurement of the complex modulus of elasticity of fibres and folios. *Bruel and Kjaer Technical Review*, 2:3, 1970.
- [145] L. Meirovitch. *Elements of Vibration Analysis*. McGraw-Hill, New York, ed.2, 1986.
- [146] Cs. Mikó, M. Milas, J. W. Seo, E. Couteau, N. Barišić, R. Gaál, and L. Forró. Effect of electron irradiation on the electrical properties of fibers of aligned single-walled carbon nanotubes. *Applied Physics Letters*, 83:4622, 2003.
- [147] A. W. P. Fung, Z. H. Wang, M. S. Dresselhaus, G. Dresselhaus, R. W. Pekala, and M. Endo. Coulomb-gap magnetotransport in granular and porous carbon structures. *Physical Review B*, 49:17325, 1994.
- [148] A. L. Efros and B. I. Shklovskii. Coulomb gap and low temperature conductivity of disordered systems. *Journal of Physics C*, 8:L49, 1975.
- [149] S.C. Clark, C.E. Hoyle, S. Jonsson, F. Morel, and C. Dekker. Photopolymerization of acrylates using n-aliphaticmaleimides as photoinitiators. *Polymer*, 40:5063, 1999.
- [150] M. Grujicic, G. Cao, A. M. Rao, T. M. Tritt, and S. Nayak. Uv-light enhanced oxidation of carbon nanotubes. *Applied Surface Science*, 214:289, 2003.
- [151] T. Savage, S. Bhattacharya, B. Sadanadan, J. Gaillard, T. M. Tritt, Y. Sun, Y. Wu, S. Nayak, R. Car, N. Mazari, P. M. Ajayan, and A. M. Rao. Photoinduced oxidation of carbon nanotubes. *Journal of Physics: Condensed Matter*, 15:5915, 2003.
- [152] B. S. Makki, M. R. Ghafouri-Fard, S. Mohajerzadeh, T. Maleki, S. Mohammadi, M. Miri, and A. E. Soleimani. A novel ultra-violet assisted anisotropic etching of plastic to realize micro-gears. *Sensors and Actuators A*, 115:563, 2004.

- [153] B. S. Makki, M. Moradi, A. Moafi, S. Mohajerzadeh, B. Hekmatshoar, and D. Shahrjerdi. A novel ultra-violet assisted anisotropic etching of plastic to realize micro-gears. *IEEE Sensors Journal*, 4:743, 2004.
- [154] S. Anoopkumar-Dukie. *Rhodes University Electronic Theses Collection*. PhD thesis, Rhodes University, 2000.
- [155] K. B. Shelimov, R. O. Esenaliev, A. G. Rinzler, Ch. B. Huffman, and R. E. Smalley. Purification of single-wall carbon nanotubes by ultrasonically assisted filtration. *Chemical Physics Letters*, 282:429, 1998.
- [156] J. Liu, A. G. Rinzler, H. Dai, J. H. Hafner, R. K. Bradley, P. J. Boul, A. Lu, T. Iverson, K. Shelimov, C. B. Huffman, F. Rodriguez-Macias, Y.-S. Shon, T. R. Lee, D. T. Colbert, and R. E. Smalley. Fullerene pipes. *Science*, 280:1253, 1998.
- [157] L. Thien-Nga, K. Hernadi, E. Ljubovic, S. Garaj, and L. Forró. Mechanical purification of single-walled carbon nanotube bundles from catalytic particles. *Nano Letters*, 2:1349, 2002.
- [158] J. M. Bonard, T. Stora, J. P. Salvetat, F. Maier, T. Stockli, C. Duschl, L. Forró, W. A. de Herr, and A. Châtelain. Purification and size-selection of carbon anotubes. *Advanced Materials*, 9:827, 1997.
- [159] A. Bhattacharya and S. D. Mahanti. Critical micelle concentration in three-dimensional lattice models of amphiphiles. *Journal of Physics: Condensed Matter*, 13:L861, 2001.
- [160] J. Tabony, A. de Geyer, and L. F. Braganza. Assembly of micelles into higher-order structures with salt concentration. *Nature*, 327:321, 1987.
- [161] C. Richard, F. Balavoine, P. Schultz, T. W. Ebbesen, and Ch. Mioskowski. Supramolecular self-assembly of lipid derivatives on carbon nanotubes. *Science*, 300:775, 2003.
- [162] L. Capes, E. Valentin, S. Esnouf, A. Ribayrol, O. Jost, A. Filoramo, and J.-N. Patillon. High yield nondestructive purification of single wall carbon nanotubes monitored by epr measurements. *IEEE Conference Proceedings*, August 28:439, 2002.

# Curriculum Vitae

## Personal Data

Birthday 04. 05. 1978.  
Nationality Hungarian  
Marital Status married, 1 child

## Education

**2003–2005** PhD student at EPFL, Faculty of basic sciences, Institute of physics of complex matter under the supervision of and in the group of prof. Forró László

**2002** Diploma thesis on the subject of synthesis and characterisation of carbon nanotubes

**1996–2002** Eötvös Lóránd University, Budapest, Hungary.  
Certified Teacher of Physics (Msc)

**1996** Baccalaureate, Pollák Antal specialized secondary school, Szentes, Hungary. (Informatics and Electronics)

## Languages

English, French, Hungarian.

## Experimental methods

Transmission and scanning electron microscopies  
Electrical resistivity measurements, Labview programming  
Atomic force microscopy

## Teaching experience

**2003-2004** Teaching assistant, Physics Lab (Travaux pratiques de physique), EPFL, (Dr. Schaller)

## Achievements

**1999** Special prize for the paper on Observation of Domain Structure of Soft Magnetic Materials on “as-quenched” Ribbons, in the framework of a Student Research Program





## Publications

*Growth of Carbon Nanotubes with Alkaline Earth Carbonate as Support*

A. Magrez, J. W. Seo, Cs. Mikó, K. Hernádi and L. Forró

Journal of Physical Chemistry B, **109**, 10087 (2005).

*Effect of Band Structure on Quantum Interference in Multiwall Carbon Nanotubes*

B. Stojetz, Cs. Mikó, L. Forró and Ch. Strunk

Physical Review Letters, **94**, 186802 (2005).

*Determination of the Intershell Conductance in Multiwalled Carbon Nanotubes*

B. Bourlon, Cs. Mikó, L. Forró, D. C. Glatti and A. Bachtold

Physical Review Letters, **93**, 176806 (2004).

*Carbon Nanotube Based Bearing for Rotational Motions*

B. Bourlon, D. C. Glatti, Cs. Mikó, L. Forró and A. Bachtold

Nano Letters, **4**, 709 (2004).

*Geometrical Dependence of High-Bias Current in Multiwalled Carbon Nanotubes*

B. Bourlon, D. C. Glatti, Cs. Mikó, L. Forró and A. Bachtold

Physical Review Letters, **92**, 26804 (2004).

*Effect of electron irradiation on the electrical properties of fibers of aligned single-walled carbon nanotubes*

Cs. Mikó, M. Milas, J. W. Seo, E. Couteau, N. Barišić, R. Gaál and L. Forró

Applied Physics Letters, **83**, 4622 (2003).

*Synthesis and manipulation of carbon nanotubes*

J. W. Seo, E. Couteau, P. Umek, K. Hernadi, P. Marcoux, B. Lukic, Cs. Mikó, M.

Milas, R. Gaál and L. Forró

New Journal of Physics, **5**, 120 (2003).

*CVD synthesis of high-purity multiwalled carbon nanotubes using CaCO<sub>3</sub> catalyst support for large-scale production*

E. Couteau, K. Hernadi, J. W. Seo, L. Thien-Nga, Cs. Miko, R. Gaal and L. Forró

Chemical Physics Letters, **378**, 9 (2003).

*Controlled Growth and Applications of Carbon Nanotubes*

K. Hernadi, E. Couteau, P. Umek, Cs. Mikó, J. W. Seo, L. Forró, M. Croci, C. Klinke, P. Chauvin and J. M. Bonard  
Chimia, **56**, 547 (2002).

Submitted and in preparation

*Effect of ultraviolet light irradiation on the electrical and mechanical properties of single-walled carbon nanotube fibers*

Cs. Mikó, M. Milas, J. W. Seo, R. Gaál, A. Kulik and L. Forró

Submitted to Applied Physics Letter

*Quantum-Limited Thermal Transport in Multi-Walled Carbon Nanotubes*

H.-Y. Chiu, V. V. Deshpande, H. H. W. Ch. Postma, C. N. Lau, Cs. Mikó, L. Forró and M. Bockrath

Submitted to Science